Physics of Gallium Nitride Quantum Wells

A thesis submitted to The University of Manchester for the degree of Master of Philosophy in the Faculty of Science and Engineering

2018

Lydia M W Jim

School of Physics and Astronomy

Contents

Word Count: 26,313

List of Figures

List of Tables

Abstract

In this thesis, studies performed on InGaN/GaN quantum well (QW) structures using photoluminescence (PL) spectroscopy are presented. Green light-emitting InGaN/GaN QW structures with a varying number of QWs (1, 3, 5 & 10) were investigated with respect to the effect of QW number on internal quantum efficiency (IQE). 10 K transient PL measurements performed on the samples showed that the QW samples have different lifetimes. This suggests that there is a varying level of indium content amongst the samples, different average QW layer thickness between the samples and/or strain relaxation in the 10 QW sample. Comparing the 3 and 5 QW samples, which have similar lifetimes, the 300 K excitation power dependent IQE measurements performed on the samples shows that IQE increases with QW number; this can be attributed due to the increased recapture of escaped thermally excited carriers.

Additionally, InGaN/GaN QWs with varying growth temperatures were studied with respect to their high energy band (HEB) and efficiency droop behaviour; the samples grown at higher growth temperatures have a lower defect density and this could affect the HEB and efficiency droop. The HEB is a recently reported feature on the high energy side of the typical emission peak in the PL spectra of InGaN/GaN QWs. 10 K excitation power dependent PL showed that the sample with the highest growth temperature exhibited efficiency droop at a higher excitation compared to the other samples; this may be because efficiency droop is influenced by defect-related recombination. 10 K time-resolved PL showed that the samples have similar HEB behaviour despite their different growth temperatures; monoexponential decay components and inflections which corresponded to the HEB were observed in the time decay measurements. 10 K excitation power varying time decay measurements performed across the PL spectra on one of the samples showed that the lifetime of the carriers at a given emission energy is constant at low carrier densities and decreases at high carrier densities; this reduction in lifetime occurred at a higher carrier density at higher PL emission energies.

Declaration

No portion of the work referred to in the thesis has been submitted in support of an application for another degree or qualification of this or any other university or other institute of learning.

Copyright Statement

Acknowledgements

I would like to offer my special thanks to my supervisor Dr. David Binks, my co-supervisor Dr. Peter Mitchell and Prof. Phillip Dawson for their patient guidance, useful critique and generous support.

Furthermore, I am particularly grateful to Dr. George Christian and Stephen Church for their illuminating discussions, benevolent assistance and warm friendship during my time at the University of Manchester.

Additionally, I also wish to acknowledge Dr. Simon Hammersley, Dr. Marina Leontiadou and Dr. Darren Graham for their kind assistance in the laboratory.

I would also like to extend my thanks to colleagues at the University of Cambridge for providing me with samples to study.

Lastly, I would like to express my gratitude to my friends and family who have supported me, with special thanks to Timmy and Bethany Jim for proof-reading this thesis.

"There are darknesses in life and there are lights, and you are one of the lights, the light of all lights."

- Bram Stoker, Dracula

Chapter 1

Introduction

Group III-Nitrides are semiconductors which can be alloyed to emit light that covers the whole visible spectrum. III-Nitrides semiconductors are commonly used for lighting in the form of light emitting diodes (LEDs) and laser diodes (LDs); they are also attractive candidates for power electronic applications. Many group III-Nitrides LEDs and LDs employ indium gallium nitride multiple quantum well (MQW) active regions. Indium gallium nitride acts as an efficient light emitter despite possessing a high number density of defects ($\sim 10^8 - 10^9$ cm^{-2}) which would lead to device failure in III-Arsenides and III-Phosphides light emitting devices; this has been attributed to the presence of potential fluctuations in the QWs which spatially localize the charge carriers and inhibit their access to non-radiative recombination centres.

In 2014, Nakamura, Amano and Akasaki jointly received the Nobel Prize in Physics for their work in developing efficient blue LEDs based on gallium nitride which led to the production of bright, energy-efficient white light sources. The adoption of LED lighting will aid climate change mitigation since it is more energy efficient than traditional incandescent lightbulbs and compact fluorescent lamps. The majority of global electricity is generated from fossil fuels and around one fifth of it is used for lighting[1, 2]; generating electricity from fossil fuels releases carbon dioxide into the atmosphere which accelerates climate change through the greenhouse effect. In the 2015 report 'The LED Lighting Revolution', Signify (formerly Philips Lighting) estimated that 403 million tons

of carbon dioxide emissions could be prevented and $94 billion US dollars saved if there was a global switch to using LED lighting across the private sector[3]. Improving the efficiency of LEDs could further reduce carbon dioxide emission and the financial cost of lighting.

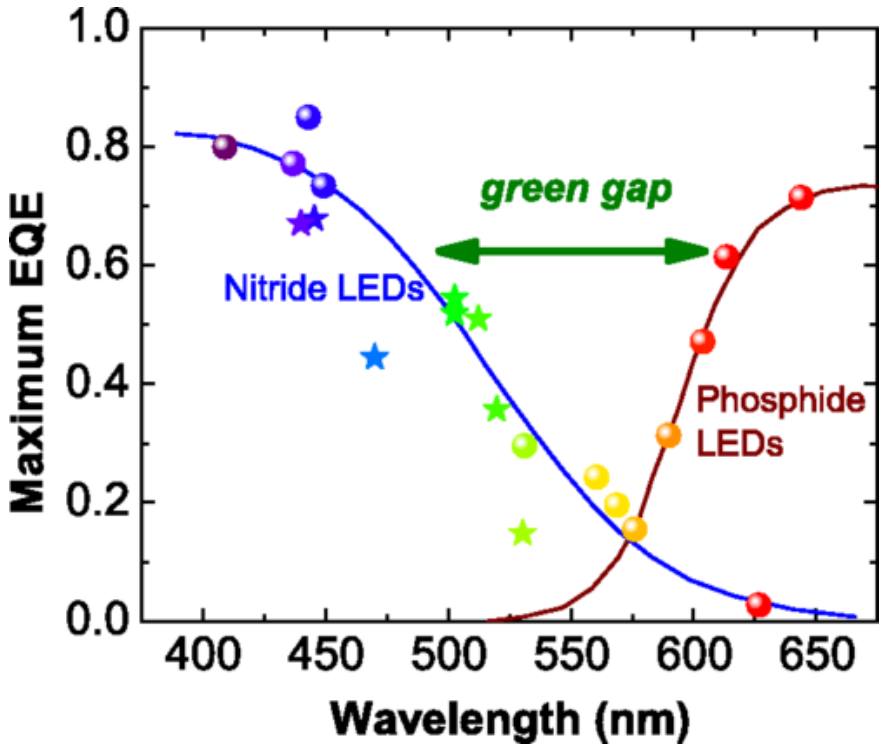

Figure 1.1: The maximum external quantum efficiency (EQE) of nitride and phosphide LEDs, highlighting the green gap. Taken from Reference [4] with permission.

One of the issues currently limiting the adoption of InGaN MQW light emitters is the so-called "green gap". Green light-emitting InGaN QWs are less efficient than their blue light-emitting counterparts, see Figure 1.1. This is one of the barriers to producing white light emitters by combining red, green and blue LEDs. Currently, it is common practice to instead create the appearance of a white light emitting LED by using a phosphor coating on a blue InGaN LED that absorbs some of the blue light and re-emits the energy as yellow light; energy is lost in this process as the photons are re-emitted at a longer wavelength. The wavelength at which the InGaN QWs emit is tuned by varying the percentage of indium incorporated into the ternary alloy. Green light-emitting In-

GaN QWs require a larger percentage of indium than blue light-emitting InGaN QWs; the presence of more indium may lead to more defect formation during growth and this could be a cause of the lower internal quantum efficiency (IQE) of green InGaN QWs compared to blue InGaN QWs[5]. Alternatively, the lower growth temperature required to grow green InGaN QWs to reduce the desorption of indium during growth may cause more defect formation and lead to reduced efficiency[5].

The efficiency of InGaN MQW light emitters is also constrained at high carrier densities by efficiency "droop". At high carrier densities, the light-emitting efficiency of InGaN QWs decreases with increasing carrier density. One of the several proposed mechanisms is carrier density activated defect recombination where localized states become saturated at high carrier densities so that carriers are able to access structural defects which act as non-radiative recombination centres[7]. An additional emission band on the high energy side of the normal emission spectra, a "high energy band" (HEB), has been recently observed at high carrier densities in InGaN QWs; this suggests that droop could occur when deeply localized ground states become saturated and carriers are able to occupy more weakly localized excited states from which the carriers can recombine radiatively, albeit with reduced efficiency[9].

This work attempts to investigate the factors limiting the efficiency of InGaN QWs. Two series of green InGaN QW samples have been investigated using photoluminescence spectroscopy and time-correlated single photon counting techniques; one series with a varying number of QWs and the other with varying growth temperature, which has previously been shown to correspond to defect density[10, 11]. This thesis contains a review of the background information on InGaN QWs in Chapter 2, details of the experimental techniques used to investigate the InGaN QWs in Chapter 3, the results of the investigations in Chapters 4 and 5 and a conclusion of the work in Chapter 6. Descriptions of the history of gallium nitride, an ideal quantum well and III-Nitrides are also included in the next sections of this chapter.

1.1 History and Development

This section aims to provide a brief overview of the development and history of gallium nitride. The fabrication of GaN was first reported by Johnson *et al.* in 1932 who heated pure gallium with ammonia to create powdered GaN[12]. In 1969, Maruska and Tietjen developed a method to grow crystalline GaN on sapphire using hydride vapour phase epitaxy (HVPE) which uses a reactor with varying temperature zones[13]. In the source zone, hydrogen chloride gas reacts with liquid gallium to form gaseous gallium chloride compounds which flow in to the deposition zone and react with ammonia gas to form solid GaN films. Maruska and Tetjen reported that HVPE grown GaN had a high residual carrier density of above 10^{19} cm^{-3} without intentional doping and when p-type doping with germanium was attempted, the material became electrically inhomogeneous. Metal-Insulator-Semiconductor type LEDs, which do not require p-type doping, were fabricated by Maruska *et al.*[14] and Ilegems and Dingle[15] in 1973 using HVPE.

The growth of GaN was advanced by Yoshida *et al.* and Amano *et al.* who grew GaN films on an AlN buffer using molecular beam epitaxy (MBE) in 1983 and metal-organic chemical vapour deposition (MOCVD) in 1986 respectively. Yoshida *et al.* reported that GaN grown with an AlN buffer layer have higher Hall mobilities than GaN grown directly on sapphire and attributed it to the smaller difference in the thermal expansion coefficient and lattice parameter between GaN and AlN than between GaN and sapphire[16]. Amano *et al.* reported that GaN films grown on an AlN buffer layer by MOCVD have a better surface morphology and less cracks compared to GaN films grown on sapphire[17]. In 1991, Nakamura grew higher quality GaN films on a GaN buffer layer with Hall mobilities of 600 cm^2/Vs at room temperature using MOCVD[18]. MBE and MOCVD are described later in Section 1.3.1.

In 1989, Amano *et al.* made progress in the p-type doping of GaN using low-energy electron-beam irradiation (LEEBI) post-growth treatment of Mg-doped GaN and created the first GaN p-n junction blue LED[19]. In 1992, Nakamura *et al.* also achieved p-type doped GaN by post-

growth thermal annealing of Mg-doped GaN in nitrogen[20]. Later in 1992, the problems associated with p-type doping of GaN was attributed to the formation of Mg-H complexes during growth due to the disassociated hydrogen from ammonia passivating magnesium[21, 22]; post growth LEEBI treatment and thermal annealing in nitrogen removed the atomic hydrogen from Mg-H complexes and reactivated the acceptors. This was later theoretically confirmed by Neugenbauer and Van de Walle in 1995[23, 24]. Okamoto *et al.* also published first principle calculations of the Mg-H complex in 1996 [25].

The production and commercialization of GaN based p-n junction LEDs followed the resolution of the issue of p-type doping. The next advance was due to the ability to grow satisfactory III-nitrides alloys. In 1991, Itoh *et al.* fabricated AlGaN/GaN layered structures[26] and Yoshimoto *et al.* grew the first InGaN sample to exhibit photoluminescence using MOCVD[27]. Previously grown InGaN required a low growth temperature to control indium incorporation as the equilibrium vapour pressure of nitrogen over InN is very high compared to AlN and GaN. Yoshimoto *et al.* grew InGaN under a high temperature and a high source indium flow rate and reported that InGaN grown at 800 °C exhibited better crystal quality than InGaN grown at 500 °C.

In 1993, Nakamura *et al.* made the first blue p-n junction LED with an GaN/InGaN double heterostructure[28]. The InGaN active layer had a lower band gap energy than the GaN barriers and confined carriers, leading to higher internal quantum efficiency compared to the preceding homostructure GaN LEDs. The development of yellow and green InGaN based LEDs soon followed[29, 30]. The production of GaN based QW LEDs was followed by the fabrication and commercialisation of GaN based laser diodes (LDs). The first GaN based LD was made by Nakamura *et al.* in 1996 and had an InGaN multiple QW structure[31]; this followed from the observations of optically pumped stimulated emission from an InGaN epilayer by Khan *et al.* in 1994[32] and the production of an InGaN/AlGaN double heterostructure by Amano *et al.* in 1993[33].

In addition to GaN based LDs and LEDs, work was also carried out on GaN based transistors. The first GaN based metal semiconductor field effect transistor was made by Khan *et al.* in 1992[35]; the structure

consisted of n-type doped GaN epilayer grown on sapphire with an AlN buffer with silver and gold contacts and gate. GaN based transistors are commercialized but are still an immature technology. GaN based transistors exhibit advantages over traditional silicon based transistors in terms of a higher breakdown voltage and more efficient high temperature operation[36].

1.2 Ideal Quantum Wells

When an electron (or a hole) is confined in a potential well which has a length comparable to the de Broglie wavelength of the electron (or hole), its properties are modified compared to those found in the bulk. Confined carriers within semiconductor QWs have higher radiative recombination rates compared to carriers in bulk semiconductors as the electrons and holes are closer together and their wave functions have more of an overlap. Confinement also modifies the energy levels and density of states; these are further modified by the effects of localization in a complex way, which is difficult to model. Nevertheless, analysing an ideal QW provides some useful basic insights. This section examines the energy levels of a simplified ideal quantum well and the density of states expected in ideal quantum wells.

Infinite Potential Well

The confinement energy E of an electron (or a hole) of effective mass m^* confined in a one dimensional quantum well along the z axis can be found by solving the time independent Schrödinger's equation which is given by:

$$E\psi(z) = -\frac{\hbar^2}{2m^*}\frac{d^2\psi(z)}{dz^2} + V(z)\psi(z), \tag{1.1}$$

where $\psi(z)$ is the wavefunction of the electron $|\psi(z)|^2$ gives the probability of finding the electron or hole at a position z, $\hbar$ is the reduced Planck constant and $V(z)$ is the potential of the well[34]. For a simplified QW

with infinite potential barriers of width d, the solution is given by:

$$\psi(z) = \sqrt{\frac{2}{d}} \sin(\frac{n\pi z}{d}), \tag{1.2}$$

which gives a confinement energy E of:

$$E = \frac{n^2 h^2}{8m^* d^2}. \tag{1.3}$$

The confined electron can only have certain discrete energies within the well since n is a non-zero, positive integer; a real quantum well with a finite potential barrier also has discrete electron energy levels but does not have an infinite number of energy levels. The wavefunction of the electron can also spread into the walls of the well in a finite potential well.

1.2.1 Two Dimensional Free Electron Gas

For an electron confined in a well of length d along the z axis, the electrons are free to move (and have kinetic energy) in the x and y direction within the well. A real semiconductor quantum well confines both holes and electrons within the plane of the well. The Schrödinger's equation for a two dimensional free electron gas is given by:

$$E\psi(x, y, z) = -\frac{\hbar^2}{2m^*} \nabla^2 \psi(x, y, z) + V(x, y, z)\psi(x, y, z), \tag{1.4}$$

where $V(x, y, z) = \infty$ everywhere except for $0 \leq z \leq d$, where $V(x, y, z) = 0$. Using periodic boundary conditions in the xy plane of $\psi(x, y, z) = \psi(x + L_x, y, z)$ and $\psi(x, y, z) = \psi(x, y + L_y, z)$ where L_x and L_y are the width and length of the film, the solution takes the form of:

$$\psi(x, y, z) = Be^{ik_x x} e^{ik_y y} \sin(\frac{n\pi z}{d}), \tag{1.5}$$

where B is a constant, $k_x = \frac{2\pi p}{L}$, $k_y = \frac{2\pi q}{L}$, $k = \frac{n\pi}{d}$ and p, q and n are integers (wave-functions in the form of $e^{ik_x x}$ represents travelling waves).

The total energy, including kinetic energy terms, is given by:

$$E = \frac{n^2 h^2}{8m^* L^2} + \frac{h^2(k_x^2 + k_y^2)}{8m^* \pi^2}, \tag{1.6}$$

where k_x and k_y describes the motion of the electrons within the film. This gives a parabolic dispersion relation, see Figure 1.2.

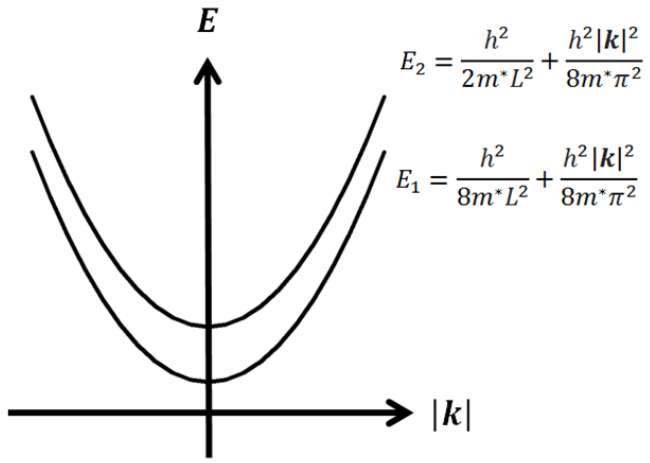

Figure 1.2: Schematic of the dispersion relation of electrons inside an ideal quantum well. Only the first two subbands are shown.

1.2.2 Density of States

The possible k_x and k_y states associated with each nth state can be represented as a two dimensional plot in $\boldsymbol{k}$-space where $k = |\boldsymbol{k}| = \sqrt{k_x^2 + k_y^2}$, see Figure 1.3. The density of electron states per unit area for each nth state is given by:

$$g(k)dk = \frac{\text{No. of spin states per } \boldsymbol{k} \text{ state}}{\text{Area}} \cdot \frac{\text{Area between k and k + dk in } \boldsymbol{k}\text{-space}}{\text{Area per } \boldsymbol{k} \text{ state}}$$

$$g(k)\ dk = \frac{2}{L_x L_y} \frac{2\pi k\ dk}{4\pi^2 / L_x L_y} = \frac{k\ dk}{\pi}. \tag{1.7}$$

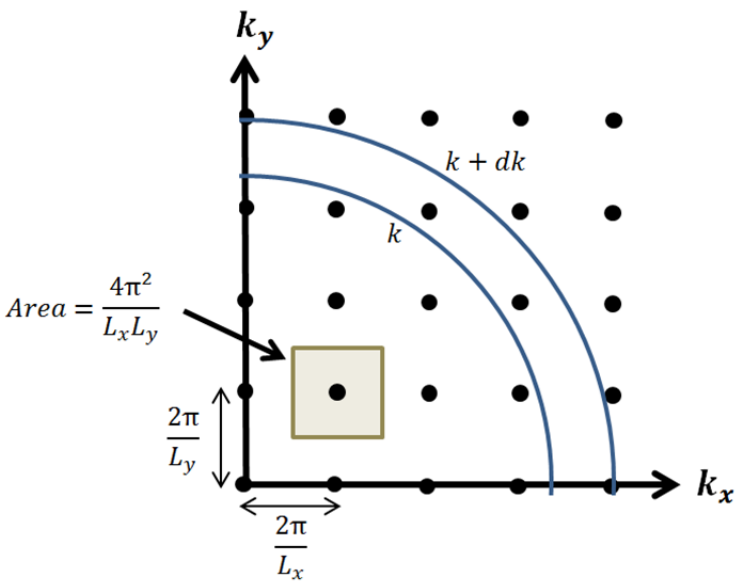

Figure 1.3: Representation of possible k_x and k_y states in $\boldsymbol{k}$-space; each point represents an allowed momentum value of an electron.

The density of states per unit area for each nth state can be written in terms of energy E as:

$$g(E)\ dE = \frac{m^*}{\pi\hbar}\ dE. \tag{1.8}$$

The density of states is independent of energy and the total density of states of all n states, see Figure 1.4, resembles a step-like function.

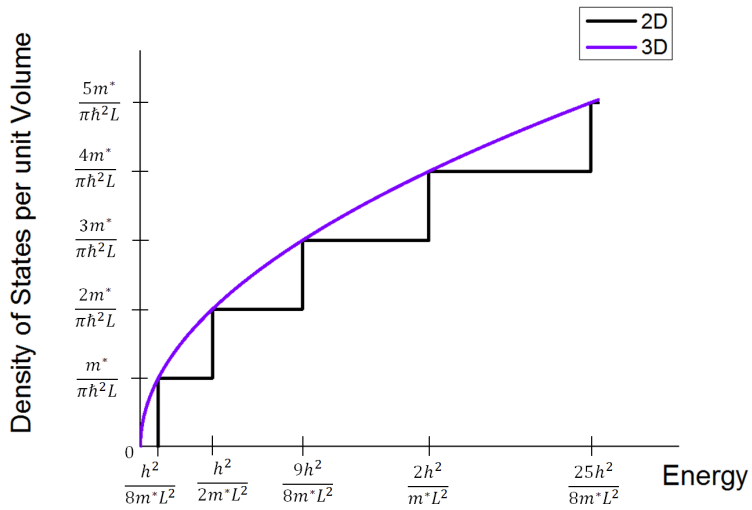

Figure 1.4: Schematic of the total density of states per unit volume of electrons inside an ideal quantum well and in bulk material.

1.3 III-Nitrides

This section briefly describes the crystal structure of III-Nitrides, the effects of alloying III-Nitrides on the lattice constant and bandgap, the growth of wurtzite III-Nitrides and the polarisation of wurtzite III-Nitrides.

AlN, GaN and InN can have two crystal structures: wurtzite and zinc-blende. Wurtzite GaN is hexagonal with a ABAB stacking sequence of (0001) planes in the $< 0001 >$ direction and zinc-blende GaN is cubic with an ABCABC stacking sequence of (111) planes in the $< 111 >$ direction, see Figure 1.5. Zinc-blende GaN, AlN and InN are metastable; GaN, AlN and InN have lower cation-nitrogen pair bonding energies in the wurtzite polytype than in the zinc-blende polytype. This section will focus on wurtzite AlN, GaN and InN.

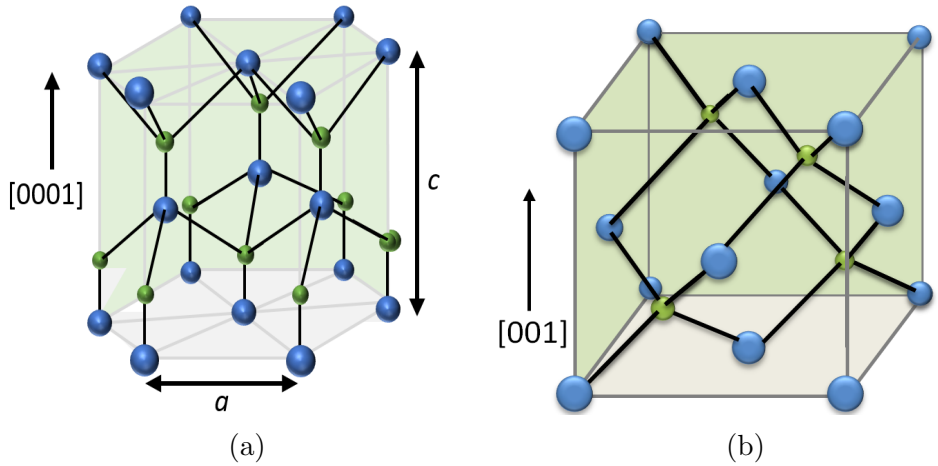

Figure 1.5: Ball and stick model of the (a) wurtzite structure of hexagonal GaN and (b) zinc-blende structure of cubic GaN. The blue spheres represent gallium and the green spheres represent nitrogen. The lattice parameters a and c are indicated for the wurtzite structure of hexagonal GaN.

The lattice constant a, indicated in Figure 1.5a, of a ternary III-nitride alloy $A_xB_{1-x}N$ varies linearly between the lattice constants of the two binary III-nitride alloys AN and BN with molar fractional com-

position x according to Vegard's law which is given by:

$$a(x) = xa_{AN} + (1-x)a_{BN}, \tag{1.9}$$

where a_{AN} and a_{BN} are the lattice constants of the binary alloys AN and BN respectively. The band gap $E_g(x)$ of a ternary III-nitride alloy $A_xB_{1-x}N$ is not linear with molar fractional composition x and given by:

$$E_g(x) = xE_g^{AN} + (1-x)E_g^{BN} - bx(1-x), \tag{1.10}$$

where E_g^{AN} and E_g^{BN} are the band gap energies of the binary alloys AN and BN respectively and the bowing parameter b describes the parabolic dependence of the average band gap on molar fractional composition x, see Figure 1.6.

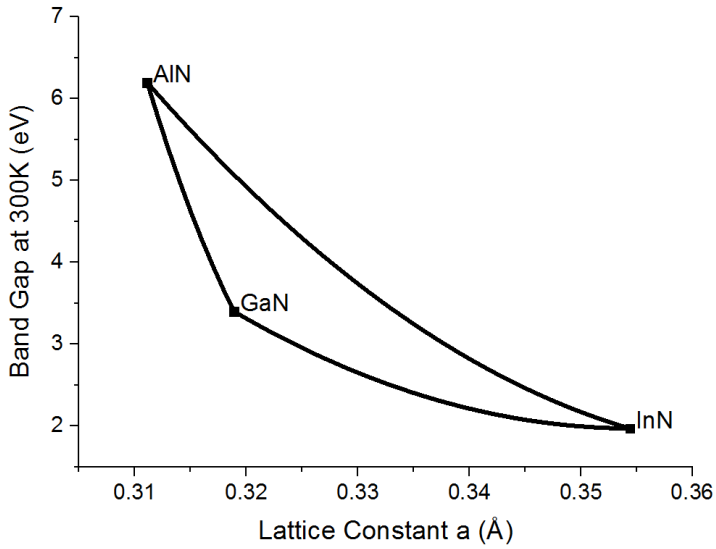

Figure 1.6: The band gap at 300 K for AlN, GaN and InN as function of their lattice constant a is plotted using Equation 1.9, Equation 1.10 and the recommended values of the bowing parameter for III-nitride alloys by Vurgaftman and Meyer[38]. The values used for the band gap energies for AlN, GaN and InN are obtained from Yim *et al.*[39], Perry and Rutz[40], Monemar[41] and Guo and Yoshida[42].

1.3.1 Growth

Substrates

Wurtzite GaN is produced by epitaxial (layer-by-layer) growth on a sapphire (Al_2O_3) substrate. Alternative substrates for GaN include silicon (Si), silicon carbide (SiC), gallium arsenide (GaAs), lithium gallate ($LiGaO_2$), aluminium nitride and GaN[37]. In general, the quality of the sample grown depends on the amount of mismatch between the lattice parameter and co-efficient of thermal expansion between GaN and the substrate. The higher the lattice mismatch between the substrate and GaN, the higher the in-plane strain experienced and the more likely defects are to occur. For lattice mismatched growth of a material on a different substrate material (heteroepitaxial growth), dislocations and misfits occur to relieve strain after the material has been grown to a critical thickness. For substrates that have a different thermal expansion coefficient, cracking and bowing can occur when cooling. For the growth of a material on the same substrate material (homoepitaxial growth), there is no mismatch in lattice parameter or thermal expansion coefficient so the dislocation densities are much lower and cracking and bowing do not occur.

In this project, the green light-emitting wurtzite InGaN/GaN QWs studied were produced by epitaxial growth on sapphire (Al_2O_3) substrates in the c-plane so this section will focus on c-plane sapphire. GaN can be grown on the c-, a-, r- and m-planes of sapphire [43]. In the growth of GaN on $c-$plane sapphire, the sapphire substrate and GaN $c-$planes are rotated by 30° with respect to each other, see Figure 1.7, to reduce the lattice mismatch from 30 % to about 14 %. GaN grown on $c-$plane sapphire has dislocation densities on the order of 10^{10} cm^{-2}; in comparison, gallium arsenide produced by homoepitaxal growth has much lower dislocation densities on the order of 10^2 cm^{-2} to 10^4 cm^{-2}[44]. Sapphire has a greater coefficient of thermal expansion than GaN; this causes compressive stress to be applied to the GaN layer in the plane of the growth surface when the sample is cooled after deposition. In the case of thick films, the stress can lead to the fracture of the film and the substrate[45].

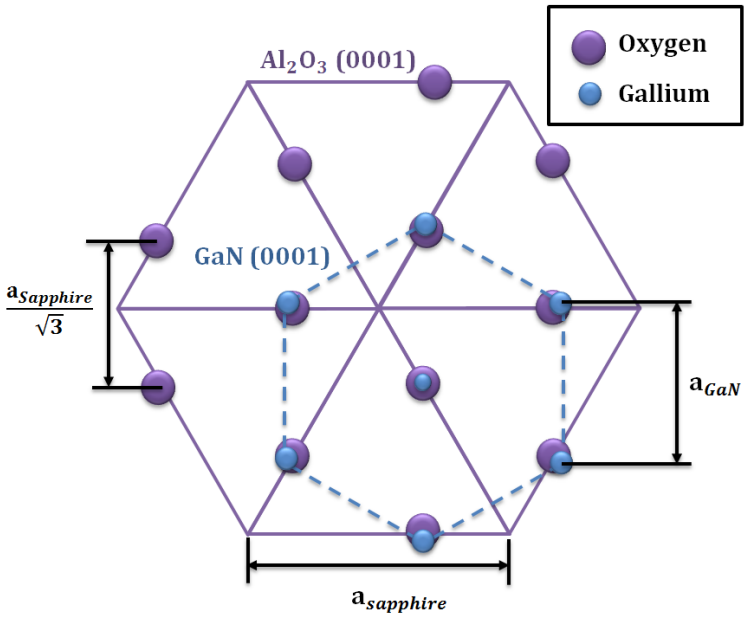

Figure 1.7: Schematic diagram demonstrating the alignment of the GaN *c*-plane on the *c*-plane of the sapphire substrate to reduce lattice mismatch.

Growth Techniques

III-Nitrides are typically grown by Molecular Beam Epitaxy (MBE) or Metal Organic Chemical Vapor Deposition (MOCVD). Both MBE and MOCVD are epitaxial growth processes.

In MBE growth of III-nitrides, the substrate is mounted on a rotating, heated platform in an ultra high vacuum ($< 10^{-9}$ Torr) chamber with liquid nitrogen cooled panels[44]. Reflection high-energy electron diffraction is used to monitor the sample growth *in situ*, in real time[46]. Ultra-pure aluminium, indium and gallium are evaporated and deposited on the sample surface using Knudsen (effusion) cells which can be shuttered; the aperture of the Knudsen cell is very small compared to the mean free path of the evaporated particles such that the vapour is emitted in a cosine distribution. Nitrogen is supplied as ammonia gas or nitrogen plasma from radio-frequency resonance at 113.56 MHz or electron cyclotron resonance at 2.45 GHz. The particle beams are collimated and targeted at the substrate and do not interact until they reach the heated substrate. GaN is typically grown at around 800 K; the growth

of GaN via MBE is a non-equilibrium reaction where the growth rate of GaN is reduced at high temperature as GaN is thermodynamically unstable in vacuum. MBE with ammonia gas has growth rates limited by the disassociation of NH_3 which requires a high temperature to be efficient. In plasma-assisted MBE, the delivery of active nitrogen is independent of temperature.

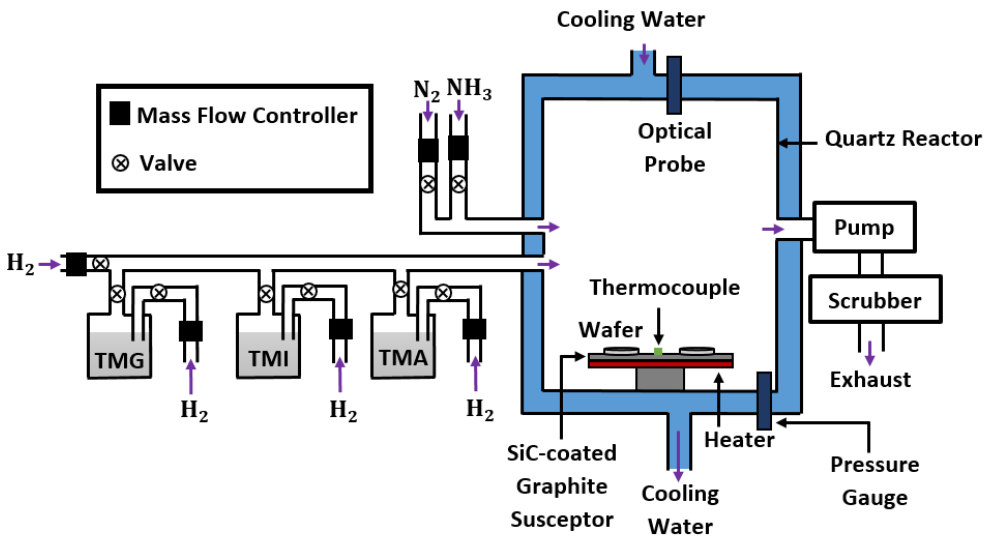

Figure 1.8: Schematic diagram of a Metal Organic Vapour Epitaxy setup for the growth of III-Nitrides. Hydrogen gas is bubbled through trimethylgallium (TMG), trimethylindium (TMI) and trimethylaluminium (TMA).

In MOCVD, hydrogen gas is bubbled through metal organic liquid precursors as a carrier gas. The metal organic chemical vapour is transported over a heated substrate, where they react and form a nitride film, see Figure 1.8. The samples used in this project were grown using a Thomas Swan MOCVD closed couple showerhead system. The precursors used for the samples were trimethylgallium, trimethylindium and trimethylaluminium; ammonia was used as the nitrogen source. The growth temperature of GaN is typically much higher (>900 °C) in MOCVD than in MBE. High nitrogen-to-gallium ratios are also typically used in MOCVD to minimise nitrogen loss from GaN films.

MOCVD is typically used in industry over MBE for growing III-

Nitrides as more than one wafer can be grown in the reaction chamber per growth run in MOCVD. MOCVD also has faster growth rates. However, MBE gives better thickness control compared to MOCVD[47].

1.3.2 Polarisation

Wurtzite III-nitrides have both intrinsic spontaneous and strain-induced piezoelectric polarisation. The intrinsic spontaneous polarisation is due to the presence of a unique direction that is polar in GaN and is present in unstrained wurtzite GaN, InN and AlN crystals. The strain induced polarisation is caused by lattice mismatch during growth.

Spontaneous Polarisation

In wurtzite GaN, gallium and nitrogen form interpenetrating hexagonal close packed structures which stack along the c-axis. Gallium and nitrogen atoms form polar bonds as nitrogen is more electronegative than gallium so electrons are attracted to the nitrogen nuclei. These gallium-nitrogen dipoles do not overlap along the c-axis direction, resulting in a net polarisation parallel to the c-axis. The spontaneous polarisation $P_{SP}^{A_xB_{1-x}N}$ of a III-nitride ternary alloy $A_xB_{1-x}N$ can be determined by:

$$P_{SP}^{A_xB_{1-x}N} = xP_{SP}^{AN} + (1-x)P_{SP}^{BN} - x(1-x)b_{SP}^{ABN}, \tag{1.11}$$

where x is the molar fractional composition of AN, P_{SP}^{AN} is the spontaneous polarisation of AN, P_{SP}^{BN} is the spontaneous polarisation of BN and b_{SP}^{ABN} is the bowing parameter of the ternary alloy[54]. The spontaneous polarisation of GaN, AlN and InN were determined to be -0.034 Cm^{-2}, -0.090 Cm^{-2} and -0.042 Cm^{-2} respectively and spontaneous polarisation bowing parameters of AlGaN, InGaN and AlInN were determined to be 0.019 Cm^{-2}, 0.038 Cm^{-2} and 0.071 Cm^{-2} by Fiorentini *et al.* through *ab initio* calculations[49]. Prodhomme, Beya-Wakata and Bester also obtained similar values of -0.027 Cm^{-2}, -0.095 Cm^{-2} and -0.035 Cm^{-2} for the spontaneous polarisation of GaN, AlN and InN respectively through calculations[50]. Lahnemann *et al.* experimentally determined the spontaneous polarisation of GaN to be -0.022 ± 0.007 Cm^{-2}[51].

Piezoelectric Polarisation

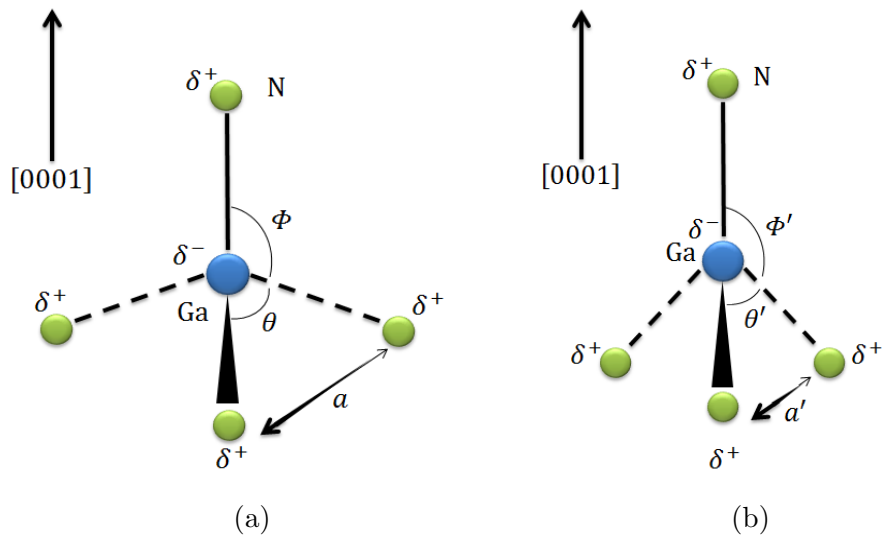

Figure 1.9: Diagram showing the bond angles between gallium and nitrogen in (a) relaxed GaN and (b) GaN compressed in the c-plane.

Thin wurtzite InGaN alloy layers grown pseudomorphically on wurtzite GaN in the [0001] direction experience an in-plane compressive strain due to their different lattice parameters a perpendicular to the growth direction. In relaxed GaN, see Figure 1.9, the polarisation of the Ga-N bonds P_{GaN} caused by the difference in electronegativity between gallium and nitrogen atoms are balanced out by the tetrahedral arrangement of the nitrogen atoms around the gallium atom, such that all the angles θ, ϕ between each Ga-N bond are equal and are given by:

$$3P_{GaN}\cos(180^\circ - \phi) = P_{GaN}, \tag{1.12}$$

where $\phi = 109.5^\circ$ in GaN in the ideal crystal approximation. In a GaN lattice under compressive strain, see Figure 1.9., the lattice parameter a is reduced to a', the bonds are compressed such that $\theta' < \phi'$ and the polarisation of the Ga-N bonds are no longer balanced out, resulting in a piezoelectric polarisation in the growth direction.

The strain-induced polarisation $\boldsymbol{P^{pz}}$ of an InGaN QW layer between two GaN barriers can be determined from the scalar product of the piezo-

electrical modulus tensor $\boldsymbol{d}$ and the stress tensor $\boldsymbol{\sigma}$ by:

$$P_i^{pz} = \sum_{j=1}^{6} d_{ij}\sigma_j, \tag{1.13}$$

where P_3^{pz} is the only non-zero strain-induced polarisation component in the growth direction. For biaxial stress, the piezoelectrical modulus tensor $\boldsymbol{d}$ can expressed as:

$$\boldsymbol{d} = \begin{bmatrix} 0 & 0 & 0 & 0 & \frac{1}{2}d_{15} & 0 \\ 0 & 0 & 0 & \frac{1}{2}d_{15} & 0 & 0 \\ d_{31} & d_{31} & d_{33} & 0 & 0 & 0 \end{bmatrix}. \tag{1.14}$$

Under the assumption of no shear stress or shear strain, the stress tensor $\boldsymbol{\sigma}$ can be determined from the scalar product of the elastic stiffness constant tensor $\boldsymbol{C}$ for a hexagonal geometry under biaxial stress and the strain tensor $\boldsymbol{\epsilon}$ by:

$$\sigma_k = \sum_{l=1}^{6} C_{kl}\epsilon_l. \tag{1.15}$$

Using Hooke's law modified for hexagonal geometries, Equation 1.15 can be expressed as:

$$\begin{bmatrix} \sigma_1 \\ \sigma_2 \\ \sigma_3 \\ 0 \\ 0 \\ 0 \end{bmatrix} = \begin{bmatrix} C_{11} & C_{12} & C_{13} & 0 & 0 & 0 \\ C_{12} & C_{11} & C_{13} & 0 & 0 & 0 \\ C_{13} & C_{13} & C_{33} & 0 & 0 & 0 \\ 0 & 0 & 0 & C_{44} & 0 & 0 \\ 0 & 0 & 0 & 0 & C_{44} & 0 \\ 0 & 0 & 0 & 0 & 0 & \frac{1}{2}(C_{11} - C_{12}) \end{bmatrix} \begin{bmatrix} \epsilon_1 \\ \epsilon_2 \\ \epsilon_3 \\ \epsilon_4 \\ \epsilon_5 \\ \epsilon_6 \end{bmatrix}. \tag{1.16}$$

By assuming that the in-plane strain is isotropic such that $\epsilon_1 = \epsilon_2 = \frac{a_b - a_{QW}}{a_{QW}}$ and that there is no stress applied along the c-axis, such that $\sigma_3 = 0$, it is implied that ϵ_3 can be expressed in terms of ϵ_1 as:

$$\epsilon_3 = -\frac{2C_{13}}{C_{33}}\epsilon_1. \tag{1.17}$$

Hence the strain-induced polarisation component P_3^{pz} in the growth di-

rection is given by:

$$\begin{aligned} P_3^{pz} &= d_{31}\sigma_1 + d_{31}\sigma_2 + d_{33}\sigma_3 \\ &= 2d_{31}\sigma_1 \\ &= 2d_{31}(C_{11}\epsilon_1 + C_{12}\epsilon_2 + C_{13}\epsilon_3) \\ &= \epsilon_1(C_{11} + C_{12} - \frac{2C_{13}^2}{C_{33}}). \end{aligned} \tag{1.18}$$

Alternatively, the strain-induced polarisation component P_3^{pz} in the growth direction can be written in terms of the piezoelectric coefficient tensor; the piezoelectric coefficient $\boldsymbol{e}$ is defined in terms of the piezoelectrical modulus tensor $\boldsymbol{d}$ and the elastic stiffness constant tensor $\boldsymbol{C}$ as:

$$e_{mn} = \sum_{p=1}^{6} d_{mp}C_{pn}. \tag{1.19}$$

Hence the the strain-induced polarisation $\boldsymbol{P^{pz}}$ can be expressed as:

$$P_i^{pz} = \sum_{j=1}^{6} d_{ij}\sigma_j = \sum_{j=1}^{6}\sum_{l=1}^{6} d_{ij}C_{jl}\epsilon_l = \sum_{l=1}^{6} e_{il}\epsilon_l. \tag{1.20}$$

And the strain-induced polarisation component P_3^{pz} in the growth direction can be expressed as[52][53]:

$$\begin{aligned} P_3^{pz} &= e_{31}\epsilon_1 + e_{32}\epsilon_2 + e_{33}\epsilon_3 \\ &= 2e_{31}\epsilon_1 - \frac{2C_{13}}{C_{33}}e_{33}\epsilon_1 \\ &= 2\left(\frac{a_b - a_{QW}}{a_{QW}}\right)\left(e_{31} - \frac{C_{13}}{C_{33}}e_{33}\right). \end{aligned} \tag{1.21}$$

Table.1.1 shows some of the reported values of the piezoelectric coefficients $e_{31,33}$ and the elastic stiffness constants $C_{13,33}$ for AlN, GaN and InN.

Table 1.1: Reported values of the piezoelectric coefficients $e_{31,33}$ and the elastic stiffness constants $C_{13,33}$. (a), (b) and (c) are values from references [54], [55] and [38] respectively.

Parameters	e_{31} (Cm^{-2})	e_{33} (Cm^{-2})	C_{13} (GPa)	C_{33} (GPa)
AlN	-0.53 (a) -0.58 (b)	1.50 (a) 1.55 (b)	108 (c)	373 (c)
GaN	-0.34 (a)	0.67 (a)	106 (c)	398 (c)
InN	-0.41 (a)	0.81 (a)	92 (c)	224 (c)

Quantum Confined Stark Effect

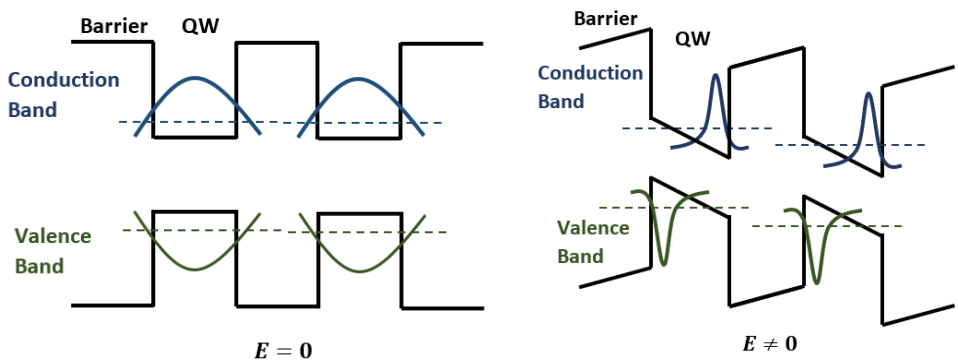

(a) No electric field. (b) Non-zero electric field.

Figure 1.10: Diagram demonstrating the effect of an electric field across a quantum well on the hole wavefunction in the valence band and electron wavefunction in the conduction band.

The quantum confined Stark effect (QCSE) observed in InGaN/GaN QWs grown in the [0001] direction is a consequence of the spontaneous and strain-induced polarisation present in the GaN barriers and the InGaN QWs[59, 57]. The InGaN alloy and the GaN barriers have different polarisation along the [0001] direction. The abrupt change in polarisation at the interfaces of the hetero-structure induces a fixed charge at the interface, which in accordance with Gauss law, induces an electric field across the QW and the barriers. The piezoelectric field is calculated to increase with the indium content of the InGaN QW[59]. For a series of InGaN QW of length L_{QW} with identical GaN barriers of length L_B, the

electric field F_{QW} across the QW is given by [58]:

$$F_{QW} = \frac{(P_B^{Tot} - P_{QW}^{Tot})L_B}{\epsilon_0(\epsilon_B L_{QW} + \epsilon_{QW} L_B)}, \tag{1.22}$$

where P_B^{Tot} and P_{QW}^{Tot} are the total sum of the spontaneous and piezoelectric polarisation present in the barriers and the QWs respectively, ϵ_0 is the absolute dielectric constant and ϵ_B and ϵ_{QW} are the relative dielectric constants of the barriers and the QWs respectively. The electric field causes the potential energy of charge carriers to change linearly with distance along growth direction, resulting in a more triangular shaped well; this is shown schematically in Figure 1.10. The QCSE localizes the charge carriers at opposite sides of the QW, decreasing their confinement energies[59] and reducing their wavefunction overlap[60]. The reduction in wavefunction overlap between carriers in the QW increases the lifetime of the carriers and decreases the probability of radiative recombination, reducing the internal quantum efficiency of the InGaN QW[61]; this effect is more pronounced in InGaN wells of a higher indium content.

The built-in electric field can be screened by the injection of carriers to increase the space charge at the interface of the QW to balance out the piezoelectrically induced charges[62]. In the photoluminescence spectroscopy of InGaN QWs, where carriers are photo-excited, the screening of the QCSE is exhibited by a blueshift in the peak emission energy and a decrease in the width of the emission peak with increasing carrier injection[63, 64].

Chapter 2

Carrier Recombination in Photo-excited InGaN/GaN QWs

In photoluminescence spectroscopy of InGaN/GaN QWs, electrons and holes that are excited by an absorbed photon can recombine radiatively or non-radiatively. Carrier recombination dynamics in photo-excited InGaN/GaN QW samples are not directly equivalent to carrier recombination dynamics in InGaN/GaN QW LEDs where carriers are electrically excited. However, PL provides an insight to the underlying physics of InGaN QWs which could be applied to InGaN QW LEDs. This section discusses the recombination mechanisms observed in InGaN QWs.

2.1 Radiative Recombination

This section describes the features of InGaN/GaN QW PL spectra. Figure 2.1 shows the PL spectra of a 5 QW InGaN/GaN QW sample at 10 K. The main emission peak centered around 2.38 eV is a superposition of the emission from each QW; the lower energy side of the main emission peak is broader than the higher energy side. The emission from the InGaN/GaN QWs has been attributed to the radiative recombination of localized holes and electrons within the quantum well, see Section 2.1.1. Shoulder emission peaks at multiples of around 91 meV lower in energy

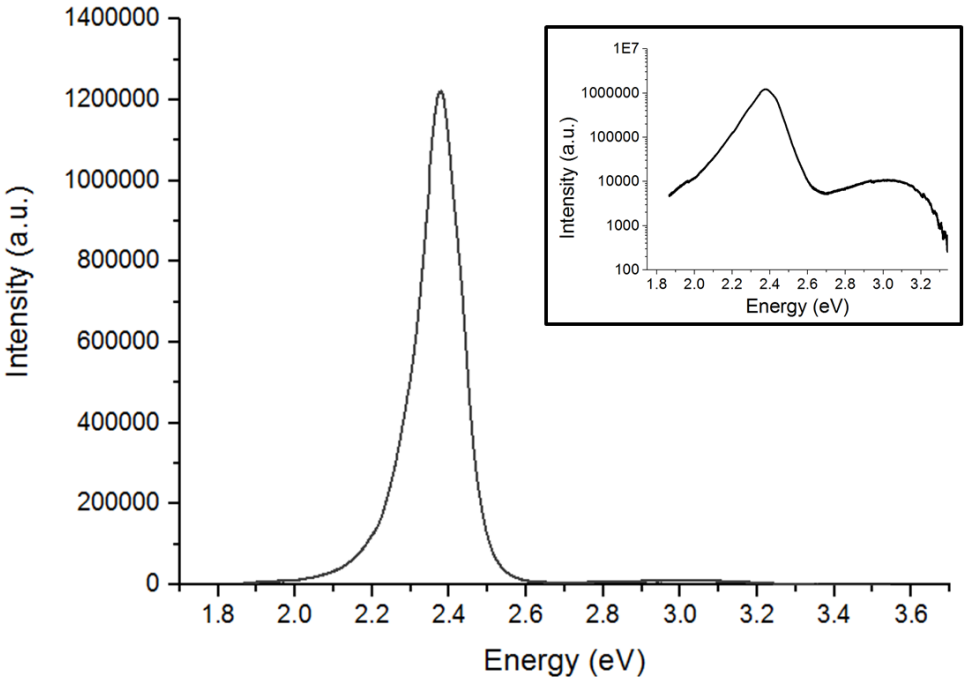

Figure 2.1: The photoluminescence spectra of a 5 QW InGaN/GaN sample at 10 K. The spectra is plotted with a logarithmic intensity scale in the inset. Carriers were excited to be above the GaN band gap.

relative to the main QW emission peak, called "phonon replicas", have often been observed[97, 89]. They are not resolved in Figure 2.1; these peaks have been attributed to phonon accompanied radiative recombination. In phonon accompanied radiative recombination, a spatially separated electron and hole pair in a QW act as a dipole which induces polarisation in the local charge distribution. When the spatially separated electrons and holes recombine, a lower optical phonon is created and dissipates the stored potential energy in the lattice. The Huang-Rhys factor relates the intensities of the phonon replicas to the zero-phonon (primary) peak. The Huang-Rhys factor depends strongly on the spatial separation between the electrons and holes[89].

Furthermore, a "high energy band" (HEB) that is present at an energy higher than the main QW emission peak has been recently reported by several authors[9, 99, 100, 101, 102, 104]. (It is not present in Figure 2.1.) The HEB is typically observed at very high carrier densities

and has been attributed to a number of origins: radiative recombination from weakly localized states following the saturation of deeply localized states[9, 99, 100], carriers recombining from non-ground state subbands with indices greater than $n = 1$ (see Equation 1.6)[101], confined electrons in the QW recombining with holes that are partially confined in the QW in a "confined hole continuum"[102] and the recombination of carriers in a high density of electron-hole plasma[104]. The HEB is more fully discussed in Chapter 5.

In addition to QW-related emission, luminescence from the GaN layers is also present in the PL spectra of InGaN/GaN QWs. Photoluminescence from the GaN barriers itself, which would be located at around 3.5 eV, cannot be observed in Figure 2.1. A blue luminescence band can be observed in Figure 2.1 and is more clearly shown in the logarithmic plot in the inset. The source of this blue luminescence band is uncertain; the blue luminescence band has been observed in undoped GaN samples where it has been attributed to Mg impurities. Kaufmann *et al.* suggested that GaN self-compensates against shallow Mg impurities by forming a deep donor level and that the blue luminescence band in undoped GaN is due to the donor-acceptor pair recombination of electrons from the deep donor level with holes in the shallow Mg acceptor level[105]. A yellow luminescence band, around 2.2 eV, observed in the PL of undoped GaN with carbon impurities and silicon doped GaN may be concealed by the QW emission in Figure 2.1; this band has been ascribed to gallium vacancy-related and carbon-related defects[106]. Other defect-related luminescence bands not discussed here have also been observed in GaN; a comprehensive review is provided by Reshchikov and Morkoç[107].

2.1.1 Carrier Localization

Localization of carriers has been widely agreed as the cause of efficient light emission in LEDs employing InGaN active layers despite the large defect densities ($\sim 10^9$ cm^{-2}) present in InGaN which would quench radiative recombination in III-Arsenides and III-Phosphides[65]. In localization, carriers are trapped by potential fluctuations below the band gap

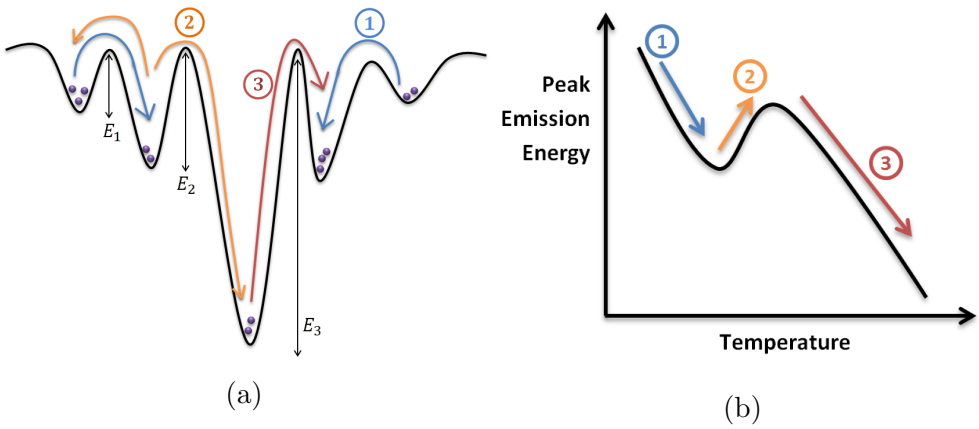

Figure 2.2: Diagram showing the redistribution of carriers responsible for the S-shape peak emission energy behaviour with increasing temperature. Potential fluctuations with different energies E_1, E_2 and E_3 are shown in (a). The purple spheres represent carriers. The corresponding change in peak emission energy with temperature is shown in (b) with labels for steps 1, 2 and 3.

at certain spatial positions within the plane of the InGaN active layer, keeping carriers away from defects acting as non-radiative recombination centres.

The presence of localization can be seen from the redshift-blueshift-redshift or "S-shape" of the emission peak as function of temperature in photoluminescence (PL) spectroscopy, see Figure 2.2. At very low temperatures, the charge carriers are randomly distributed among the localized states and do not have sufficient energy to escape from the states[66]. As the temperature is increased, the peak energy redshifts due to the more weakly bound carriers having sufficient energy to escape from their localized states and redistribute themselves in localized states of lower energies. With the further increase of temperature, the carriers thermalise and redistribute into higher energy localized states, causing a blueshift in the peak energy. The redshift occurring at higher temperature is due to the shrinkage of the band gap. It has been shown that the S-shape temperature dependence of the peak emission energy is reduced with increasing excitation power; this was attributed to the saturation of localized states with increasing carrier density[67].

The localization of carriers is further evidenced by PL time decay

curves observed in InGaN QWs at low temperature at low carrier densities. In time-resolved PL, a short laser pulse is used to excite the sample and the emission of the sample is measured as a function of time relative to a start signal triggered by the laser pulse, see Chapter 3. PL time decay curves reflect the population change of carriers at a given emission energy as a function of time. In low temperature time-resolved PL of InGaN QWs at low carrier densities, time decay curves that were not mono-exponential and had a similar shape when the carrier density was varied have been observed; this was attributed to carriers occupying and recombining from a range of potential traps, similar to behaviour observed in quantum dot samples [68, 69].

The localization of carriers is also demonstrated by the difference between the PL and absorption peak, the Stokes shift[70, 71]. The PL emission peak occurs at lower energy than the absorption edge. The absorption occurs at a higher energy where there is a higher density of states. However, the Stokes shift could also be due to, or be enhanced, by the screening of the electric field and the reduction of the QCSE by charge carriers during absorption experiments[72, 68]. The mechanism of carrier localization in InGaN has long been a subject of debate and has been thought to be caused by indium clustering, random alloy fluctuations and quantum well width fluctuations.

Indium Clustering

The first proposed mechanism for the localization of charge carriers was indium clustering, where electrons and holes are trapped in nano-scale indium rich, dot-like, regions with a reduced band gap. Dark nano-scale spots representing locally strained areas within InGaN QWs was observed though transmission electron microscopy (TEM) by Narukawa *et al.*; the spatial distribution of indium in and around the dark spots was evaluated using energy-dispersive x-ray microanalysis and it was found that the dark regions in the quantum wells always had a higher indium percentage than the surrounding quantum well regions[73]. The locally strained regions attributed to indium clustering in InGaN QWs were observed using high energy TEM imaging[74, 75]. Indium clustering was

initially proposed to be caused by spinodal decomposition[73], a phase separation mechanism that does not require an energy barrier to be overcome for nucleation to occur, based on a theoretical phase diagram for relaxed zinc-blende InGaN alloys[76]; the diagram suggested that for the indium content and growth temperature of blue and green light-emitting InGaN, phase separation of indium and gallium would occur. However, the diagram did not consider the effect of coherency strains due to the formation of an interface between gallium and indium[65]. Later, a phase diagram for biaxially strained wurtzite InGaN alloys accounting for the coherency strain between the gallium-indium interface was calculated[77]; it predicted that for the indium content and growth temperatures of green and blue light-emitting InGaN QWs, InGaN should be a random alloy. It was also suggested that the appearance of indium clustering was an artefact caused by high energy electron beam damage during TEM imaging of InGaN QW samples[78, 79, 80]; this was demonstrated using TEM imaging with a minimal exposure[81] and atomic probe tomography (APT)[82, 83] by comparing samples that have and have not undergone high energy TEM imaging.

Random Alloy Fluctuations

Bellaiche *et al.* first proposed that holes can be localized by indium atoms in atomically inhomogeneous zinc-blende InGaN with statistical random alloy fluctuations without nano-scale indium clustering[84]. Shortly after, Wang calculated that holes can be localized by In-N-In chains in random wurtzite InGaN alloys[85]. Though there were some discrepancies between the predictions made by Bellaiche *et al.* and Wang with experimental results relating to the InGaN bowing parameter and the behavior of the photoluminescence linewidth with indium content respectively, some experimental results supported the localization of holes by random alloy fluctuations[65]. Using positron annihilation, Chichibu *et al.* determined that positrons, which would be localized in the same sites as holes, had very short diffusion lengths (<4 nm) in wurtzite InGaN alloys, promoting the idea of localization of holes on an atomic scale[86]. Graham *et al.* compared the low temperature resonantly excited PL

spectra of InGaN/GaN QWs with an acoustic phonon replica to a modelled spectrum which accounted for the coupling to acoustic phonons; they determined the localization length scale of carriers to be around 2.5 Å for InGaN wells of 15 % and 25 % indium concentration[87]. However, a similar previous experiment yielded a larger carrier localization length of around 2 nm for InGaN QWs with similar widths and indium content[88].

Though the mechanism of localization appeared to be found for holes through random alloy fluctuations, there was some debate as to how are electrons are localized. Bellaiche *et al.* and Wang originally suggested that electrons were localized by forming bound excitons with localized holes[84, 85]. However, Kalliakos *et al.* carried out low temperature photoluminescence spectroscopy of GaN/InGaN QWs of varying thicknesses and found that the Huang-Rhys factor increased monotonically with QW width, which is inconsistent with a bound exciton model and more consistent with a Donor Acceptor Pair (DAP) model where electrons and holes are separately localized[89]. This leaves random alloy fluctuations unable to solely account for carrier localization.

Quantum Well Monolayer Width Fluctuations

An increase in the width of a QW lowers the confinement energy within the QW; it has been shown that monolayer well width fluctuations are sufficient to localize excitons in GaAs/AlGaAs QWs at low temperatures[90]. The localization effect is not observed at high temperatures in GaAs/AlGaAs QWs as the localization effect is small and when given sufficient thermal energy, the carriers can escape from the well width fluctuation. In InGaN/GaN QWs, the confinement energy of carriers within the QW is further enhanced by the QCSE due to piezoelectric polarisation; Graham *et al.* calculated that for an ground state electron and hole in a 3.3 nm InGaN QW with a 25 % indium content, an increase of the well width by one monolayer decreases the confinement energy by 58 meV, suggesting that monolayer well width fluctuations can localize carriers in InGaN QWs at room temperature[88]. It has been observed using APT[83] and TEM[88] that the lower interface of

InGaN QW layers are smooth and well width fluctuations of one to two monolayers thick are present on the top layer of InGaN QW layers, at the interface between the QW and the the capping GaN layer; the formation of the well width fluctuations were attributed to the growth mechanism of the InGaN QW layer[83].

There is some theoretical support for the localization of carriers by monolayer well width fluctuations in conjunction with random alloy fluctuations. A study determined the localization lengths of electrons to be between 7 nm to 10 nm and the localization lengths of holes to be around 1 nm for InGaN QWs with a 5 % to 25 % indium concentration; the model used the numerical solutions of the effective mass Schrödinger equation and included a 10 nm diameter disk shaped monolayer well width fluctuation and accounted for random alloy fluctuations and strain and built in field fluctuations[91]. A second, more recent modelling study on an InGaN QW with a 25 % indium content with 5 nm diameter disk shaped two monolayers thick well width fluctuations which accounted for random alloy fluctuations and strain-induced and spontaneous electric fields was also carried out[92]. Both sets of authors reported that the localization lengths of holes calculated was consistent with the experimentally determined results of 2 nm[88], though this result was reported for both electrons and holes. Both also suggested that the holes are well localized by random alloy fluctuations whereas electrons have larger localization lengths and are mainly localized by local well width fluctuations but there remains a lack of experimental evidence to confirm or deny localization by random alloy fluctuations.

Dislocation Screening

Though there is support for monolayer well width fluctuations and random alloy fluctuations as the cause of localization, the exact mechanism of how InGaN QWs keep carriers away from defects remain inconclusive and the screening of carriers from dislocations by means of a potential barrier around dislocations may also play a role in the high IQE observed in InGaN QWs despite the high defect density present. The formation of potential barriers around dislocations have been proposed to be caused

by the following: the formation of V-shaped pits at the termination of dislocations[93], dislocation terminations leading to reduced well thickness without V-shaped pits[94] and dislocations passing through the edge or between intermittent InGaN QW strips[95].

Hangleiter *et al.* put forward that threading dislocations in the GaN layer preceding the InGaN QW layer leads to the formation of V-shaped hexagonal pits in the InGaN QW layer during growth for InGaN QWs optimized for high IQE. The V-shaped pits were observed using atomic force microscopy (AFM) and were found to have side walls in the $(1\bar{1}01)$ plane; the QW layer is distorted in these pits and is thinner as the InGaN growth rate is reduced compared to the surrounding undistorted QW layer[93]. Hangleiter *et al.* used a combination of low temperature spectra taken from near the threading dislocations, TEM and spectroscopic scanning near-field microscopy to demonstrate that regions near the threading dislocations emitted some light at higher energies than the main emission peak of the InGaN QW, which is consistent with regions of reduced QW width. A reduced thickness of the QW layer around a threading dislocation increases the local band gap around the defect and could act as an energy barrier to carriers.

Grandjean *et al.* also suggested that the termination of dislocations leads to thinner regions in the QW layers during growth[94]. Grandjean *et al.* observed deep valleys in the InGaN QW layer using AFM and used time-resolved cathodoluminescence to demonstrate that light emission from inside a valley redshifts with time; this is a characteristic sign of diffusion of carriers from a high energy to a low energy region. The light emission from inside the valleys is at a higher energy compared to outside the valley and the emission peak of the cathodoluminescence of the valleys was wider than of surrounding regions, suggesting that the valleys have a greater band gap and a wider distribution of energy levels compared to the surrounding regions.

Additionally, Van der Laak *et al.* used AFM and TEM to observe that MOVCD grown InGaN QWs that have been grown at a single temperature and annealed in an NH_3 and N_2 atmosphere under certain conditions or grown using the "two-temperature" (2-T) growth method form a network of interlinking InGaN strips with the center of the strips having a

higher indium content than the edge of the strips; it was also found that most threading dislocations terminated in the thinner region between the InGaN strips[95]. The 2-T growth method involves growing the InGaN QW layer at a lower temperature (720 °C) before linearly increasing the growth temperature to a higher temperature (860 °C) for the growth of the GaN barriers; during the temperature ramp, the InGaN QW layer is exposed to a NH_3 and N_2 atmosphere and no growth of GaN takes place. The 2-T growth method and annealing was reported to result in InGaN QWs with higher intensity emissions at room temperature compared to unannealed InGaN QWs grown under a single temperature. The unannealed InGaN QWs grown under a single temperature were reported to have no gross well width fluctuations[95]. Gross well width fluctuations were also observed by Narayan *et al.* in MOVCD grown InGaN MQW LEDs using TEM and TEM atomic number contrast techniques[96]. In addition, Oliver *et al.* used cathodoluminescence imaging with scanning electron microscopy to show bright emission from the InGaN strips on annealed InGaN QWs and APT to confirm that the center of the InGaN strips had a higher indium content compared to the edge of the strips and that most threading dislocations passed between the InGaN strips[65].

2.2 Non-radiative Recombination

The effect of non-radiative recombination can be seen in the PL of InGaN QWs by varying the temperature and the number of injected carriers. The integrated intensity of the PL spectra varies with excitation power; there are, of course, more carriers generated to recombine radiatively but the probability of radiative recombination is also carrier density dependent due to a number of effects, such as the screening of the QCSE, and the saturation of defects and localized states. The integrated PL intensity is typically proportional to the injected carrier density raised to a power index[108, 109]; by assuming that the injected carrier density is proportional to the excitation power density, the integrated PL intensity I can be related to the excitation power density P as:

$$I \propto P^m, \tag{2.1}$$

where a $m = 1$ linear relationship corresponds to complete radiative recombination. A $m > 1$ super-linear relationship has been observed at low excitation power densities at room temperature and has been attributed to the saturation of trap assisted non-radiative Shockley-Read-Hall (SRH) recombination of thermally delocalized carriers[108, 109]; the super-linear relationship has been observed to evolve into a linear relationship with increasing excitation power density as the traps become increasingly saturated. The exponential increase of integrated intensity with excitation power at low excitation power densities is characteristic of a non-radiative recombination pathway which does not increase with carrier density, and can be saturated. The traps responsible for SRH recombination has been attributed to threading dislocations[110].

At low temperature and low excitation power densities, there is a linear relationship, indicating that carriers remain localized and cannot move to traps. At high excitation power densities at both low and room temperature, a sub-linear $m < 1$ relationship have often been observed and indicates the presence of non-radiative recombination pathway(s) which becomes more accessible with increasing carrier density; this phenomena is referred to as efficiency "droop". The cause of droop in InGaN QWs is in contention and is further discussed in Section 2.2.1.

2.2.1 Efficiency Droop

The origins of efficiency droop in InGaN QW LEDs may not be solely intrinsic to InGaN QWs and may arise due to the presence of the p-type and n-type GaN layers in InGaN QW LEDs. The cause of efficiency droop in InGaN QW LEDs is widely debated and the main proposed mechanisms include: delocalization of carriers[7, 111, 6], Auger recombination[119, 114, 115] and carrier leakage[116]. Carrier leakage refers to phenomena in which carriers leave the QW active region without recombining; these include poor hole-injection efficiency, ineffective electron blocking layer, incomplete capture of carriers into QWs and carrier escape from QWs[117]. This section focuses on the intrinsic causes of efficiency droop: Auger recombination and the delocalization of carriers. Carrier escape from QWs, also a potential intrinsic cause of efficiency

droop, is referred to in Chapter 4.

Auger Recombination

In Auger recombination in semiconductors, an excited electron and hole pair recombine non-radiatively by transferring the excess energy to either another electron or hole, see Figure 2.3.

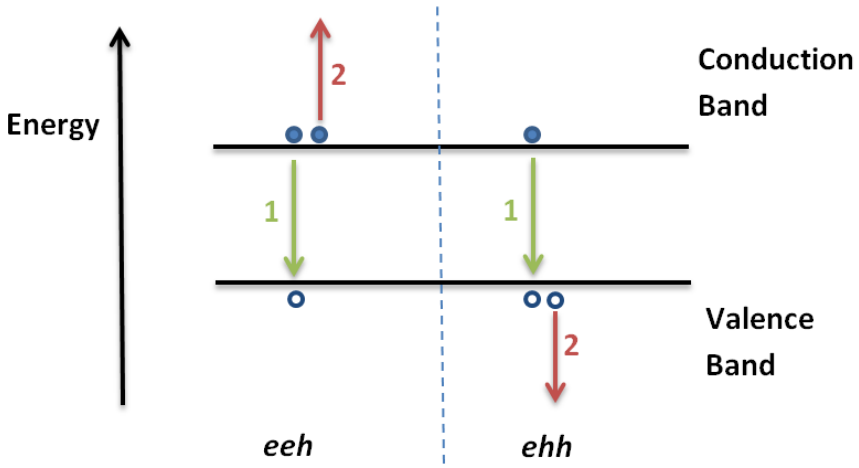

Figure 2.3: Auger recombination in semiconductors. The energy from carrier recombination is transfered to an electron (*eeh*) or a hole (*ehh*).

The rate of Auger recombination is approximately proportional to n^3, where n is the carrier density. The study of Auger recombination as a cause of efficiency droop in InGaN QWs is typically based on the "ABC" model, which gives the rate of change in carrier population as:

$$\frac{dn}{dt} = G - An - Bn^2 - Cn^3, \tag{2.2}$$

where G is the generation rate of the carriers, $-An$ represents SHR non-radiative recombination, $-Bn^2$ denotes bimolecular radiative recombination and $-Cn^3$ accounts for Auger non-radiative recombination. The ABC model has been used to fit experimental data from a number of continuous and time-resolved electro-luminescence and PL studies[119, 120, 121, 112, 123], giving an Auger coefficient C around the order of 10^{-29} cm^6 s^{-1} - 10^{-30} cm^6 s^{-1}. Theoretically, it has been

variously predicted that only an Auger coefficient $C > 10^{-31}$ cm^6 s^{-1} can cause efficiency droop[124], that direct Auger recombination in InGaN QWs is insufficient to account for efficiency droop[125] and that phonon-assisted Auger recombination can account for efficiency droop[126].

Attempts to directly observe the high energy carriers created by Auger recombination had been made by Iveland *et al.* and Binder *et al.*[115, 127]. Iveland *et al.* designed an InGaN/GaN QW LED with a layer of caesium deposited on the surface of the p-type GaN to engineer a conduction band minimum above the vacuum level at the surface, thus encouraging hot electrons transported to the surface of the p-side to escape into the vacuum where their energy distribution was analyzed using a Faraday cup[115]. The LED light emission was measured simultaneously to the energy distribution of the emitted electrons; Iveland *et al.* observed that high energy electron emission began with the onset of efficiency droop and attributed Auger recombination to be the main cause of efficiency droop. Binder *et al.* performed PL on an MQW test sample with varying green (520 nm) and ultraviolet (400 nm) QWs at 12 K using a 450 nm blue laser; they observed increasing ultraviolet luminescence simultaneously with the onset of droop from the sample[127]. Binder *et al.* attributed the luminescence mostly to hot electrons and holes created by Auger recombination in the green QWs escaping into the ultraviolet QWs and radiatively recombining[127].

Carrier Delocalization

Microscopic many-body modelling work by Hader *et al.* indicated that direct Auger recombination in InGaN QWs is insufficient to account for efficiency droop[125]. Later, Hader *et al.* proposed that efficiency droop is due to density-activated defect recombination (DADR) where increased carrier densities leading to the saturation of localized states allow carriers increasing access to defects acting as non-radiative recombination centres which otherwise would inaccessible due to localization[7]. They showed that a theoretical $(N - N_0)^2$ dependence of droop on the carrier density N and a DADR onset density N_0 corresponded to experimental results.

Cathodoluminescence images with a 5 nm spectral resolution of an

InGaN/GaN multiple QW wafer observed by Pozina *et al.* supports the DADR model. Their work shows the transformation of spatially uniform emission across the wafer to spatially separated areas of emission covered with dark spots and lines (indicating dislocations) when the electron beam current is increased. This corresponds to localization shielding carriers from defects at low currents and carriers being able to access defects at high currents[111].

The saturation of localized states with increasing carrier density is supported by the work carried out by Hammersley *et al.* on the PL of InGaN/GaN QWs; a reduction of the S-shape behaviour of the peak emission energy coinciding with efficiency droop was observed with increasing carrier density[6]. The authors attributed the suppression of the S-shape with increasing power density to the saturation of the localized states preventing the redistribution of carriers with temperature[6].

The saturation of deeply localized states was attributed as the origin of the high energy feature or high energy band in studies by Davies *et al.*, Sun *et al.* and Christian *et al.* on InGaN QWs at high carrier densities. Conversely, the high energy feature has also been observed by other studies in the droop regime and attributed to the recombination of carriers from excited sub-bands from which carrier leakage may occur[101], the recombination of high energy electron-hole plasma resulting from Auger recombination[104] and other proposals. The high energy band is more fully discussed in Chapter 5.

Chapter 3

Experimental Method

In photoluminescence spectroscopy, mono-energetic photons directed at a sample photo-excite electrons from the valency band states to the conduction band states, creating a hole in the valency band states. Excited electrons and holes may recombine radiatively or non-radiatively, with or without relaxing into lower energy states before they recombine. The PL intensity of the sample due to radiative recombination is measured as a function of photon energy using a spectrometer. In time-resolved PL, a short laser pulse is used to excite the sample and the emission of the sample is measured as a function of time relative to a start signal triggered by the laser pulse as well as a function of energy. Three independent experimental set-ups, termed A, B and C here, were used for this work. Setups A and B are described in Section 3.1 and setup C which was used for time-integrated photoluminescence (TIPL) spectroscopy and time-resolved PL spectroscopy is described in Section 3.2.

3.1 Setup A and B for TIPL

A 30 mW and a 3 mW helium cadmium (HeCd) laser were used in setups A and B respectively to emit light at 325 nm to photo-excite carriers in the sample; this excited carriers in the GaN barrier. In both setups, the laser beam was passed through a plasma filter to reduce plasma lines and a neutral density (ND) filter to reduce the laser power before being focused onto the sample, see Figure 3.1.

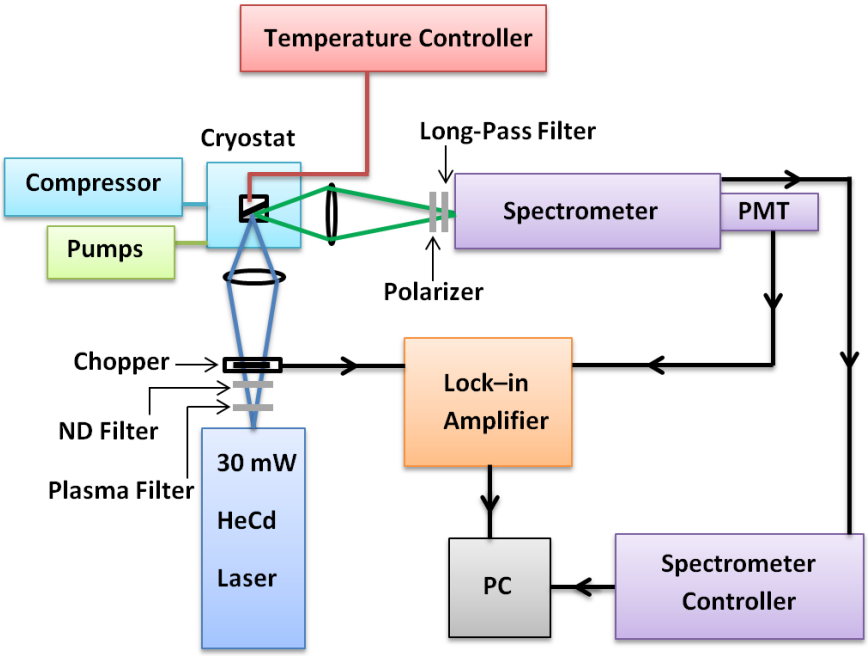

(a)

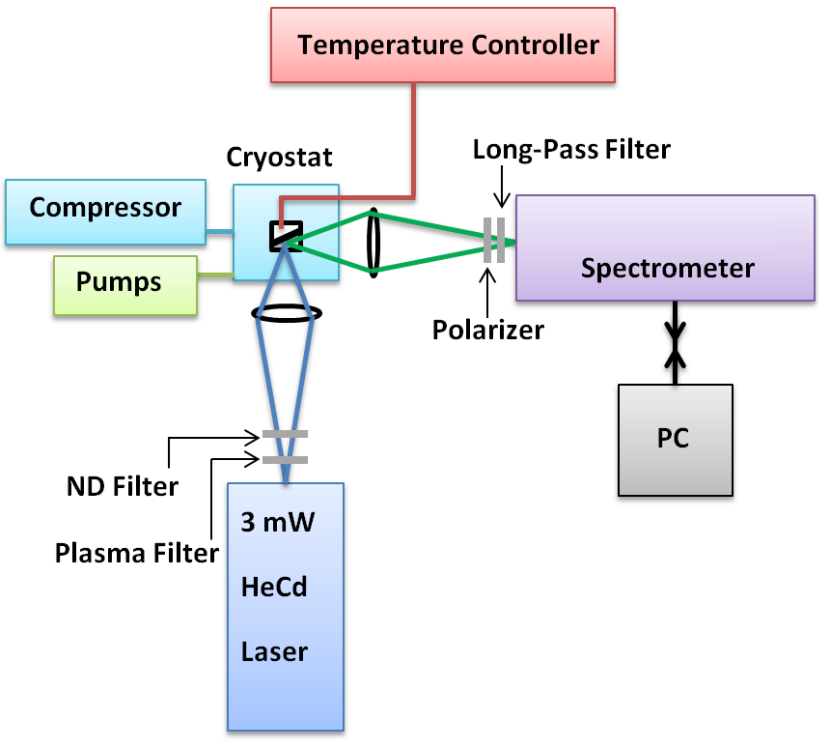

(b)

Figure 3.1: Schematic representations of the photoluminescence spectroscopy (a) setup A and (b) setup B.

In setup A, the laser was modulated by a mechanical chopper before reaching the sample. The use of different ND filters allowed the power of the laser beam to be varied. The sample was mounted on an oxygen-free copper plate inside a closed-cycle refrigerator cryostat in both setups; the cryostat was evacuated by pumps and cooled by the Joule-Thomson expansion of helium gas down as low as 10 K for low temperature experiments. In both setups, thermocouples and resistive heaters mounted close to the sample allowed the temperature of the sample to be monitored and controlled. The luminescence from the sample was focused by a collection lens onto a double-grating SPEX 1404 0.85 m spectrometer in setup A or a Horiba iHR550 Fully Automated Imaging Spectrometer in setup B. In both setups A and B, the sample was mounted at a Brewster angle geometry relative to the spectrometer, see Figure 3.2, and the luminescence was passed though a polariser and a edge filter before reaching the spectrometer; the edge filter prevented the laser emission from entering the spectrometer.

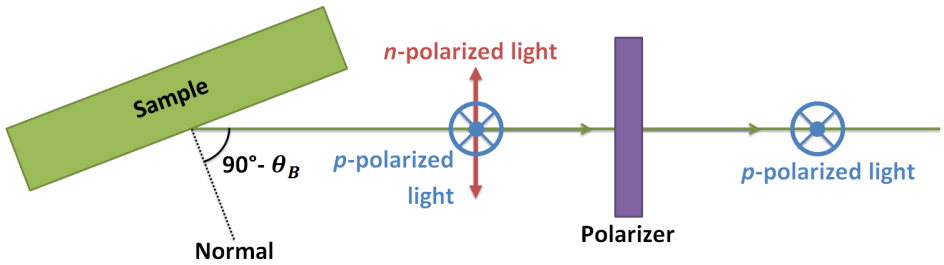

Figure 3.2: Diagram depicting the orientation of the sample relative to the optical axis of light emission propagating from the sample to the spectrometer. The fluctuating electric field of the p-polarised light is directed into and out of the plane of the page. θ_B is the Brewster angle.

In an InGaN/GaN QW sample with a sapphire substrate, the different refractive indices at the sapphire/GaN and GaN/air interfaces cause the QW sample to act as a cavity for the photoluminescence of the QW; the multiple reflections produces Fabry-Pérot interference fringes in the emission spectra of the sample. At a critical angle of incidence (the Brewster angle) the reflectivity at the GaN/air interface is zero for p-polarised light, unlike for n-polarised light, such that the p-polarised

light does not undergo constructive and destructive interference to form Fabry-Pérot fringes. The Brewster angle θ_B which is given by:

$$\theta_B = \tan^{-1}\left(\frac{n_{air}}{n_{GaN}}\right), \tag{3.1}$$

where n_{air} is the refractive index of air and n_{GaN} is the refractive index of GaN. For light at a wavelength of 520 nm, GaN has a refractive index of 2.43[139]; this gives a Brewster angle of 22.4°. The external angle shown in Figure 3.2 is related to the Brewster angle of incidence at the GaN/air interface by Snell's law. The p-polarised photoluminescence from the sample is set apart from the n-polarised photoluminescence by the polariser in front of the spectrometer.

In setup A, the spectrometer directed photons of designated wavelengths into a Peltier cooled gallium arsenide photomultiplier tube (PMT) which detected the intensity of the photons and converted it to a signal; noise was reduced from the resulting signal by using a phase sensitive (lock-in) amplifier which was referenced to the frequency and phase of the mechanical chopper. The mechanical chopper modulated the light from the laser at a controllable frequency, resulting in an excitation intensity pattern, and hence sample light emission intensity pattern, close to a square wave. A synchronous reference signal from the mechanical chopper was sent to the lock-in amplifier; the lock-in amplifier multiplied the input signal from the detector with the reference signal from the mechanical chopper and hence removed the (unmodulated) noise on the resulting output signal. The computer then recorded the output signal as a function of the detection wavelength.

In setup B, the spectrometer dispersed photons of different wavelengths onto a Syncerity deep cooled Open Electrode 1024 x 256 charge couple device (CCD) Camera with a multichannel array detector that can record the intensities of light at multiple wavelengths simultaneously; light of different wavelengths was incident on different channels of the array and the intensity as a function of wavelength was measured by the CCD and recorded in a computer.

3.2 Setup C for TRPL

Setup C was used for carrying out PL time decay and TRPL measurements by using time-correlated single-photon counting. A frequency doubled neodymium-doped yttrium aluminum garnet (Nd:YAG) laser emitting at 532 nm was used to pump a mode-locked, pulsed titanium sapphire (Ti:Sapphire) laser emitting at 800 nm with a 80 MHz repetition rate and 100 fs pulses, see Figure 3.3. The laser was then modulated by an acoustic optical modulator (AOM) which acted as a pulse picker by diffracting light periodically and was triggered by an alternating current signal; this signal was also sent to a time to pulse height converter (TPHC) via a delay box and acted as the start signal. The beam path then passed through a frequency tripler which used a second harmonic generator to obtain emission at 400 nm which was sum frequency mixed with the fundamental wavelength to obtain light emission at 267 nm. A prism was used after the frequency tripler to the separate the 800 nm, 400 nm and 267 nm components; the fundamental and second harmonic components were discarded. A ND filter holder and a flip-mounted power meter were placed in the beam path of the pulsed, frequency-tripled beam to alter and monitor the power of the beam. The beam was then focused onto the sample, which was mounted on an oxygen-free copper plate inside a closed-cycle refrigerator cryostat at a Brewster angle geometry relative to the spectrometer, similar to setups A and B.

Photoluminescence from the sample was focused onto the slits of a single-grating spectrometer after passing through an edge filter which removed light from the excitation source. The spectrometer directed photons of a designated wavelength into a Peltier cooled gallium arsenide PMT which converted the photons into an electric signal. This signal was amplified by the pre-amplifier, passed through the constant fraction discriminator (CFD) and then used as a stop signal by the TPHC. The CFD improved the signal-to-noise ratio by imposing a discriminator level and removed timing errors due to different pulse heights using constant fraction triggering; an incoming signal would have been divided into two signals, with one of the signals delayed by a set amount of time and then deducted from the non-delayed signal. At the point where the resulting

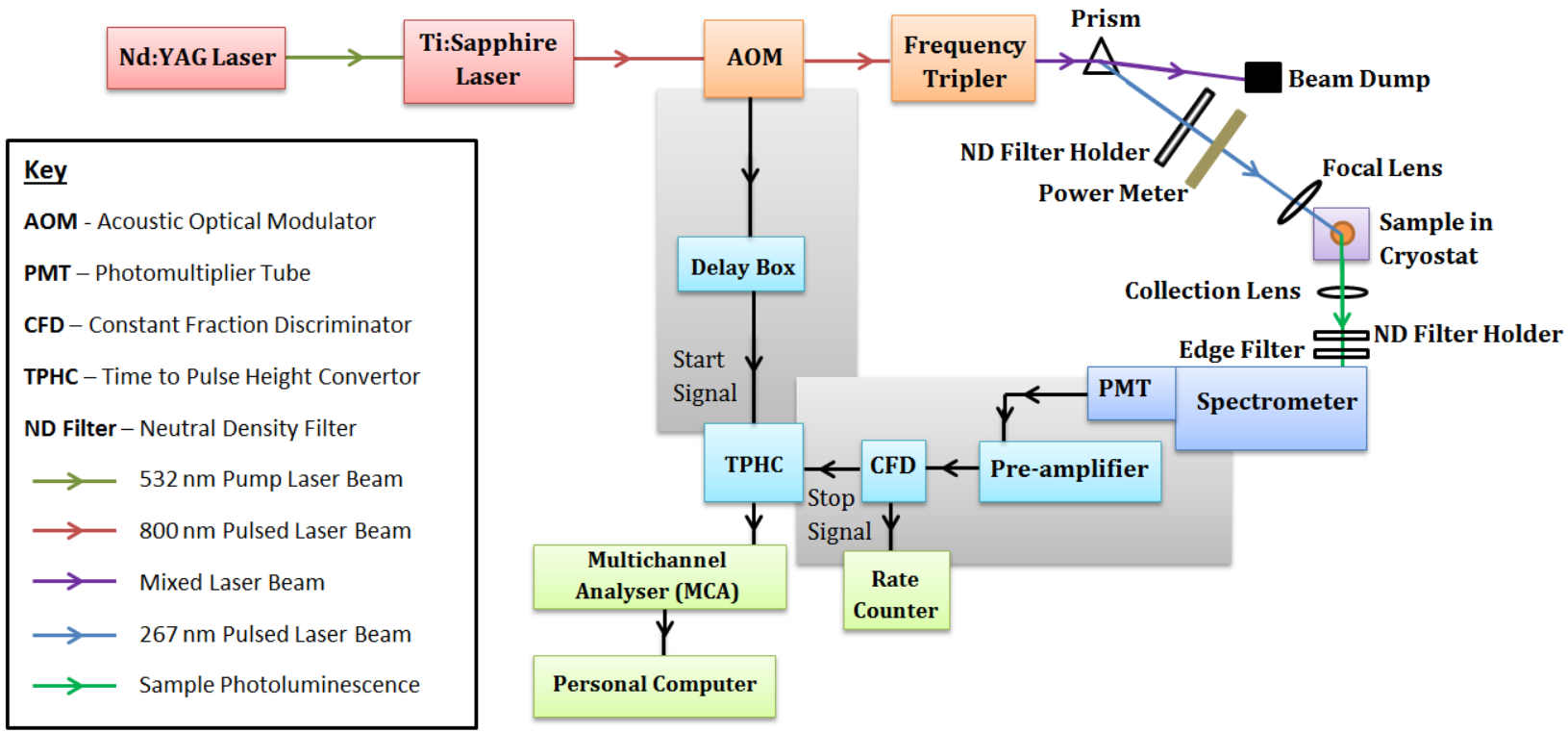

Figure 3.3: Schematic representations of setup C used for time-correlated single-photon counting lifetime measurements.

signal crossed zero, the CFD would have output a signal to the TPHC, allowing incoming signals of different sizes to be perceived at the same fraction of their total pulse height, see Figures 3.4 and 3.5.

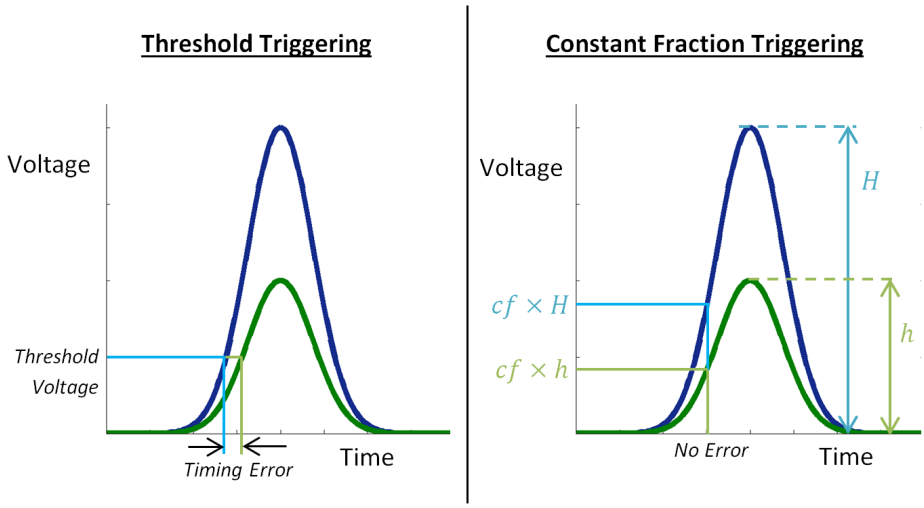

Figure 3.4: Stop signals with different pulse heights will generate a timing error using threshold triggering but not with constant fraction cf triggering.

The TPHC started a voltage ramp when the start signal arrived from the AOM and ended the voltage ramp when a stop signal arrived from the PMT, effectively measuring the time taken from when a laser pulse was triggered by the AOM to the when a signal triggered by PL from the sample was detected. The multichannel analyser (MCA) sorted electric pulses from the TPHC into voltage (time) channels and sent this to the personal computer (PC) which recorded the counts for each voltage (time) channel, allowing the change of photoluminescence from the sample to be observed as a function of time for a designated emission wavelength. The delay box which could delay the start signal before it arrived at the TPHC allowed adjustments to the time window to be made. To prevent erroneous measurements due to a pulse pile-up where multiple photons per laser excitation pulse are detected by the PMT, ND filters were typically placed in front of the spectrometer slits to maintain a PL detection rate to below 1 % of the excitation rate; the PL detection rate was monitored via the rate counter. For TRPL spectroscopy, PL time decay measurements were carried out across a range of wavelengths

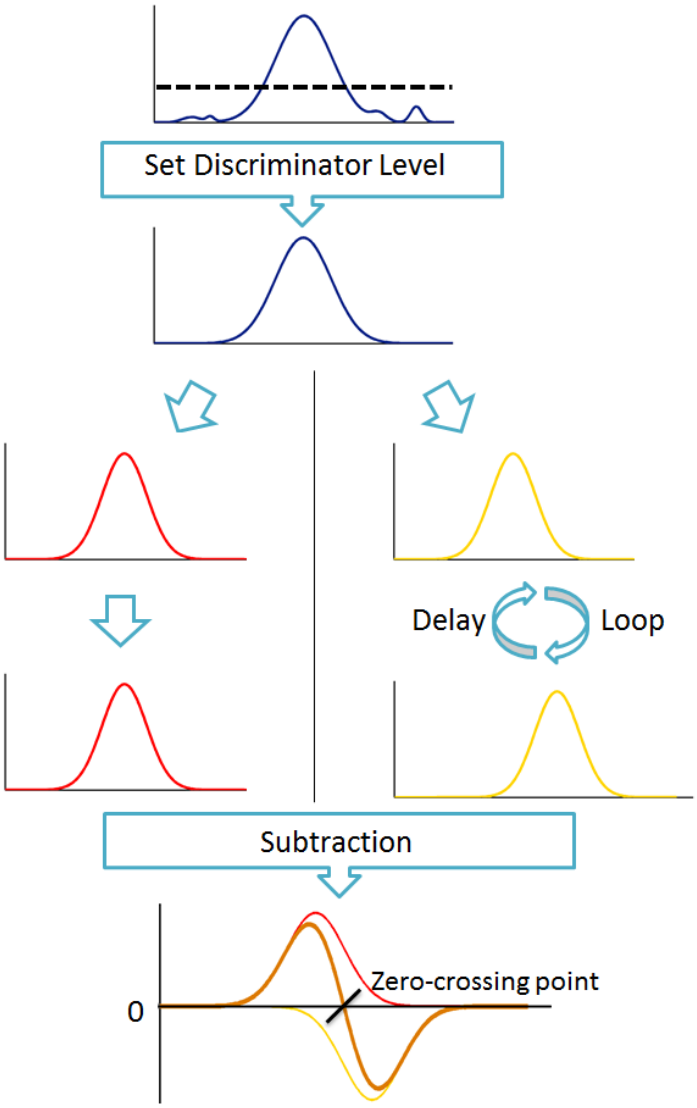

Figure 3.5: Schematic representation of the signal processing carried out by the constant fraction discriminator.

and combined to generate time-varying PL spectra.

When time-integrated photoluminescence spectroscopy (TIPL) was carried out using setup C, the timing electronics were disconnected from the system, a polariser was positioned in front of the spectrometer slits and a mechanical chopper was placed before the focal lens in the excitation beam path and used in conjunction with a lock-in amplifier to improve the signal-to-noise ratio of the PL detected, similar to setup A.

Chapter 4

Varying the Number of QWs in Green InGaN/GaN QW samples

4.1 Introduction

This chapter describes investigations carried out on a series of green light emitting InGaN/GaN QW samples with a different number of QWs to determine if increasing the number of QWs in green light-emitting InGaN/GaN QW samples increases internal quantum efficiency at carrier densities which do not trigger droop; this would contribute to determining the optimal number of QWs in an LED device. Compared to blue light-emitting InGaN/GaN QWs, the increased indium content required to produce green light-emitting InGaN/GaN QWs leads to more defect formation, increased QCSE and a greater QW energy barrier[4]. As described below, previous studies have demonstrated that increasing the number of QWs in blue InGaN/GaN QW active regions leads to an increase in light emission but little work has been carried out on green light-emitting InGaN QWs.

Hurst *et al.* measured the temperature dependent photoluminescence intensity of five blue light emitting $In_{0.14}Ga_{0.86}N$/GaN QW samples with 2-18 QWs; the lifetimes of the 2 QW and 10 QW samples were also measured as a function of temperature[140]. It was observed that the photo-

luminescence intensity and lifetime reductions with increasing temperature were less severe for the samples with a greater number of QWs and this was attributed to samples with fewer QWs experiencing increased thermally excited carrier escape from the QWs.

Schubert *et al.* demonstrated the escape of carriers from the InGaN/GaN QW region in LEDs by selectively exciting carriers in the QW using a 405 nm laser under short circuit and open circuit conditions; they observed that under short circuit conditions, light emission only occurred at the laser excitation spot but in open circuit conditions, light was emitted from the entire LED chip[118]. This open circuit behaviour was attributed to excited carriers escaping the QW region into the p-type and n-type regions where they accumulated and then redistributed across the plane of the LED before returning to the QW active region and recombining radiatively across the whole area of the LED chip. Under short circuit conditions, where the p-type and n-type regions were connected electrically, the escaped carriers did not accumulate at the p-type and n-type regions of the LED.

Laubusch *et al.* investigated the effect of increasing the number of QWs in a sample with respect to droop[122]. They performed electroluminescence on single InGaN/GaN QW LEDs of varying well thicknesses and a InGaN/GaN MQW LED which were designed to emit at 400 nm. It was observed that efficiency droop was reduced for the MQW LED compared to the single QW LEDs; the authors attributed this to a reduced carrier density in the active region of the MQW LED since the carriers were divided between more quantum wells.

Hospodková *et al.*, who studied InGaN/GaN QW samples with different number of QWs for scintillation, carried out atomic force microscopy (AFM), PL and CL measurements on two $In_{0.06}Ga_{0.94}N$/GaN QW samples; one sample had two series of 5 QWs separated by a 25 nm GaN partition layer and the other sample had six series of 5 QWs each separated by a 25 nm GaN partition layer[133]; Figure 4.1 shows a schematic comparing these two samples. In the study, only the top 10 QWs of both samples were excited in their PL and CL measurements such that the injected carrier density per QW would be the same for both samples; they observed that the sample with 6 X 5 QWs emitted greater luminescence

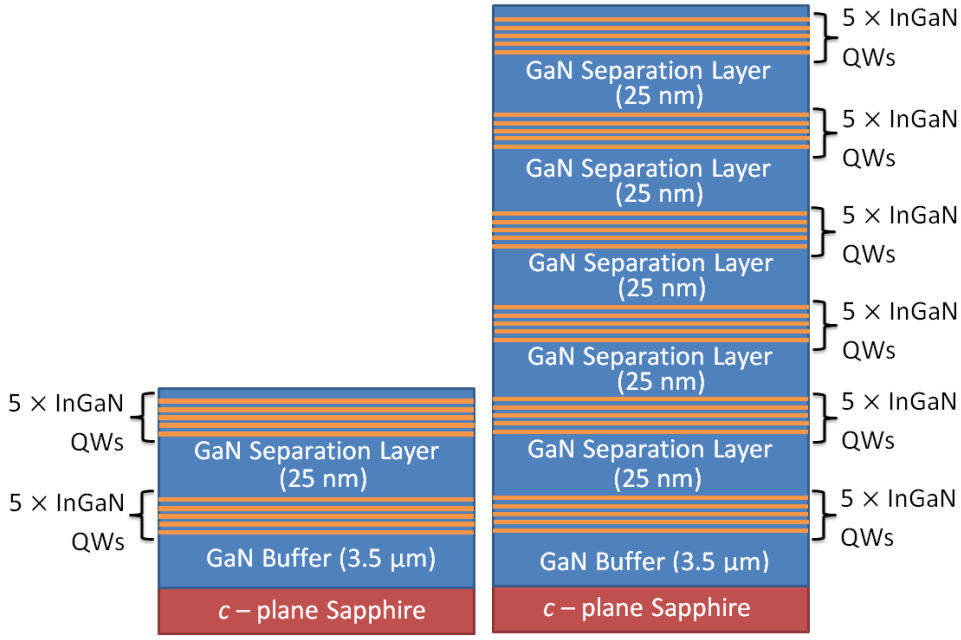

Figure 4.1: Schematic representation of the InGaN/GaN QW samples studied by Hospodková *et al.*[133]. The 2 × 5 QW sample shown on the left of the diagram had a 110 nm thick active layer and the 6 × 5 QW sample shown on the right of the diagram had a 360 nm thick active layer.

in both the PL and CL measurements. AFM results showed that the 6 X 5 QW sample exhibited V-pits with a greater diameter than in the 2 X 5 QW sample. The authors attributed the increased PL and CL in the sample with a greater number QWs to the presence of larger V-pits with increased QW number which increased the suppression of dislocations-related non-radiative recombination, as proposed by Hangleiter[93].

In this investigation, power and temperature dependent TIPL and transient PL measurements at 10 K were conducted on InGaN/GaN QW samples to study the effect of varying the number of QWs in green-emitting sample. Previous investigations have been carried out on the same samples studied in this work by Othick who performed temperature dependent PL on the samples and fitted the data with an Arrhenius equation to determine the activation energies of the samples[132]. It was observed that the 1 QW sample had a greater activation energy (78 meV) compared to the samples with more QWs (20 - 30 meV). Othick proposed

that the activation energy in the 1 QW sample was equivalent to the electron confinement energy relating to the thermal escape of electrons out of the QW and the activation energies in the multiple QW samples were equivalent to the exciton binding energy relating to the disassociations of excitons with temperature. Hence the thermal escape of electrons out of the QWs was not the dominant thermally activated non-radiative carrier loss mechanism in the MQW samples. It was also noted that the use of a HeCd laser emitting at 325 nm would have a limited $\frac{1}{e}$ penetration depth of 85 nm in GaN and may not be sufficient to probe the lower QWs of the 10 QW sample[132].

4.2 Sample Details

Table 4.1: Sample details of the InGaN/GaN QW series with a varying number of QWs.

Sample	**No. of QWs**	**Growth Temperature of the QW(s) in order of growth**
C3859	1	710 °C
C3860	3	710 °C, 705 °C, 700 °C
C3861	5	710 °C, 705 °C, 700 °C for the top two QWs
C3862	10	710 °C, 705 °C, 700 °C for the top seven QWs

In this investigation of the effect on internal quantum efficiency of varying the number of quantum wells in green InGaN QW samples, the wurtzite samples were grown on (0001) sapphire substrates in a Thomas Swan 6 × 2 inch Close Coupled Showerhead MOCVD reactor at the University of Cambridge[132]. The V/III ratio used during the growth of the InGaN QWs was 23450. All growth conditions except from the number of QWs and the QW growth temperature were the same for all samples. The samples were grown using a modified version of the two temperature (2-T) growth method in which the InGaN QWs were grown at a lower temperature (700 °C - 710 °C) and the GaN barriers were grown at a

higher temperature (860 °C); the first QW of each sample were grown at 710 °C, the second QW of each sample were grown at 705 °C and the subsequent QWs of each sample were grown at 700 °C, see Table 4.1. The temperature ramp occurred over 60 seconds during which no growth took place. The temperature-varying growth conditions were designed to reduce the variations in indium content between the QWs during growth. The samples have a nominal 25 % indium composition and peak emissions around 2.4 eV at 10 K. A schematic of the samples and a scanning transmission electron microscope - high-angle annular dark-field (STEM-HAADF) image of the sample C3862 are shown in Figure 4.2.

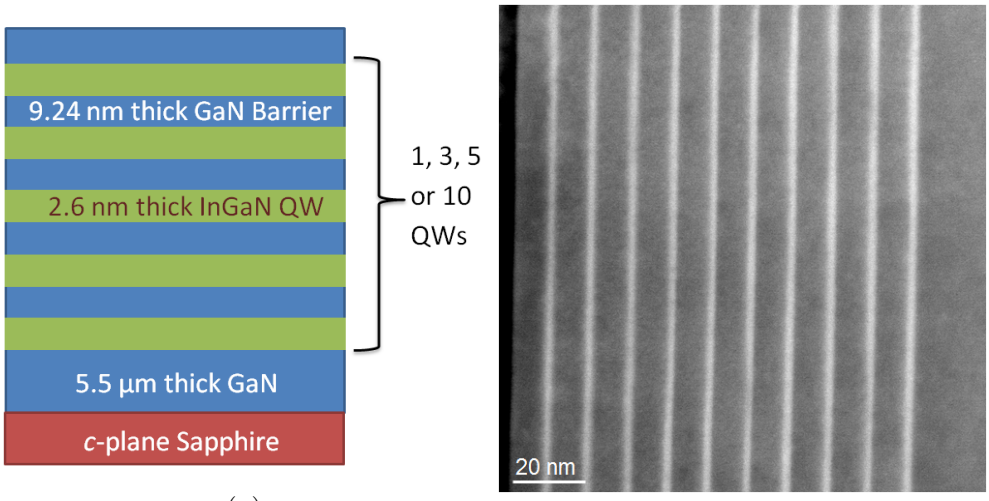

(a) (b)

Figure 4.2: (a) Schematic depicting the structure of the QW samples C3859, C3860, C3861 and C3862. (b) STEM-HAADF images of the sample C3862[134].

Analysis of the STEM-HAADF image of the sample C3862 measured the average quantum well thickness as 2.6 ± 0.5 nm and average barrier thickness as 9.24 ± 0.16 nm; this is consistent with the x-ray diffraction (XRD) measurements also performed on the sample C3862 which measured the average quantum well thickness as 2.25 ± 0.10 nm, average barrier thickness as 8.85 ± 0.10 nm and average QW indium composition as 18.3 ± 1 %. The thickness of each QW layer in the sample C3862 is shown in Figure 4.3; it appears that the initial three QWs grown are slightly thicker than the rest of the QWs and that, for the first QWs,

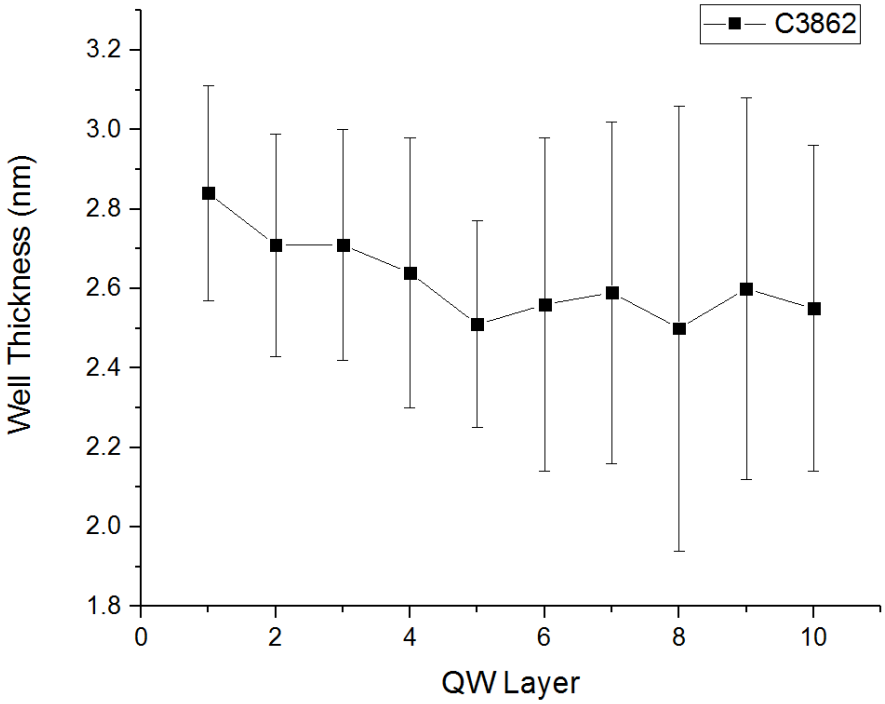

Figure 4.3: The QW thicknesses of the sample C3862 as a function of QW layer growth order[134].

the average QW thickness decreases with the sample growth number. The STEM-HAADF and XRD data were all obtained and analyzed by colleagues at the University of Cambridge[134].

4.3 Results and Discussion

4.3.1 Initial Optical Characterization

The PL spectra of the samples taken at 300 K under an excitation power density of 10 W cm^{-2} are shown in Figure 4.4. The 10 QW sample has a slightly higher emission peak energy than the 3 QW and 5 QW samples, which have similar emission peak energies; the 1 QW sample has a slightly lower emission peak energy than the 3 QW and 5 QW samples. The spectra of the samples have similar full-width half-maximum (FWHM) of around 0.15 eV to 0.16 eV with no clear trend with respect to the number of QWs. The variations of the peak emission energy amongst the

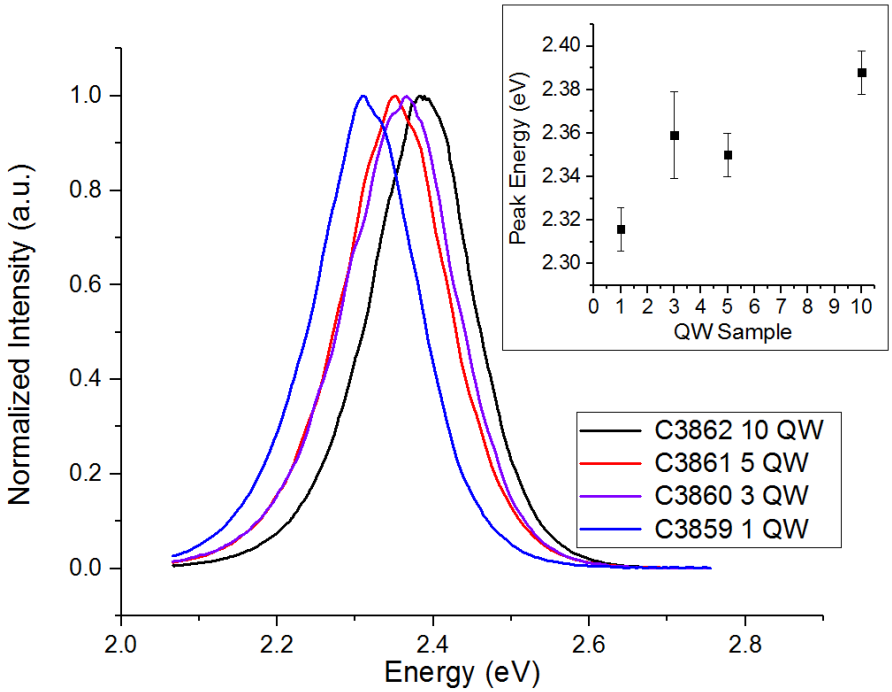

Figure 4.4: The PL spectra of the C3859 - C3862 samples at 300K under an excitation power density of 10 W cm^{-2}; the inset shows the peak energy of the samples.

samples could be indicative of a different level of indium incorporation in the samples with the 3 QW and 5 QW samples having a similar indium fraction and the 1 QW and 10 QW samples having a greater and lesser indium fraction, respectively. Additionally, the peak emission energy variation amongst the samples may be due the samples with more QWs having, on average, thinner QWs, see Figure 4.1. Furthermore, the 10 QW sample may be strain-relaxed, leading to a reduced QCSE and a blueshift in the peak energy. All three possibilities could contribute to a reduced QCSE and a blueshift of the peak emission energies in the samples with more QWs.

The 10 K PL time decay measurements taken at the peak emission energies of the samples show that the carriers decay at different rates in the 1 QW and 10 QW samples compared to the 3 QW and 5 QW samples, see Figure 4.5. The time taken for the carrier population to decrease to a tenth of the initial population is given by 222 $\pm$ 6 ns, 111 $\pm$ 3 ns,

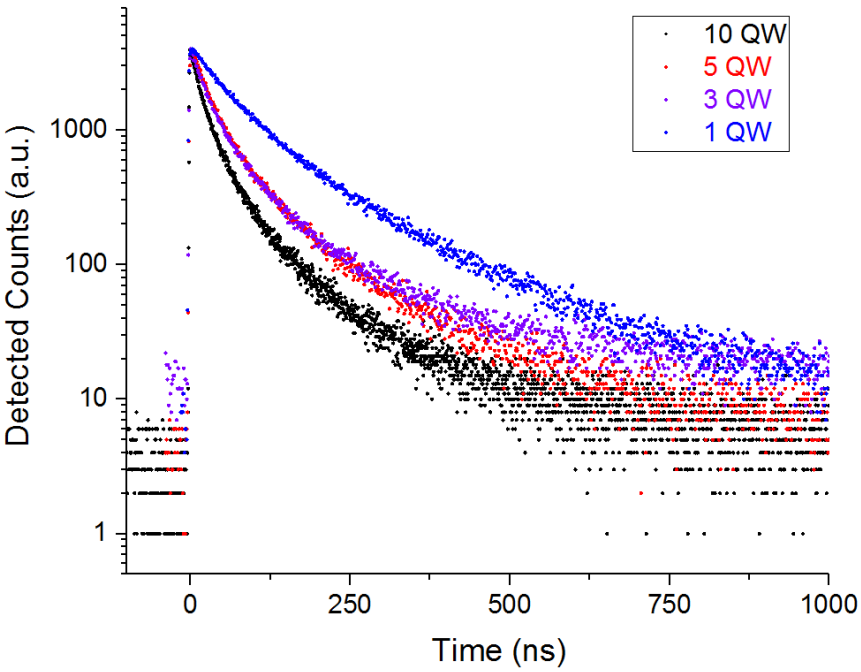

Figure 4.5: PL time decay measurements of the C3859 - C3862 samples taken at 10 K, at their peak emission energy.

112 ± 4 ns and 73 ± 3 ns for the 1, 3, 5 and 10 QW samples respectively; the 3 and 5 QW samples have similar decay curves, whereas the 1 QW sample has a slower decay and the 10 QW has a faster decay. The decays are not mono-exponential, which is characteristic of InGaN QW samples as carriers occupy multiple localized states. Again, the PL time decay measurements supports that there is a different indium content, average well widths or levels of strain amongst the QW samples leading to a reduced QCSE and hence an increased electron-hole wavefunction overlap and reduced carrier lifetimes in the samples with more QWs.

4.3.2 Temperature Dependent PL Spectra

To determine the decrease in IQE with temperature, temperature dependent PL was performed on the samples at 10 W cm^{-2}, see Figures 4.6 and 4.7.

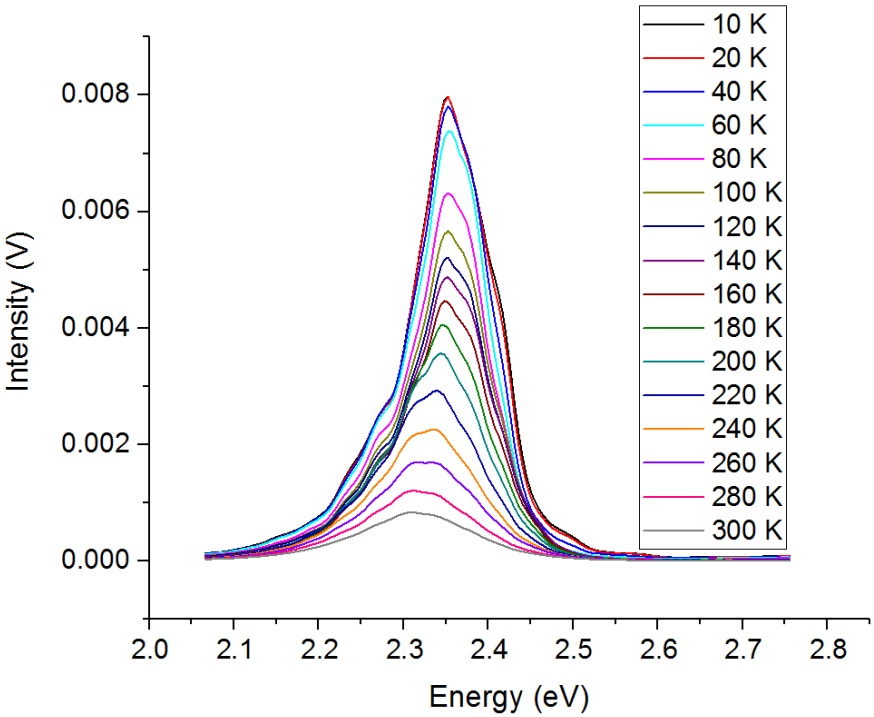

(a)

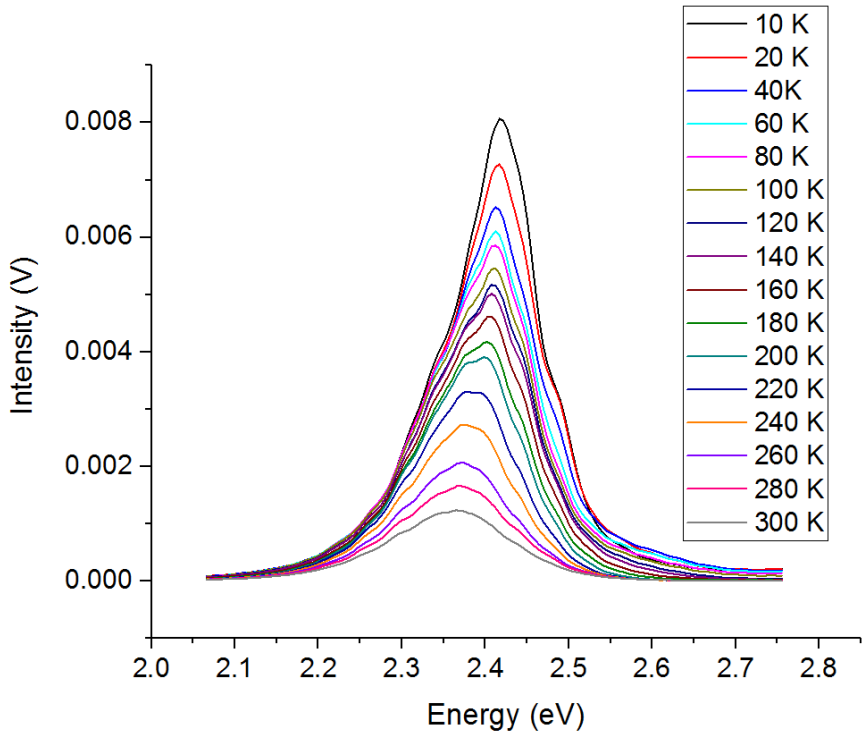

(b)

Figure 4.6: Temperature dependent spectra of (a) the C3859 1 QW sample and (b) the C3860 3 QW sample measured at 10 W cm^{-2}.

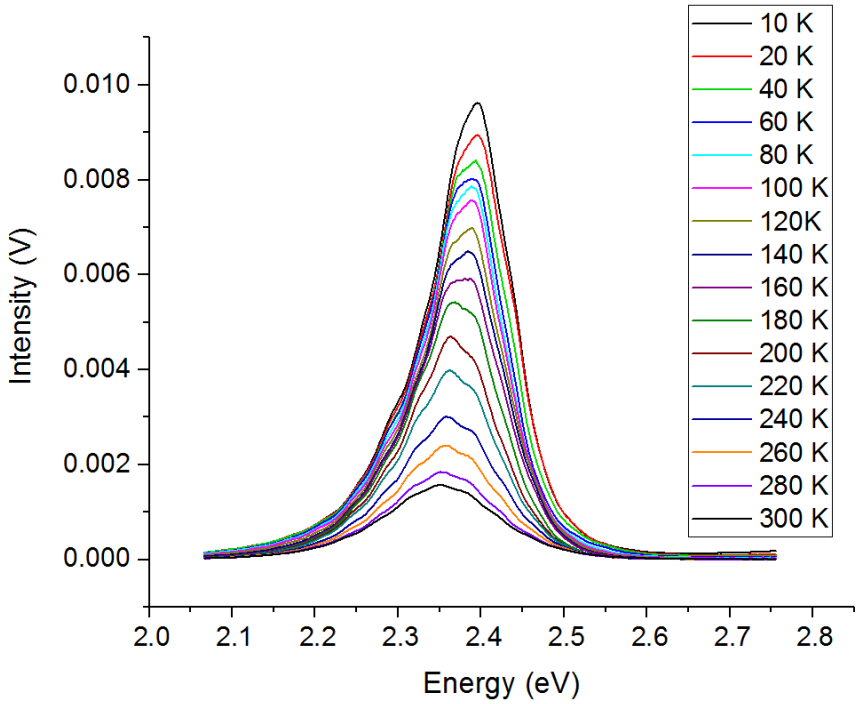

(a)

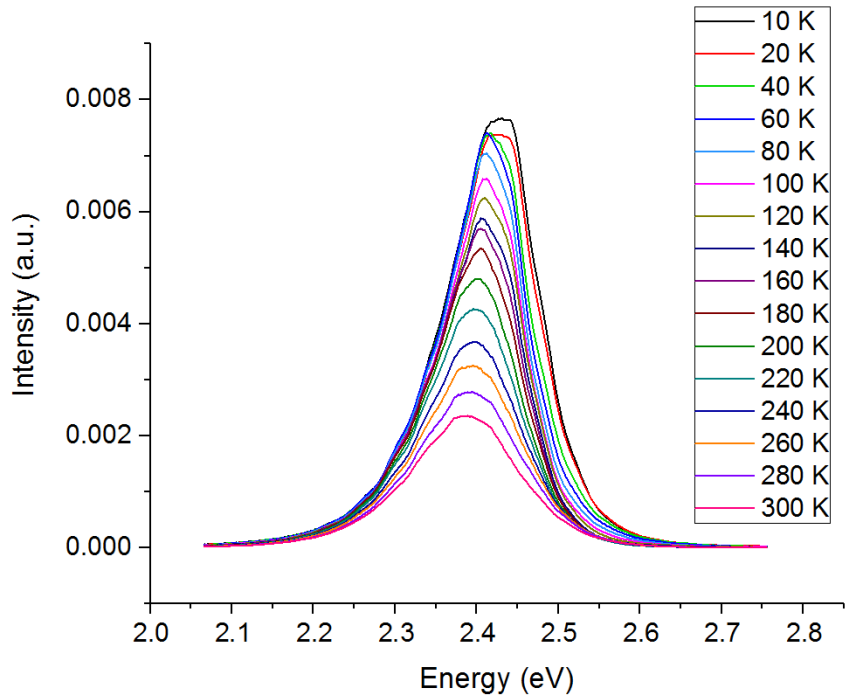

(b)

Figure 4.7: Temperature dependent spectra of (a) the C3861 5 QW sample and (b) the C3862 10 QW sample measured at 10 W cm^{-2}.

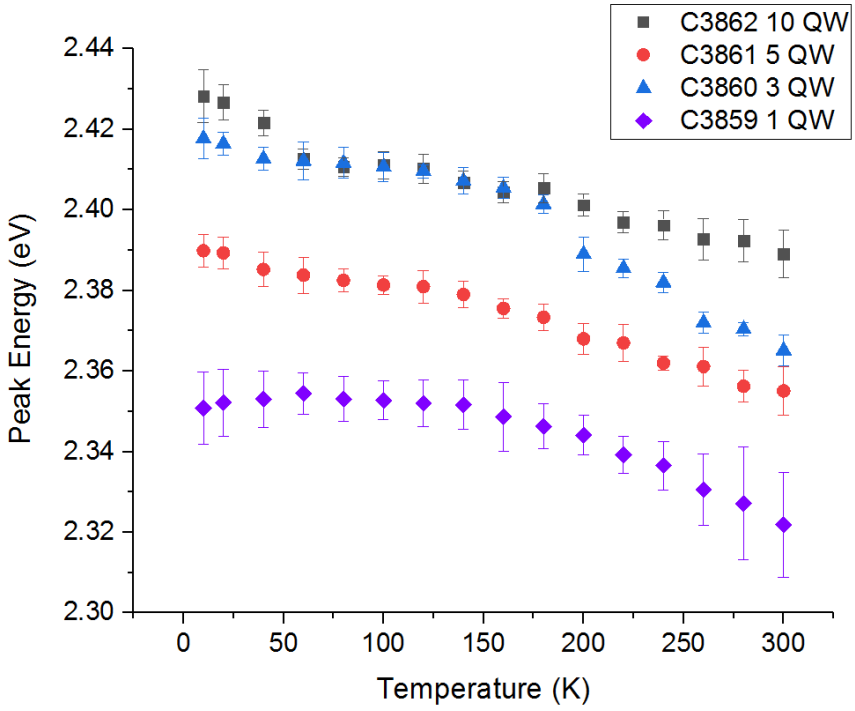

(a)

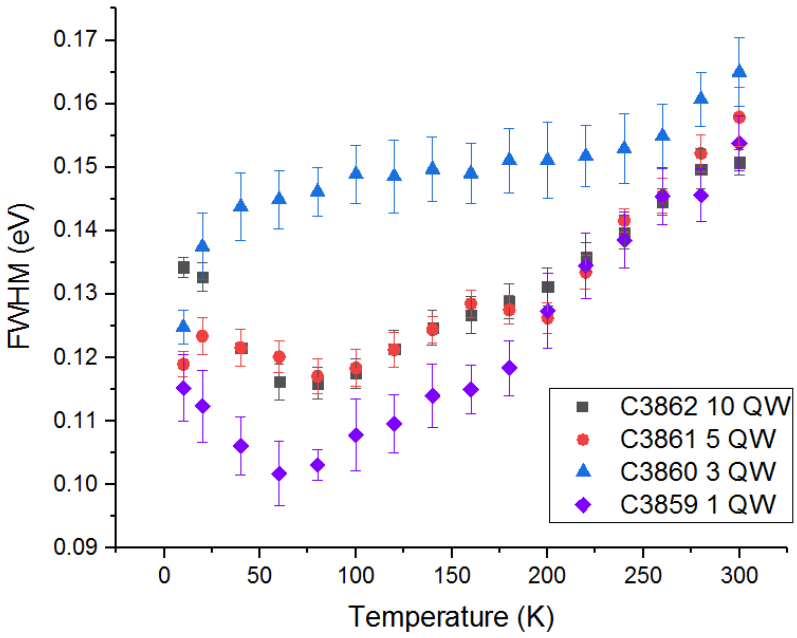

(b)

Figure 4.8: The peak energy and FWHM of the temperature dependent PL spectra shown in Figures 4.6 and 4.7

Some Fabry Pérot interference can be observed in all the spectra in Figures 4.6 and 4.7; the oscillations makes it difficult to accurately determine the peak energy of the PL emission spectra but it can be seen that the peak energy redshifts with increasing temperature, see Figure 4.8, as typically observed in the band gap of semi-conductors with increasing temperature due to the expansion of the lattice which reduces the potential energy of the charge carriers.

The FWHM of the 3 QW spectra increases monotonically with increasing temperature. The FWHM in the spectra of the 1, 5 and 10 QW samples initially decreases with temperature, reaching a minimum between 60 K to 80 K, and then increasing with temperature above this minimum; this is consistent with the carriers redistributing with increasing temperature, see Figures 4.8 and 4.9. At 10 K, the carriers are randomly distributed amongst the localized states. As the temperature increases between 10 K to around 70 K, carriers are thermally excited out of the most weakly localized states into the more strongly localized states which leads to a contraction in the FWHM of the emission spectra, see step 1 in Figure 4.9. The reduction in FWHM is less pronounced for the 5 and 10 QW samples compared to the 1 QW sample and is absent for the 3 QW sample. This could be due to the variation of QWs in the MQW samples; the superposition of the different FWHM behaviour of each QW in the MQW samples may have obscured the reduction in the FWHM. This difference in behaviour could arise either from different QW thicknesses, indium content or because the carriers are not quite distributed evenly between the QWs, as was assumed above. Above roughly 70 K, the localized carriers gain sufficient energy to escape from the moderately localized states which allows the carriers to redistribute to both more weakly and more strongly localized states, resulting in the broadening of the PL spectra, see step 2 in Figure 4.9.

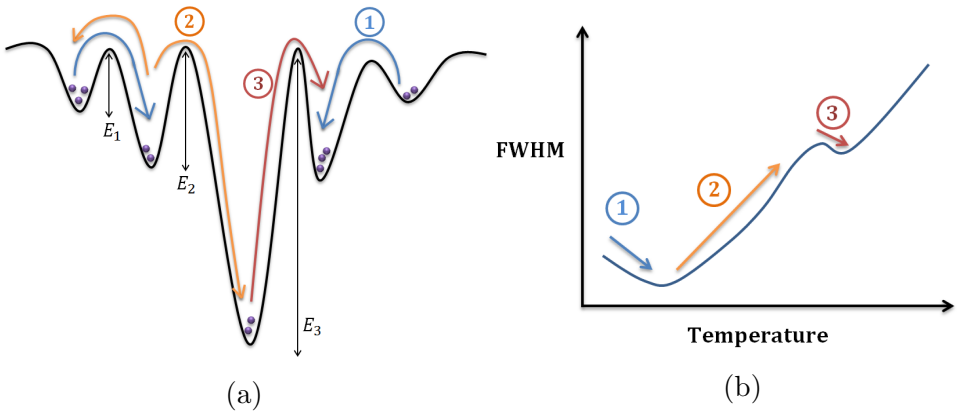

Figure 4.9: Diagram showing the redistribution of carriers responsible for the "W-shape" FWHM behaviour with increasing temperature. Potential fluctuations with different energies E_1, E_2 and E_3 are shown in (a). The purple spheres represent carriers. The corresponding change in FWHM with temperature is shown in (b) with labels for steps 1,2 and 3.

In temperature dependent PL carried out in other studies [108, 142, 143], an inflection in the FWHM with temperature, marked out as step 3 in Figure 4.9, have been observed; this corresponds with carriers being thermally excited out of the deepest localized states into more weakly localized states simultaneously with the processes marked out in steps 1 and 2. This reported "W-shape" of the FWHM and the reported "S-shape" of the peak energy, see Section 2.1.1, have not been observed in the spectra of the samples, possibly as the carrier density is sufficiently high to inhibit part of the carrier redistribution process[108].

The IQEs of the samples with increasing temperature, at an excitation power density of 10 W cm^{-2} shown in Figure 4.10, were determined by dividing the integrated intensities of the spectra shown in Figures 4.6 and 4.7 at a given temperature by the integrated intensities of the spectra at 10 K; this assumes that the IQE of the samples are 100 % at a temperature of 10 K and cannot delocalize and move to non-radiative recombination centres so that only radiative recombination occurs. In Figure 4.10, the decrease in IQE with temperature is significantly less for the 10 QW sample compared to the other samples, the 3 QW and 5 QW samples have a similar reduction in IQE with temperature and the 1 QW sample has the greatest decline of IQE with increasing tempera-

ture. If thermionic emission is significant, the IQE may be expected to decrease less with increasing temperature for samples with more QWs due to an increased probability of recapture of escaped carriers. However, the different carrier densities per QW in the samples may also have affected the IQE, and so this was studied in depth.

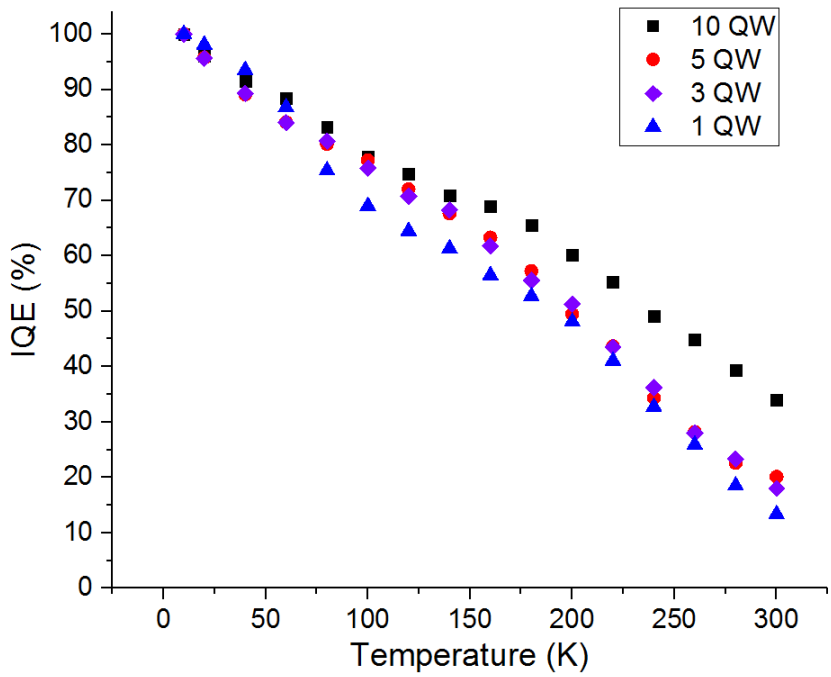

Figure 4.10: The internal quantum efficiency (IQE) of the QW samples C3859 - C3862 as function of temperature at a power density of 10 W cm^{-2}.

4.3.3 10 K Power Dependent PL Spectra

Power dependent TIPL was performed on the samples over a wide range of excitation energies at 10 K, see Figures 4.11, 4.12 and 4.13, both to establish when droop becomes significant and also to allow, by comparison, the determination of IQE at 300 K. In the spectra, it can be seen that the intensity of the QW emission escalates with increasing excitation power density as the carrier density in the QWs is increased.

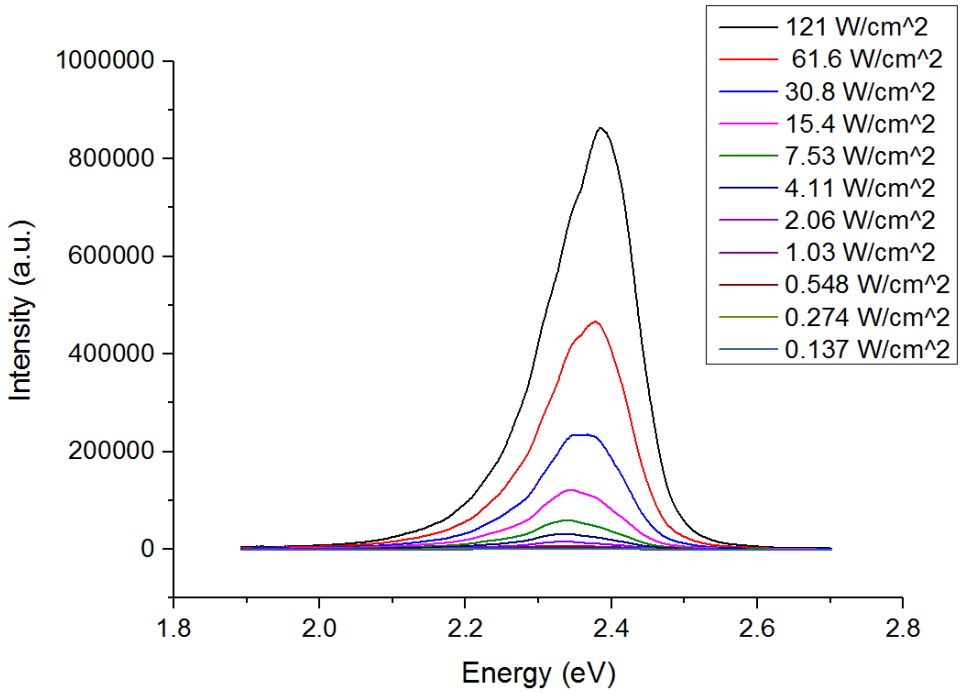

(a)

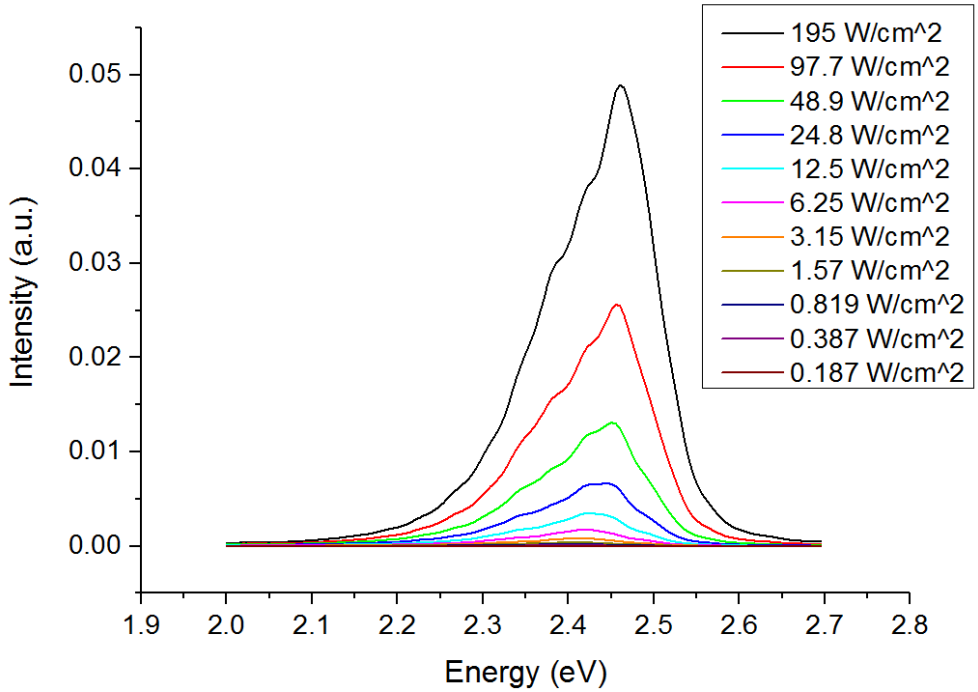

(b)

Figure 4.11: Power dependent spectra of (a) the C3859 1 QW sample and (b) the C3860 3 QW sample measured at 10 K.

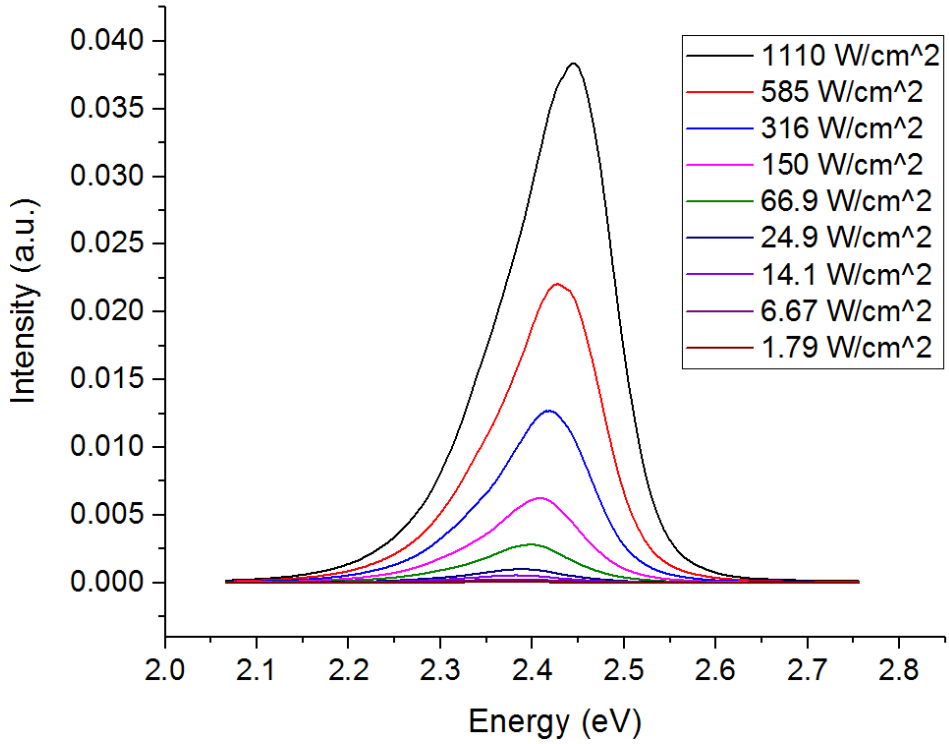

(a)

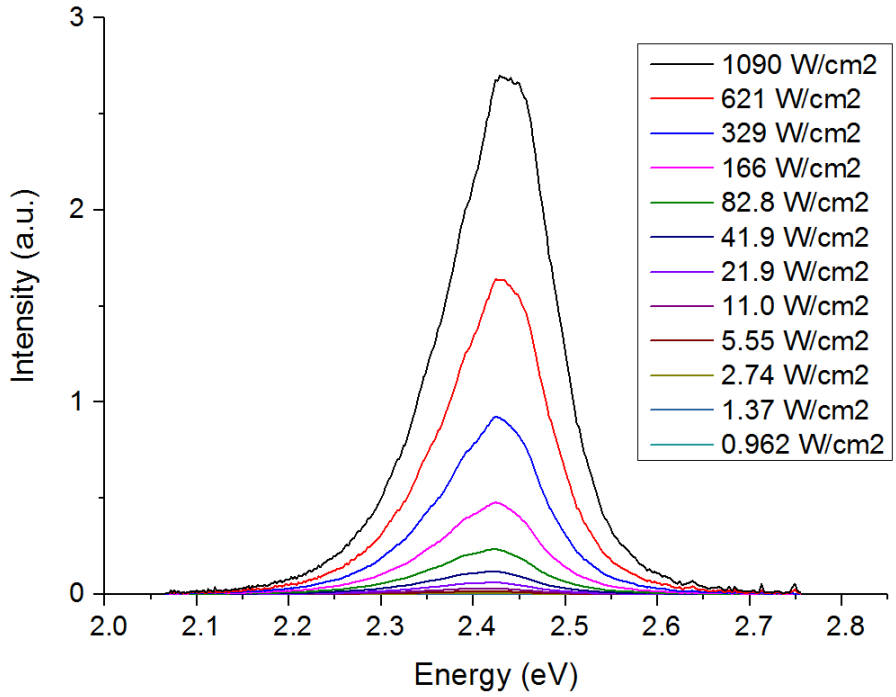

(b)

Figure 4.12: Power dependent spectra of (a) the C3861 5 QW sample and (b) the C3862 10 QW sample measured at 10 K.

The peak emission energy of the spectra of all the samples also blue-shifts with increasing excitation power density as the QCSE in the QWs is screened by the increasing carrier density. Some Fabry-Pérot oscillations are present in the spectra of all the samples despite the use of the Brewster angle geometry in the PL collection; these oscillations may have obscured the phonon replica emission peak in the 1 QW spectra. The phonon replica emission peaks are likely to be not resolved in the MQW samples due to the superposition of the PL emission from the many QWs.

The power densities were selected to allow a comparison of the samples at the same power density per QW since the injected carriers will be divided between the QWs such that a sample with more QWs will have a lower carrier density per QW compared to a sample with fewer QWs when excited at the same excitation power density; this allows data points to be plotted against power density per QW in Figure 4.13. To allow a comparison between the samples to be made, it was assumed that the carriers are spread equally between the QWs in the MQW samples and that the carriers excited by the laser in the GaN barriers are able to access the deepest QWs in the 10 QW sample despite the intensity of the beam dropping by around 63 % at a penetration depth of 85 nm into the sample[132]. In Figure 4.13, the normalized integrated intensity of the spectra divided by the excitation power density is plotted against the excitation power density per QW to determine the excitation power densities per QW for which the plateau region occurs for the samples. It is assumed that at the plateau region the recombination mechanism of the carriers in the QWs is purely radiative; at a temperature of 10 K and at sufficiently low carrier densities, the carriers cannot delocalize and access non-radiative recombination centres.

The droop curves of the samples are similar in Figure 4.13, displaying a plateau region where the integrated intensity is linear with respect to excitation power per QW below 10 W cm^{-2} and a droop region where the integrated intensity is sub-linear with respect to power density per QW above 10 W cm^{-2}. This establishes that, for an excitation power density per QW below 10 W cm^{-2}, efficiency droop is not significant for any of the samples.

The 1 QW sample droops at a marginally lower power density per QW compared to the other multiple quantum well samples which is consistent with the longer carrier lifetime observed in this sample, see Figure 4.5, resulting in a higher carrier density per QW for the same excitation power density per QW compared to a sample with a shorter carrier lifetime. The occurrence of droop at similar power densities per QW for all the samples indicates that all the samples have similar rates of carrier capture within the limitations of the experiment, assuming that droop occurs at the same carrier density per QW for all the samples along with the previous assumptions; it was not possible to directly determine if the carriers are equally captured into each well of the MQW samples through this experiment. The droop behaviour of the 10 QW sample is consistent with that of the 3 and 5 QW samples, suggesting that the assumption of carriers reaching the deepest QWs in the 10 QW sample is valid.

4.3.4 300 K Power Dependent IQE Measurements

The IQEs of the samples at 300 K were also determined as function of power density per QW, see Figure 4.18, by performing additional power dependent PL at 10 K and 300 K, see Figures 4.14, 4.15, 4.16 and 4.17; this data was then combined with previous data from Figure 4.11a to produce Figure 4.18. The range of excitation power densities was selected to be below the excitation for when droop commences.

In the spectra, some of which suffer from Fabry-Pérot oscillations, it can be seen that the intensity of the QW emission increases with increasing excitation power density. The peak emission energy of the spectra of all the samples at 300 K and 10 K blueshifts with increasing excitation power density as the QCSE in the QWs is screened. The spectra of the samples at 300 K has a larger FWHM compared to their respective spectra at 10 K, as observed in Section 4.3.2. The IQEs of the samples at 300 K were determined by dividing the integrated intensities of the 300 K spectra by the integrated intensities of their respective 10 K spectra; as discussed previously, this assumes that the IQE is 100 % at 10 K at the power excitation densities used.

In Figure 4.18, the IQE of all the samples increases with increasing

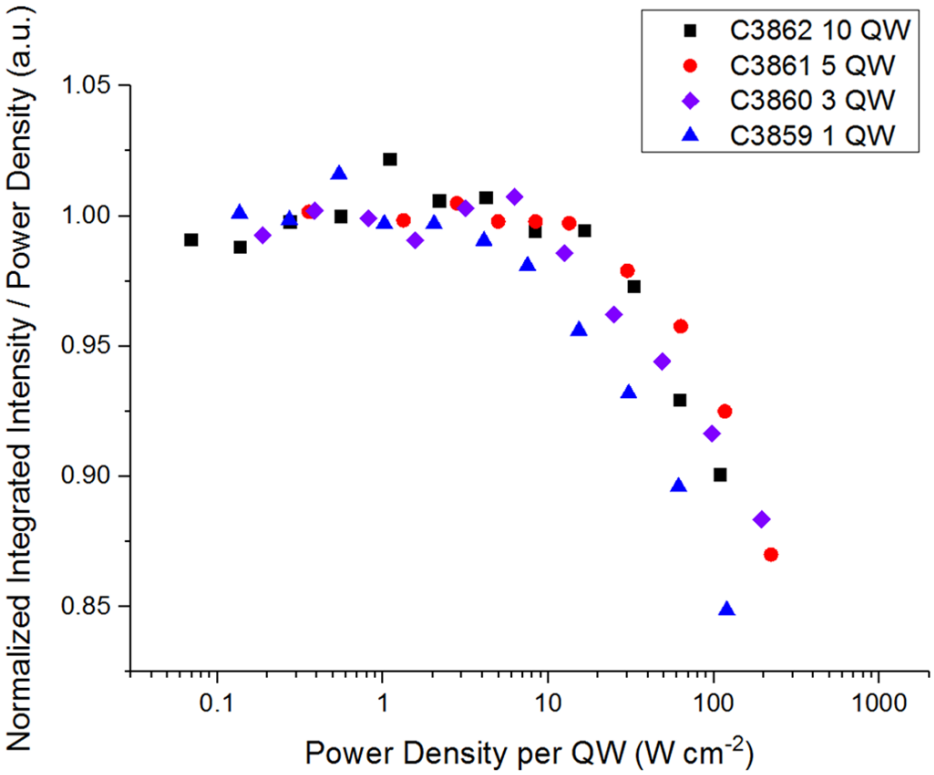

Figure 4.13: The normalized integrated intensities of the spectra from power dependent PL performed at 10 K on C3859 - C3862 are divided by the excitation power density and plotted against the excitation power density per QW to give an efficiency droop curve.

power density per QW and the samples with a greater number of QWs predominately have higher IQEs compared to the samples with less QWs except in the case of the 3 QW sample at excitation power densities below 2 W cm^{-2} per QW. The rate of increase of IQE for the 1, 5 and 10 QW samples appears to be linear over the given range of power density per QW; the rate of increase is similar for the 5 QW and 10 QW samples but is at a relatively reduced rate for the 1 QW sample. The IQE of the 3 QW sample increases gradually with increasing power density at low power densities and has an apparent change of gradient at the higher power densities.

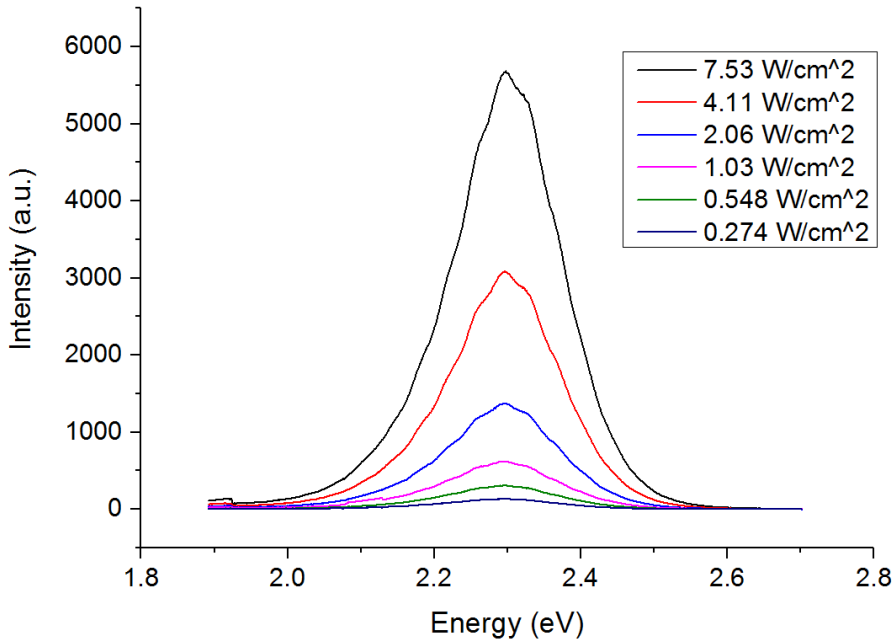

(a)

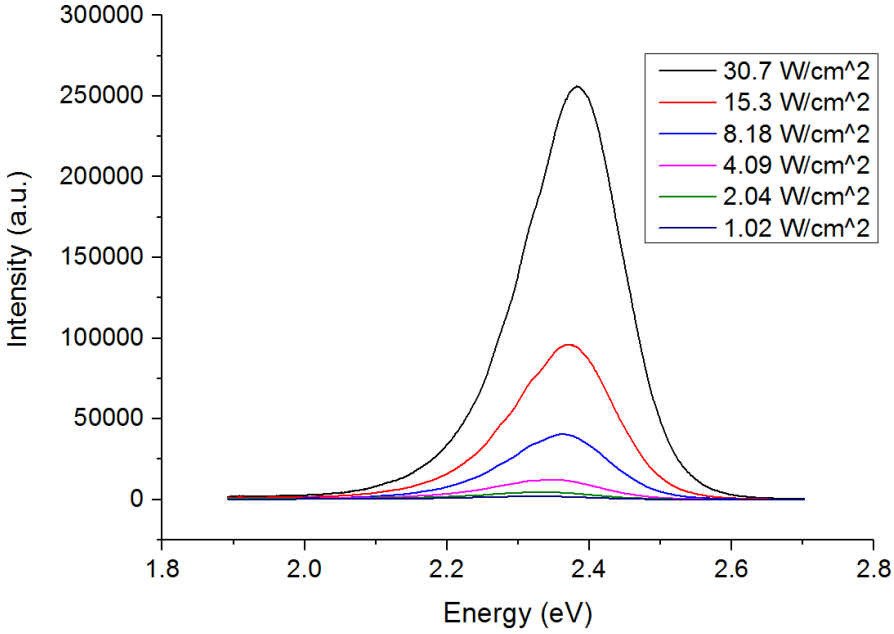

(b)

Figure 4.14: Power dependent spectra of (a) the C3859 1 QW sample and (b) the C3860 3 QW sample measured at 300 K.

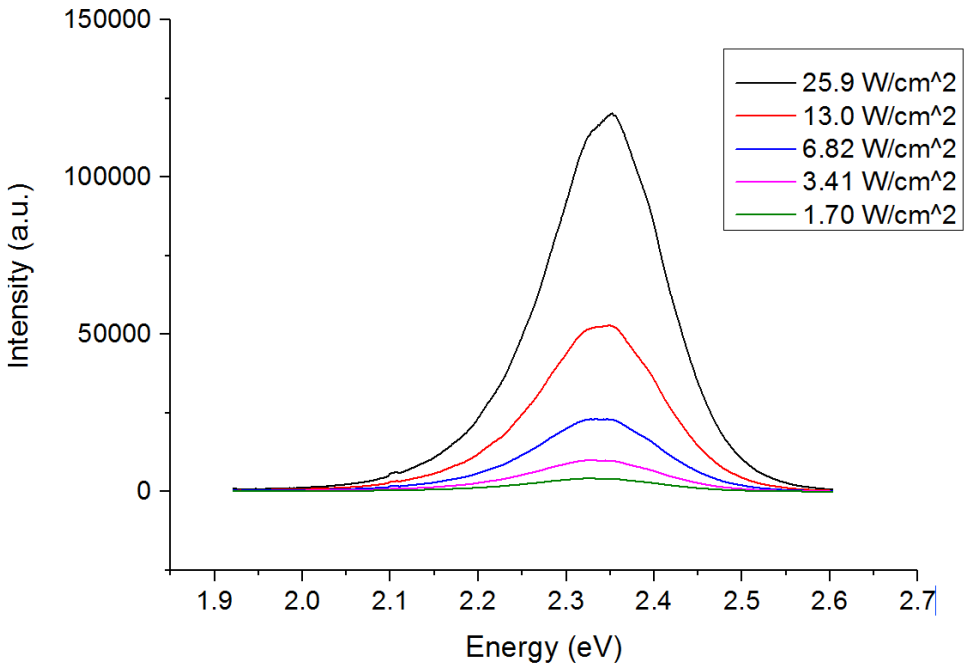

(a)

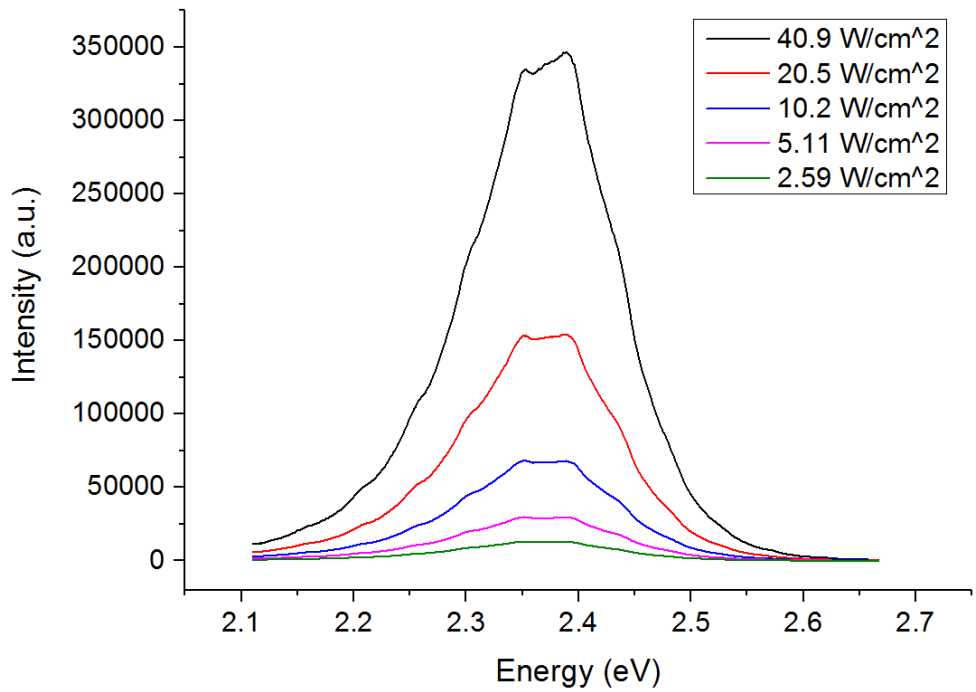

(b)

Figure 4.15: Power dependent spectra of (a) the C3861 5 QW sample and (b) the C3862 10 QW sample measured at 300 K.

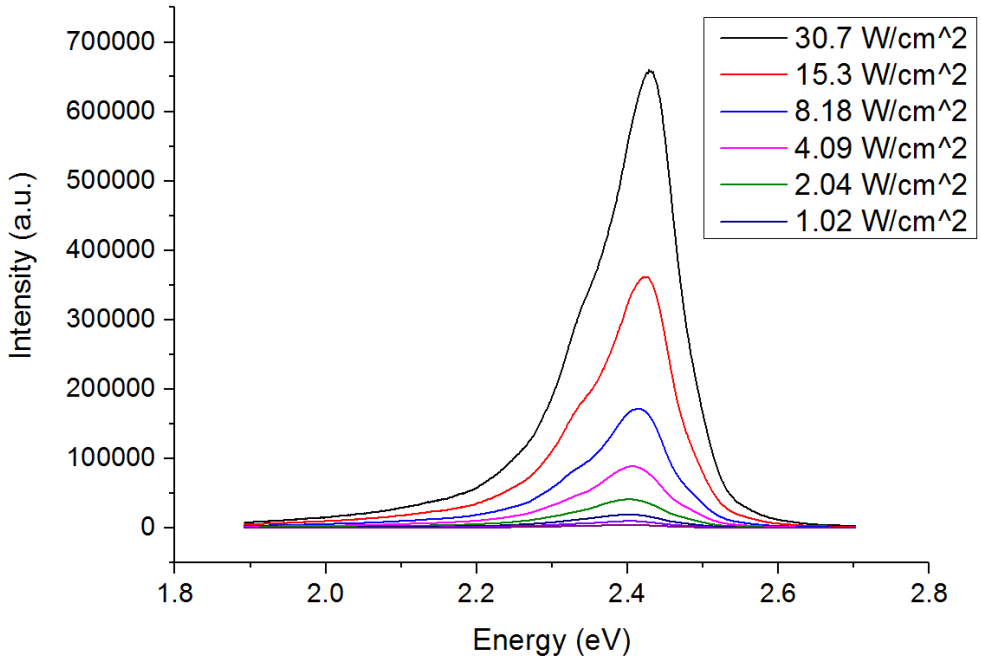

(a)

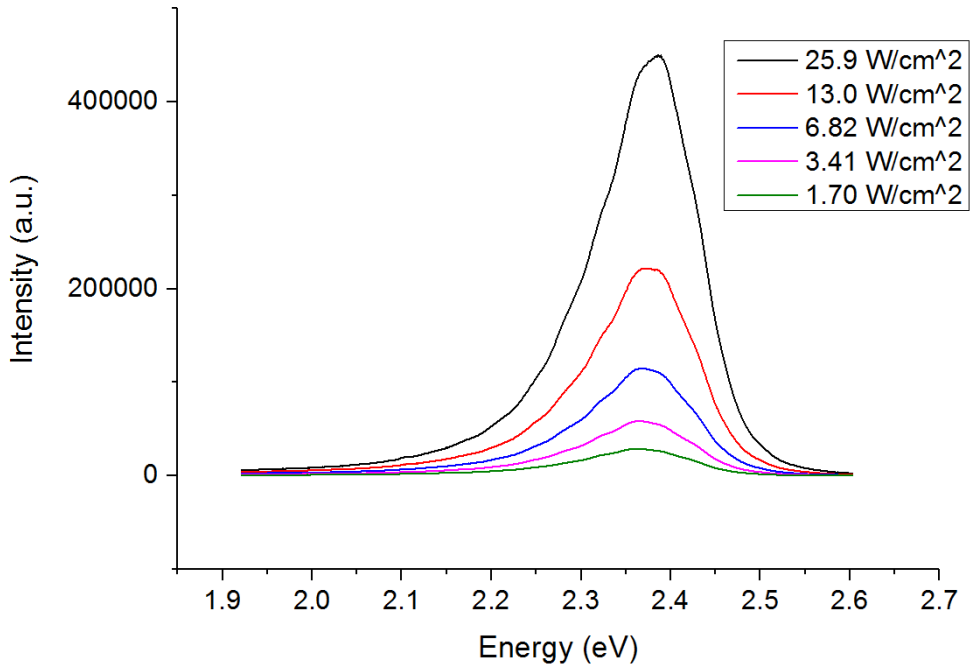

(b)

Figure 4.16: Power dependent spectra of (a) the C3860 3 QW sample and (b) the C3861 5 QW sample measured at 10 K.

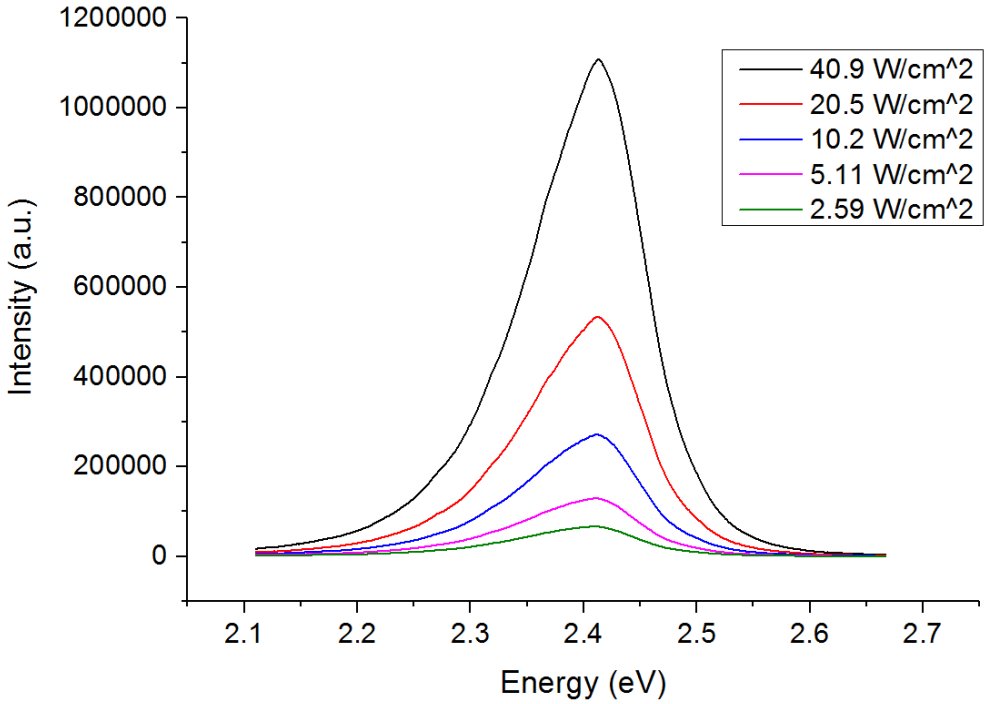

Figure 4.17: Power dependent spectra of the C3862 10 QW sample measured at 10 K.

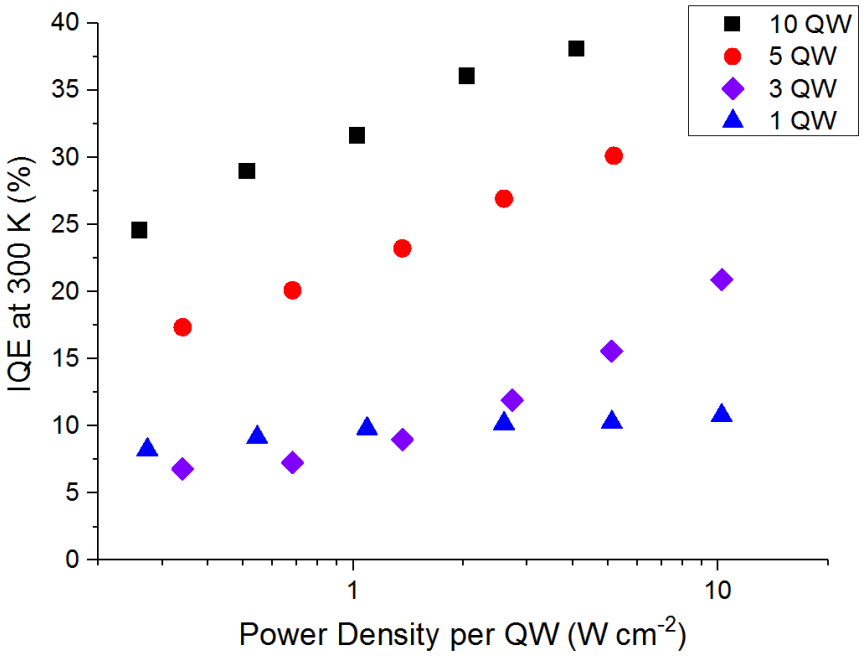

Figure 4.18: The internal quantum efficiency of the QW samples C3859 - C3862 as function of excitation power density per QW at 300 K.

The increase in IQE with increasing power density of the samples could be due to the saturation of defect-related non-radiative recombination centers. Assuming that the injected carriers spread out equally between the QWs in the MQW samples, the greater 300 K IQE for samples with more QWs in Figure 4.18 shows that the samples with more QWs are less susceptible to a thermally activated non-radiative carrier loss mechanism. There is a discrepancy of a few percentage points between the data in Figure 4.18 and the data in Figure 4.10; this may be because the PL spectra for the data points in Figure 4.10 were obtained using setup A and the PL spectra for the data points in Figure 4.18 were obtained using setup B on separate occasions, such that the laser excitation spot on a particular sample in the two sets of experiments may not have been at precisely the same position on the sample.

The PL spectra shown in Figure 4.4) and PL time decay measurements shown in Figure 4.5) of the samples suggests that the indium content, strain and average well thickness is the most similar for the 3 QW and 5 QW samples. The 1 QW and 10 QW samples may have a greater and lesser indium fraction, respectively. A reduced level of indium in the MQW samples may have led to reduced strain and defect formation throughout the InGaN QW layers in the MQW samples[4]. Studies have found that samples with lower threading dislocations densities have a higher integrated PL intensity at 300 K compared to samples with larger threading dislocations densities[138, 136, 137, 109]. Additionally, the variation in average QW thickness between the different QW growth layers could have lead to a reduction in the average QW thickness in the samples with more QWs, see Figure 4.3, therefore reducing the average QCSE in the samples with more QWs. Moreover, the 10 QW sample may have undergone strain relaxation, leading to a shorter lifetime and a blueshifted emission peak from a reduced strain-induced QCSE; this effect was observed in a study carrier on InGaN pre-layers by Nanhui *et al.* [135] and in a study on InGaN MQWs by Wang *et al.* [63]. All of these pathways could contribute to the increased IQE at 300 K for the samples with more QWs observed in Figure 4.18.

Nevertheless, comparing the IQE measurements in Figure 4.18 for the 3 QW and 5 QW samples which have very similar peak emission energies

and lifetimes indicates that there is a reduction in thermally activated non-radiative recombination for samples with a higher number of QWs that are otherwise similar. This suggests that increasing the number of QWs leads to increased recapture of thermionically emitted carriers in green light-emitting QWs as well as blue light-emitting InGaN QWs, as previously reported[140, 132].

4.4 Summary

A series of green light-emitting InGaN/GaN QW samples with 1, 3, 5 and 10 QWs, each with a nominal 25 % indium fraction, were investigated with respect to the effect of QW number on the IQE of the samples using TIPL spectroscopy and 10 K PL time decay measurements. The PL time decay and PL measurements suggests that there was a different level of indium incorporation amongst the QW samples, that the average thickness of the QWs decreased with QW number or that strain relaxation occurred for the 10 QW sample or that a combination of the three occurred. However, the 3 and 5 QW samples were measured to have similar peak emission energies and lifetimes, indicating that the two samples have a similar indium fraction, average well width thickness and levels of strain.

It was determined from 10 K power dependent PL spectroscopy that, within the limitations of the experiment, the onset of efficiency droop for all the samples occurs at the same power density per quantum well at 10 K; assuming that droop occurs at the same carrier density per quantum well in all the samples, this suggests that the samples were equally efficient at capturing carriers.

Further measurements of the PL spectra of the samples at 10 K and 300 K were performed at below droop power densities; it was found that the samples with more QWs had a higher IQEs for the majority of power densities measured, suggesting that the samples with more QWs were less susceptible to a thermally activated carrier loss mechanism. This thermally activated carrier loss mechanism could potentially be SRH recombination, thermionic emission or a combination the two mechanisms.

The increase in IQE may be due to a smaller defect density in the samples with more QWs leading to reduced rates of non-radiative recombination, as the samples with more QWs may have a lower indium fraction. In addition, the possible relaxation of strain in the top InGaN QW layers of the 10 QW sample and the possible reduction in QW thickness with increasing QW number may have also contributed to an increased rate of radiative recombination, due to a reduction in the QCSE in the samples with more QWs, causing them to be less susceptible to thermally activated carrier loss mechanisms. However, by comparing the 3 and 5 QW samples alone, the IQE data also indicates that thermionic emission plays a role in increasing the IQE of the samples with more QWs; the samples with more QWs have a higher probability of recapturing carriers that have been thermally excited out of the wells.

Chapter 5

Excitation Density Dependent Behaviour of InGaN MQWs with Varying Defect Density

5.1 Introduction

This chapter discusses investigations carried out on a set of InGaN/GaN MQW samples with different defect densities using a range of excitation densities. The purpose of the study was to investigate the effect of defect density on the high energy band. The set of samples investigated have previously been studied by Hammersley *et al.* who performed PL time decay measurements on the samples at 10 K and 300 K and measured the IQE of the samples at 300 K; they observed that the samples with the higher growth temperatures had greater IQEs and significantly longer lifetimes at 300 K despite all the samples having similar lifetimes at 10 K[141]. Hammersley *et al.* attributed the reduced susceptibility of the higher growth temperature samples to non-radiative recombination to a lower density of point defects being incorporated into the higher growth temperature samples during growth[141]. This is supported by the demonstration that InGaN/GaN QWs grown at lower growth temperatures can have increased incorporation of structural defects[10] and that point defects act as non-radiative recombination centers[146, 147].

The presence of a greater point defect density in the lower growth

temperature InGaN/GaN QW samples may affect the high energy band. The high energy band typically occurs at the high carrier density for which efficiency droop is observed[9]. Modelling indicates that this band forms when the carrier density is sufficiently high enough for the lower energy states to be saturated and the higher energy, less well localized, states to become occupied[9, 92, 98]. Similarly, efficiency droop may be due to the delocalization of carriers, granting carriers access to defects which act non-radiative recombination centers[7], see Section 2.2.1. Previous studies have related the high energy band to the recombination of delocalized carriers[8, 100, 9, 99]. However the high energy band also been attributed to the recombination of carriers from the $n = 2$ subband[101], a confined hole continuum[102] and an electron-hole plasma[104].

Davies *et al.* and Sun *et al.* performed time-resolved photoluminescence spectroscopy (TRPL) and time-resolved pump-probe differential PL respectively on InGaN QWs at high carrier densities. Davies *et al.* and Sun *et al.* showed that the PL spectra of InGaN QWs exhibited a broadening on the high energy side at high carrier densities and the onset of this feature coincided with the emergence of an initial, quickly decaying, mono-exponential component which was superimposed on the slower, non-mono-exponential decay typically seen at lower carrier densities; the authors attributed the high energy feature and mono-exponential decay to PL emission resulting from carriers recombining from weakly localized states[8, 100]. The high energy broadening was also observed by Bochkareva *et al.* in an InGaN/GaN QW LED[99], who also attributed the broadening to recombination from shallow, weakly localized states.

TRPL of InGaN QWs by Christian *et al.* showed that the high energy broadening extends to higher energies to become a high energy band at even higher carrier densities; the authors also observed plateaus in the PL time decay measurements where luminescence was constant with time[9]. Christian *et al.* attributed the high energy band to the recombination of carriers from excited, semi-localized states and the PL time decay plateaus to the refilling of states by carriers from higher energy states; they generated a theoretical model to demonstrate the change in carrier wavefunction overlap of states with increasing state energy[9].

Shahmonhammadi *et al.* performed spectrally and temporally re-

solved PL of a single InGaN/GaN QW at high carrier densities using a charge-coupled device and a streak camera and power dependent TRPL; they observed a rapidly decaying high energy broadening and attributed the feature to the recombination of carriers in an electron-hole plasma, which have undergone a Mott transition from excitons to a conductive electron-hole plasma due to an increasing carrier population, and the fast decay to Auger recombination[104].

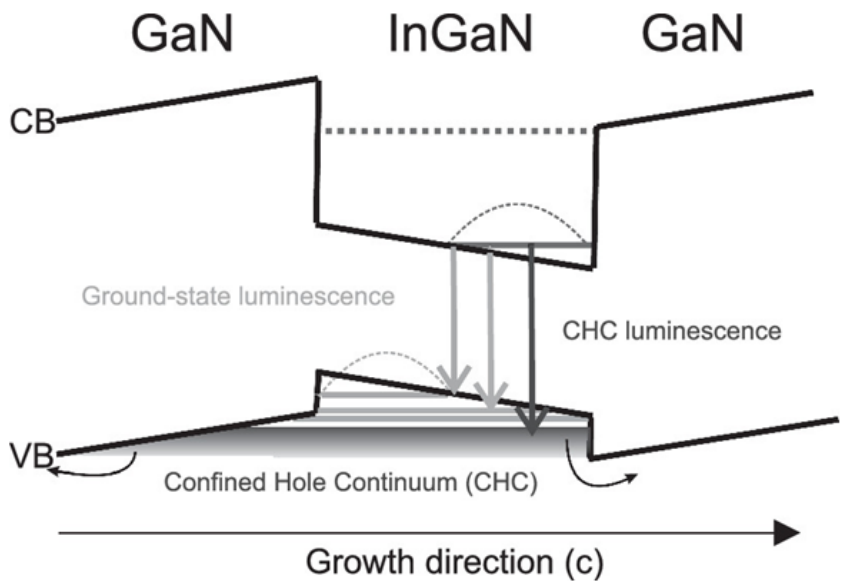

Figure 5.1: Schematic depicting the recombination of ground state electrons with holes in the confined hole continuum as proposed by Nippert *et al.*, reproduced with permission from Reference [102].

The high energy band was also observed in InGaN QWs by Nippert *et al.* using TRPL. They attributed the feature to the radiative recombination of localized, ground state electrons with excited holes in the confined hole continuum, which consists of holes that are weakly confined by the tilted valence band edge shown Figure 5.1[102]. The origin of the HEB emission from InGaN QWs is thus not widely agreed upon; the investigations described in this chapter were carried out primarily to determine if there is a relationship between the properties of the HEB and defect density.

5.2 Sample Details

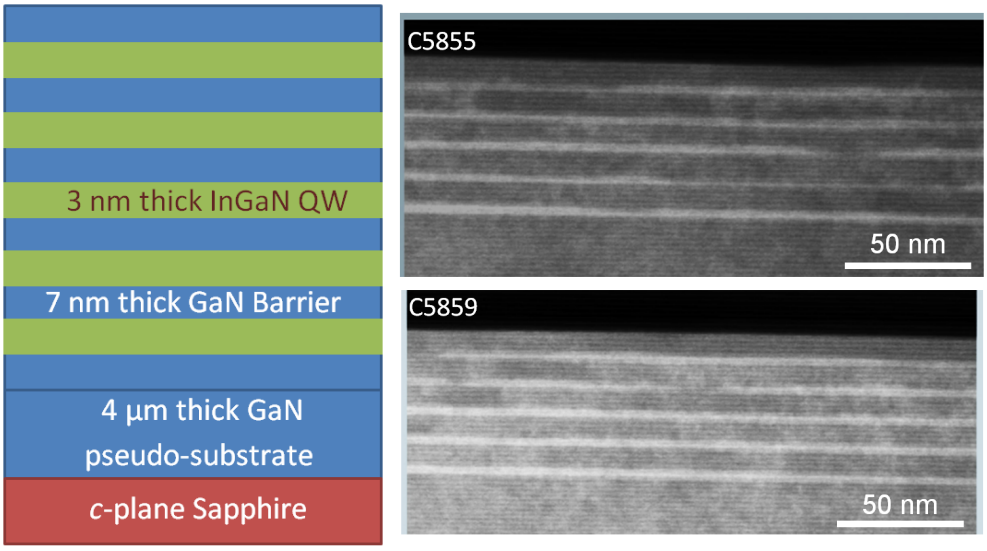

(a) (b)

Figure 5.2: (a) Schematic diagram depicting the structure of the QW samples C5855, C5857 and C5859. (b) STEM-HAADF images of the samples C5855 and C5859.

The three InGaN/GaN QW samples investigated were grown in a Thomas Swan 6 × 2 inch Close Coupled Showerhead MOCVD reactor on a 4 μm GaN pseudo-substrate with a defect density of around 4 × 10^8 cm^{-2} on (0001) sapphire using the 2-T growth method described in Section 2.1.1; the QW samples each consist of 5 green light-emitting QWs with a nominal 3 nm QW thickness and a nominal 7 nm GaN barrier thickness[141], see Figure 5.2. The scanning transmission electron microscope - high-angle annular dark-field (STEM-HAADF) images of C5855 and C5859 were provided by Kappers *et al.* from the University of Cambridge[103]. The samples C5855, C5857 and C5859 were measured to have a period of 9.9 ± 0.2 nm, 9.9 ± 0.2 nm and 10.0 ± 0.2 nm respectively by x-ray diffraction[141]. The QWs of the samples were grown at different temperatures with a varying trimethylindium (TMI) flow rate to obtain a similar level of indium incorporation and peak emission energies amongst the samples, see Table 5.1; the emission peak of the samples at 10 K is around 2.30 eV.

Table 5.1: Sample details of the InGaN/GaN QW series with varying growth temperature as determined from XRD[141].

Sample	**QW Growth Temperature (°C)**	**TMI flow (μmol/min)**	**Average In Content of QW & Barrier (%)**
C5855	716	9.7	5.1 ± 0.5
C5857	706	4.8	5.2 ± 0.5
C5859	698	3.5	5.1 ± 0.5

The samples were also investigated by Ding *et al.* who performed atomic force microscopy on the samples to determine their dislocation density; they estimated that samples C5855, C5857 and C5859 have a dislocation density of 9.1 $\times$ 10^8 cm^{-2}, 9.4 $\times$ 10^8 cm^{-2} and 10.8 $\times$ 10^8 cm^{-2} respectively and dislocation cluster densities of 4.2 $\times$ 10^8 cm^{-2}, 4.6 $\times$ 10^8 cm^{-2} and 5.0 $\times$ 10^8 cm^{-2} respectively[148]. Ding *et al.* and Hammersley *et al.* both reported the presence of gross well width fluctuations in the samples from x-ray reflectivity and x-ray diffraction measurements performed on the samples respectively[141, 148]; these can also be seen in Figure 5.2b.

5.3 Results and Discussion

The samples C5855, C5857 and C5859 were investigated using power dependent PL, time-resolved PL and PL time decay measurements at 10 K to observe the emergence of the HEB as the excitation density is increased and to characterize its behaviour.

5.3.1 10 K Power Dependent PL Spectra

Power dependent time-integrated PL was performed on the samples at 10 K using setup C described in Section 3.2 to study the samples, see Figures 5.3 and 5.4. At the lowest excitation power density used for each sample, around 1.71 μJ cm^{-2} pulse^{-1}, the peak emission energies of the samples were 2.320 eV, 2.345 eV and 2.297 eV for samples C5855, C5857 and C5859 respectively. In all three samples, a high energy broadening

appears at high excitation power densities; the intensity of the broadening relative to the typical emission peak is the greatest for C5855 and there is no trend for the broadening with growth temperature, see Figure 5.5. There is a blueshift of the peak emission energy with increasing excitation power; this may be partly due to the increased prominence of the HEB with increasing excitation.

The intensity of the high energy broadening relative to the main emission peak may be higher for C5855 possibly because the sample contains marginally more indium than the other two samples, see Table 5.1. In the study of the HEB by Christian *et al.*, they observed that QW samples with a higher indium fraction have a more pronounced HEB compared to QW samples with a lower indium fraction when excited at the same carrier density[9]. Comparing the spectra in Figures 5.3 and 5.4 suggests that the growth temperature of the samples, and thus their difference in defect density, does not have a significant impact on the magnitude or width of the HEB.

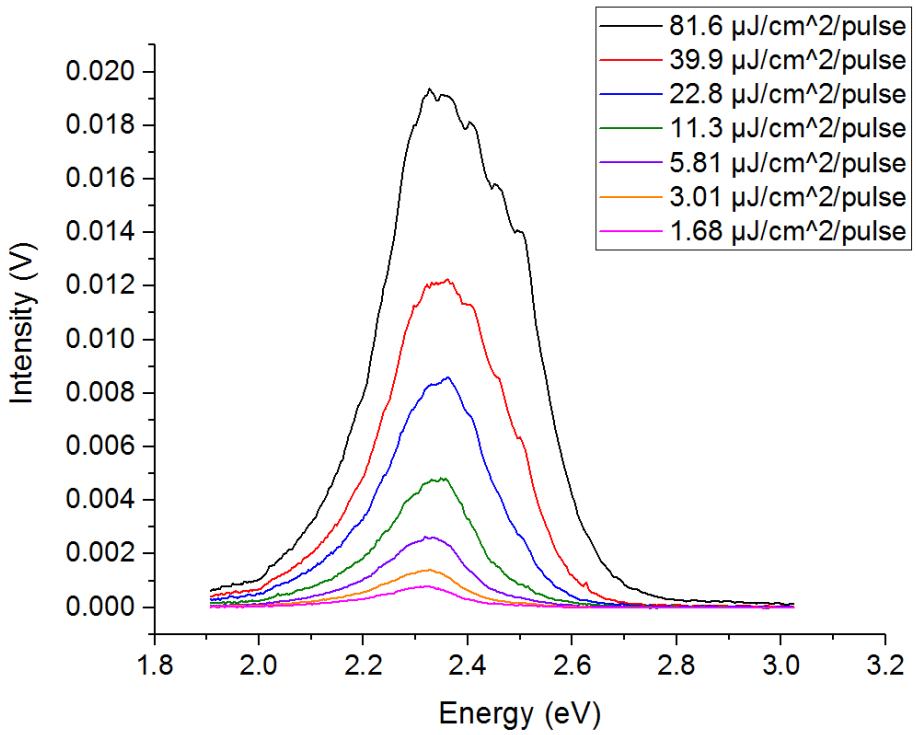

Figure 5.3: Spectra of the power dependent PL measurements performed on sample C5855 at 10 K using setup C.

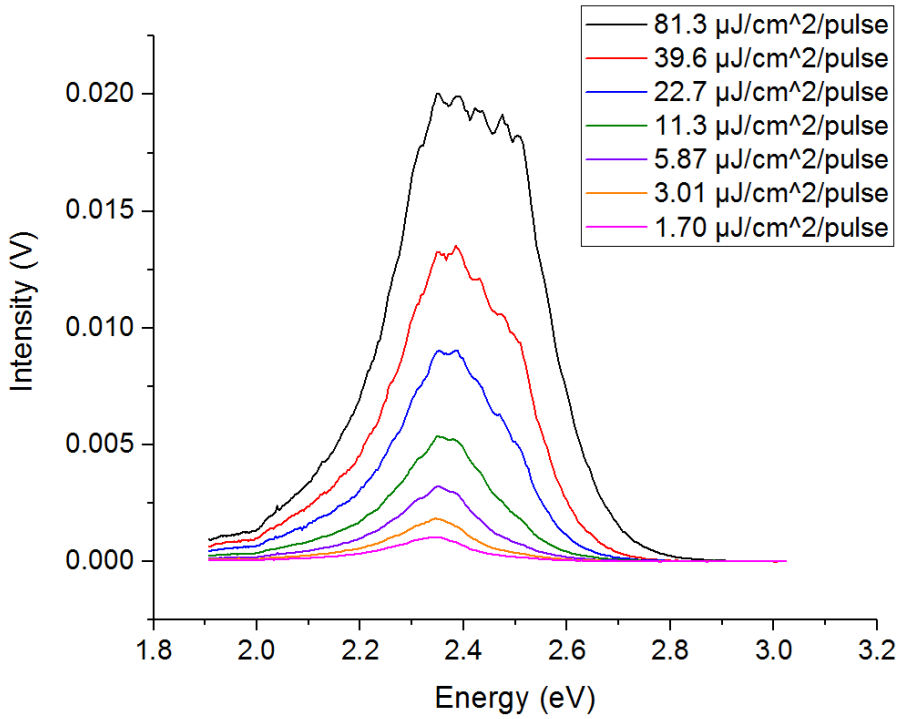

(a)

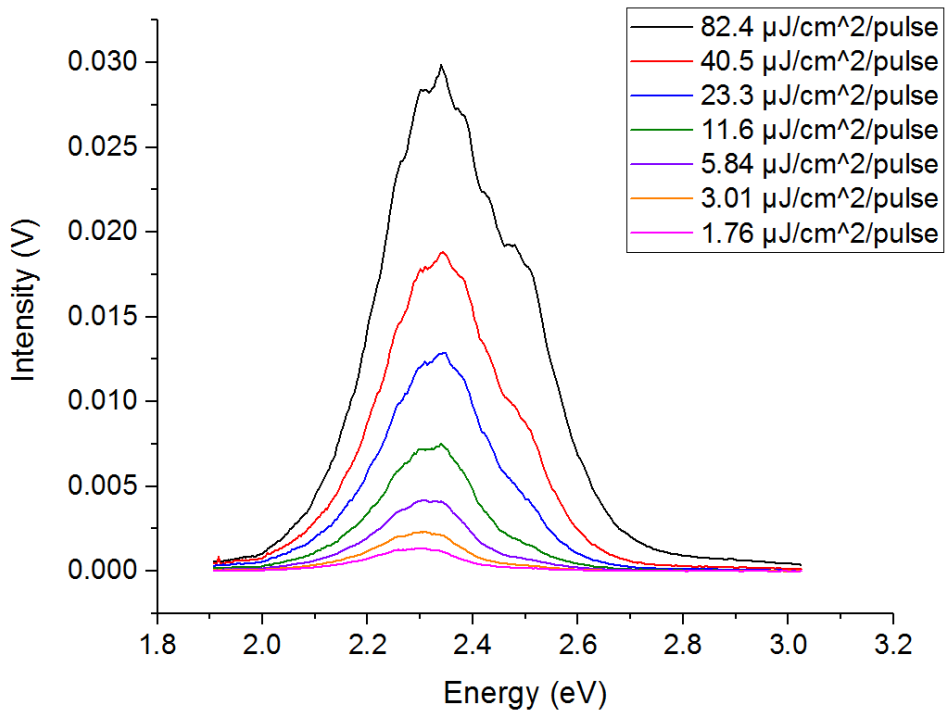

(b)

Figure 5.4: Spectra of the power dependent PL measurements performed on sample (a) C5857 and (b) C5859 at 10 K using setup C.

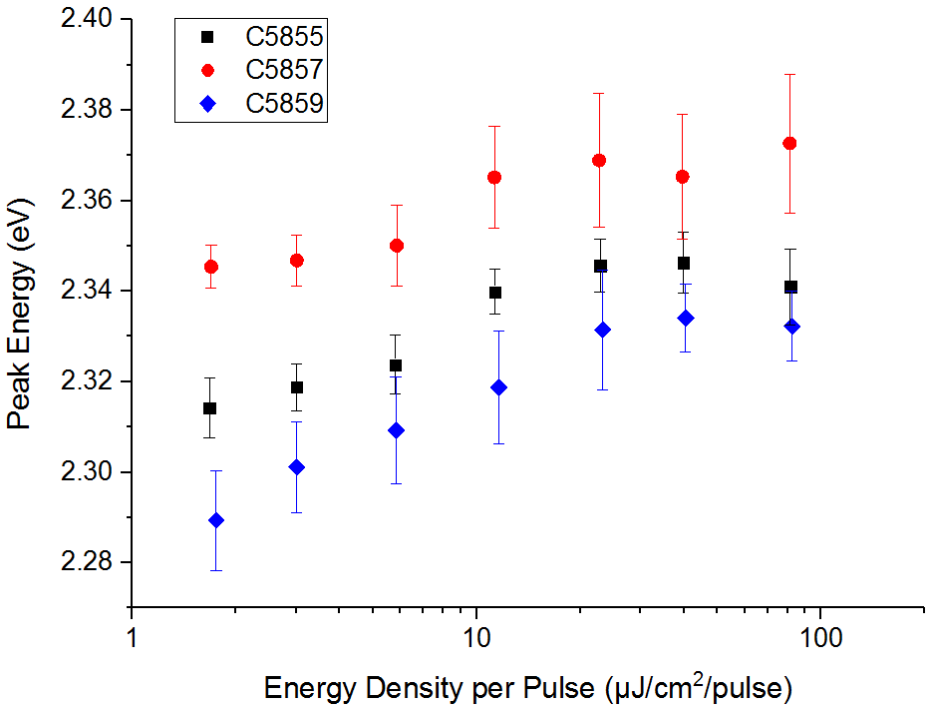

(a)

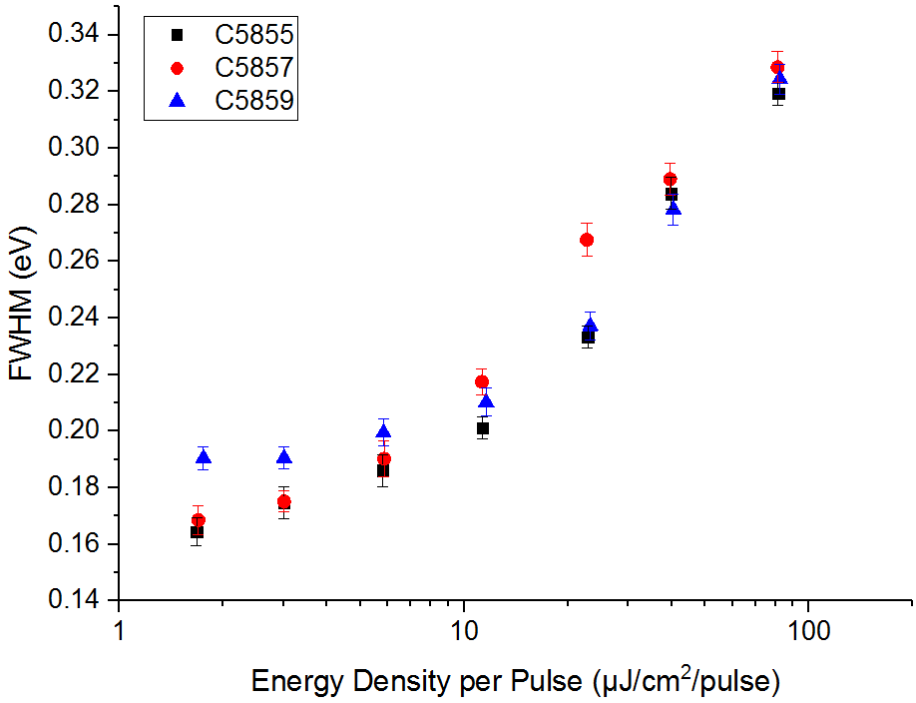

(b)

Figure 5.5: The (a) peak energy and (b) full-width half-maximum of the 10 K power dependent PL spectra of samples C5855, C5857 and C5859.

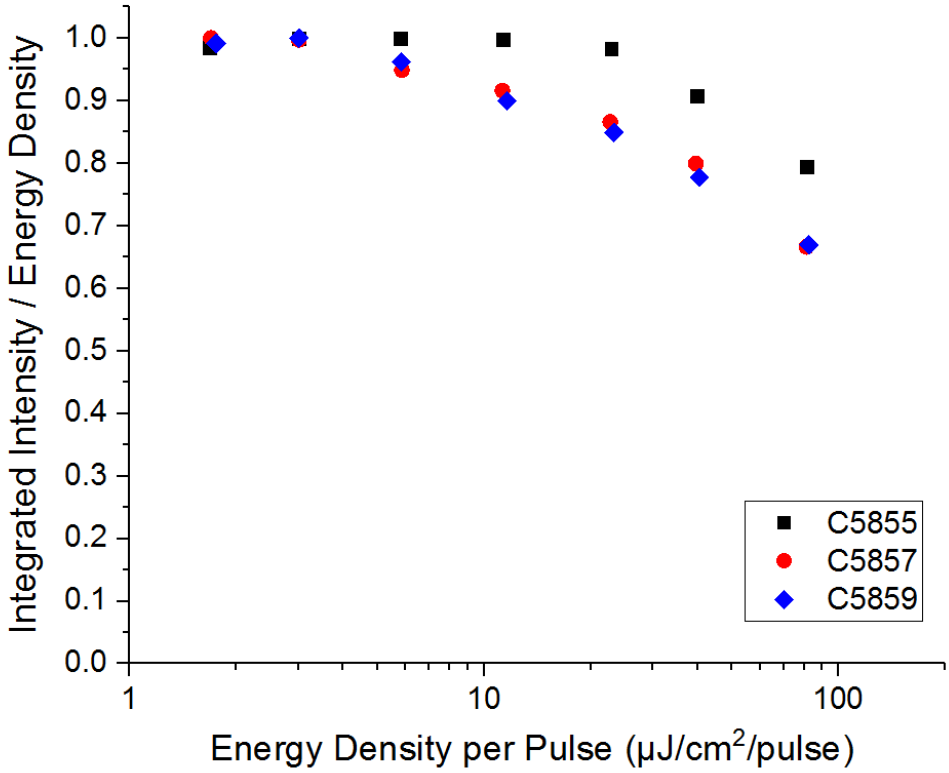

Figure 5.6: The integrated intensity of the spectra in Figure 5.3 and 5.4 divided by their excitation energy density, showing the efficiency droop of the samples C5855, C5857 and C5859.

The integrated intensity of the spectra in Figure 5.3 and 5.4 were divided by their excitation energy density and plotted against the excitation energy density in Figure 5.6. In Figure 5.6, the sample with the highest growth temperature C5855 exhibits the onset of efficiency droop at a higher excitation energy density compared to the other two samples, which exhibit very similar droop behaviour with excitation energy density; this suggests that the sample with a highest growth temperature, and hence the lowest defect density, was least susceptible to the non-radiative recombination mechanism which is responsible efficiency droop. The samples C5857 and C5859 may have very similar droop curves despite their different growth temperatures possibly because of a slightly higher indium fraction in the C5857 sample.

The variation in droop behaviour with growth temperature, and hence defect density, is consistent with the density-activated defect recombina-

tion model of efficiency droop put forward by Hader *et al.* as a reduced density of non-radiative recombination centers, i.e. defects, will require a larger population of carriers to access those defects[7]. The defects responsible may be point defects or threading dislocations as both are varied in the samples studied. However, previous studies have not found a correlation between dislocation density and efficiency droop. A study by Davies *et al.* which investigated the efficiency droop behaviour of samples with varying dislocation densities from the order of 10^7 cm^{-2} to 10^9 cm^{-2} using PL which found that there was no systematic behaviour of the samples in terms of efficiency droop[149]. Similarly, Schubert *et al.* performed electro-luminescence on two InGaN QW LEDs with varying threading dislocations and concluded that dislocations do not significantly impact efficiency droop[137].

5.3.2 10 K Time-Resolved PL Spectra

Time-resolved PL was also performed on the samples at 10 K using setup C with an excitation energy density of 89.2 μJ cm^{-2} pulse^{-1} by recording the photon counts as a function of time for varying wavelengths, see Figures 5.8 and 5.7. The time-varying PL spectra were averaged over several time windows for each sample. In the 0 ns - 0.5 ns time window, the high energy band peak emission is at around 2.58 eV for all three samples. As time increases, the emission spectra rapidly collapses in intensity and decreases in width; the peak redshifts towards the spectral region corresponding to the emission spectra seen in the TIPL of the samples. The 10 K TRPL measurements show that all the samples in the series have very similar high energy band emission behaviour at short timescales. If the high energy band arises due to carriers recombining from weakly localized states as proposed in the literature[8, 100, 99, 9], it appears that the samples have similar weakly localized states.

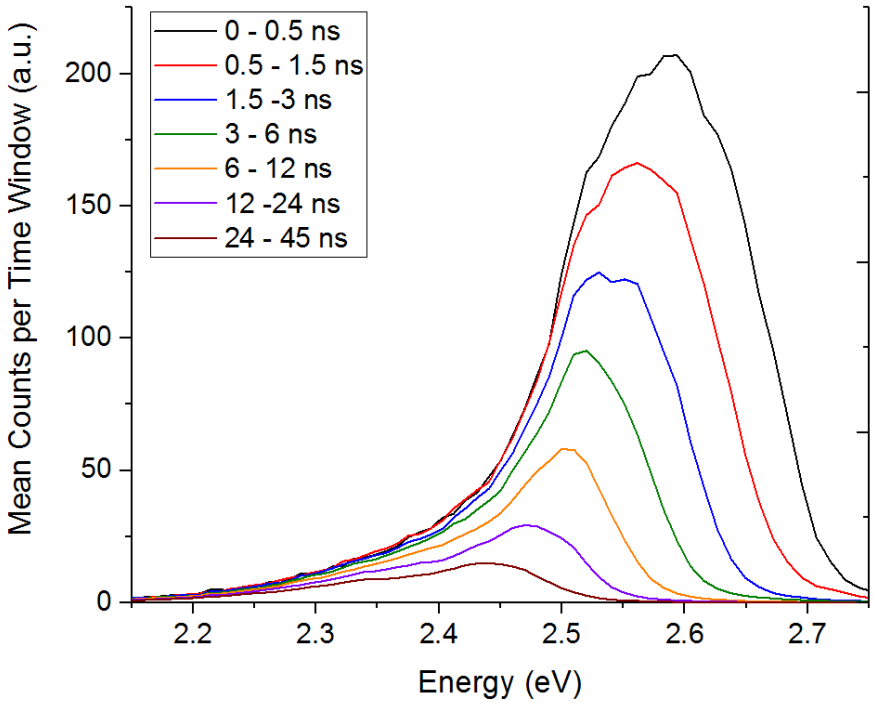

(a)

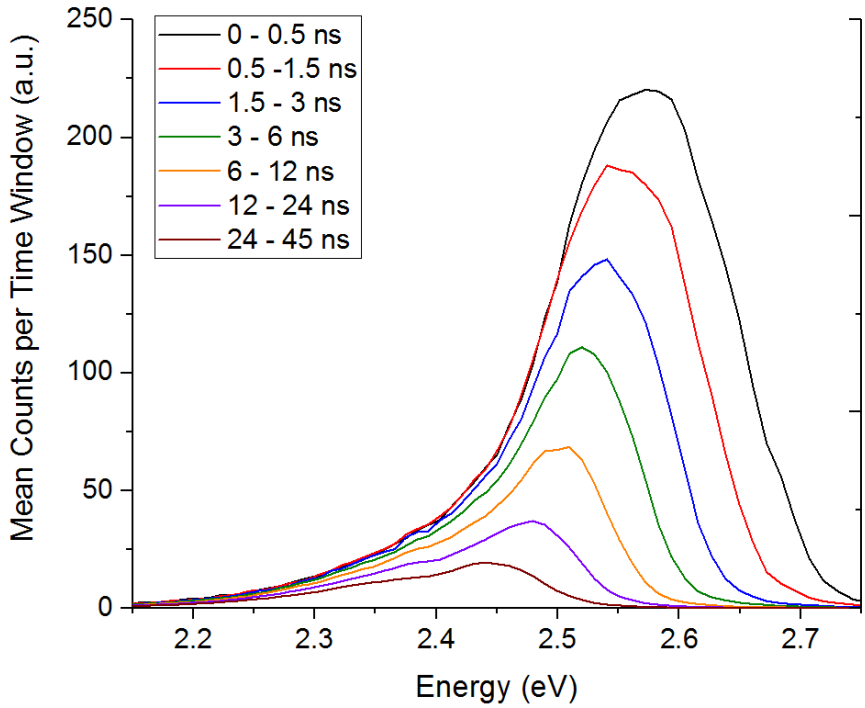

(b)

Figure 5.7: Spectra from the time-resolved PL of (a) C5855 and (b) C5857 at 10 K with an excitation energy density of 89.2 μJ cm^{-2} pulse^{-1}.

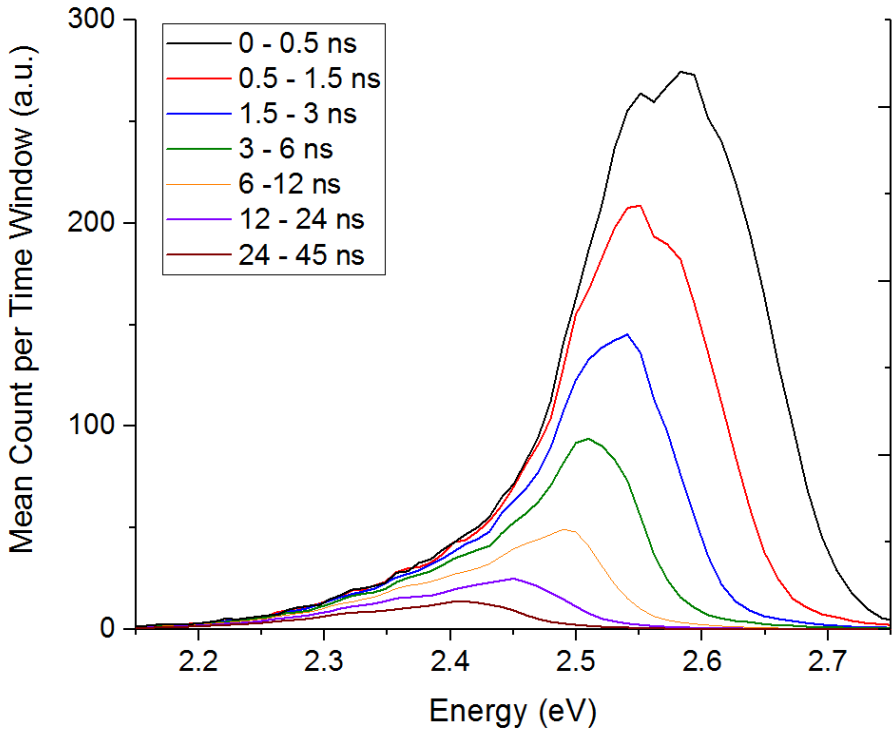

Figure 5.8: Spectra from the time-resolved PL of C5859 at 10 K with an excitation energy density of 89.2 μJ cm^{-2} pulse^{-1}.

5.3.3 10 K Power Dependent PL Decay Measurements at 2.301 eV

Power dependent PL decay measurements were performed on the samples at an emission energy of 2.301 eV, corresponding to the peak emission energy of the samples under low excitation, at 10 K using setup C, see Figures 5.9, 5.10 and 5.11. The decays shown are non-monoexponential and the rate of decay of the excited carrier population in the samples increases with excitation power. However, when the detected counts are plotted on a reduced timescale, where the time t is divided by the time for the carriers to drop to a tenth of its initial population $T_{0.1}$, the decay curves for each sample at different excitation powers appear to have a very similar shape, see Figures 5.9, 5.10 and 5.11. This shape similarity is consistent with PL emission from carriers occupying a distribution of localized states[69].

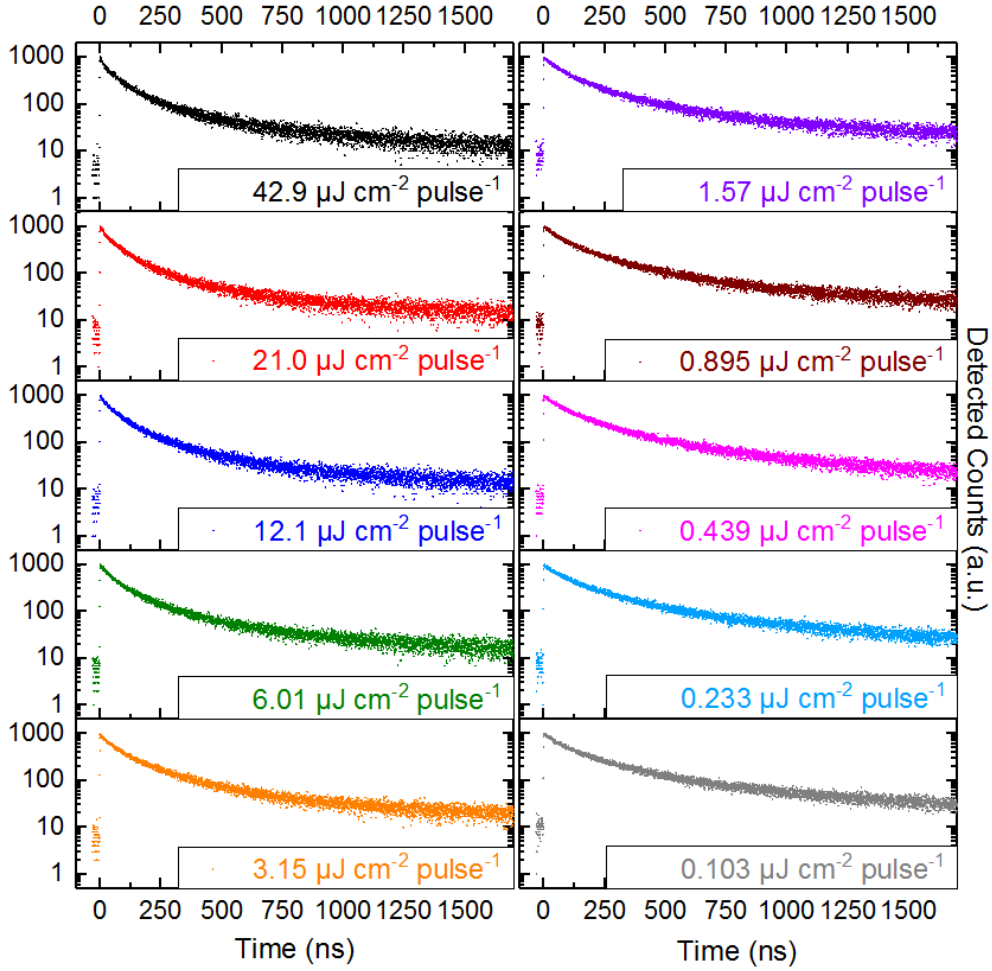

(a)

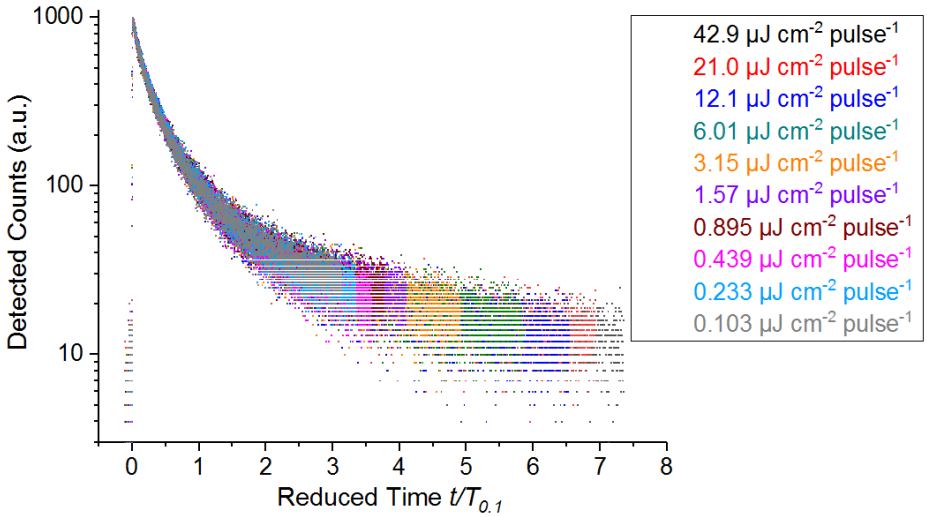

(b)

Figure 5.9: PL time decay measurements performed on C5855 at 10 K with varying excitation energy density at an emission energy of 2.301 eV (a) plotted separately (b) plotted together on a reduced time scale.

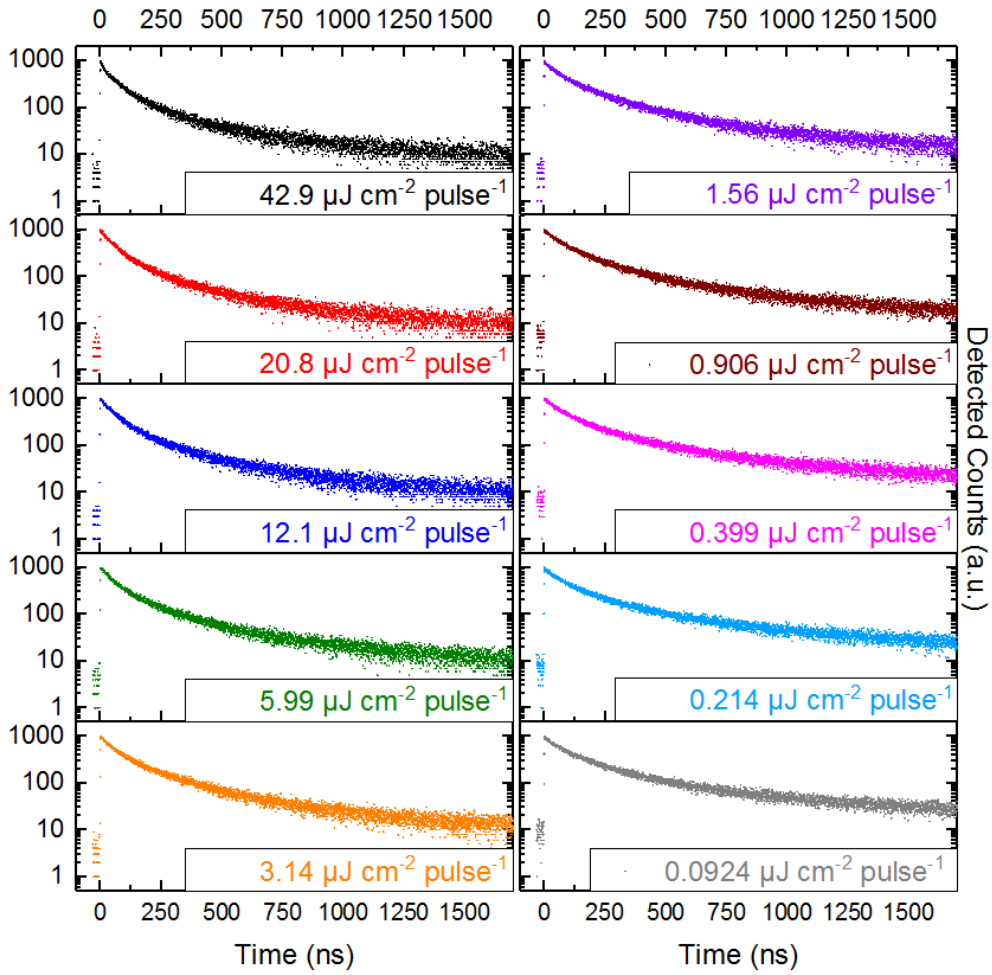

(a)

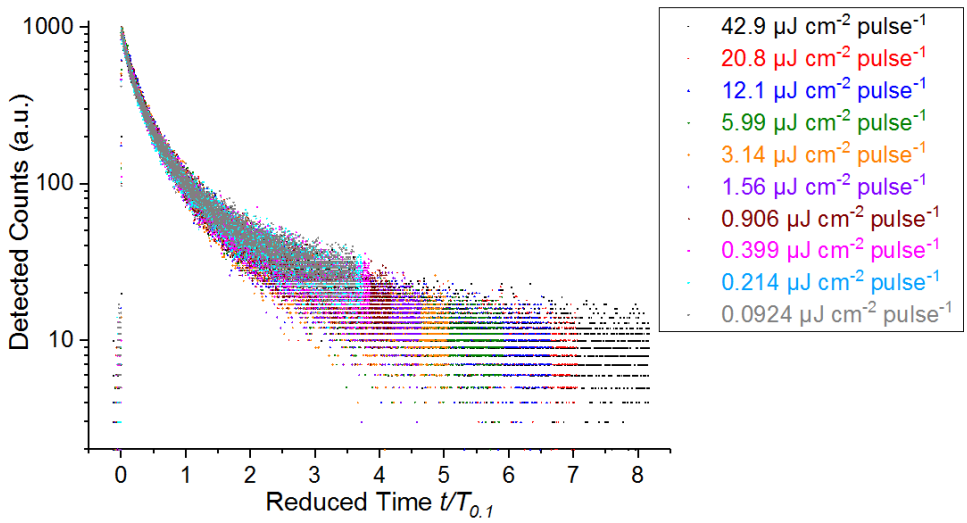

(b)

Figure 5.10: PL time decay measurements performed on C5857 at 10 K with varying excitation energy density at an emission energy of 2.301 eV (a) plotted separately (b) plotted together on a reduced time scale.

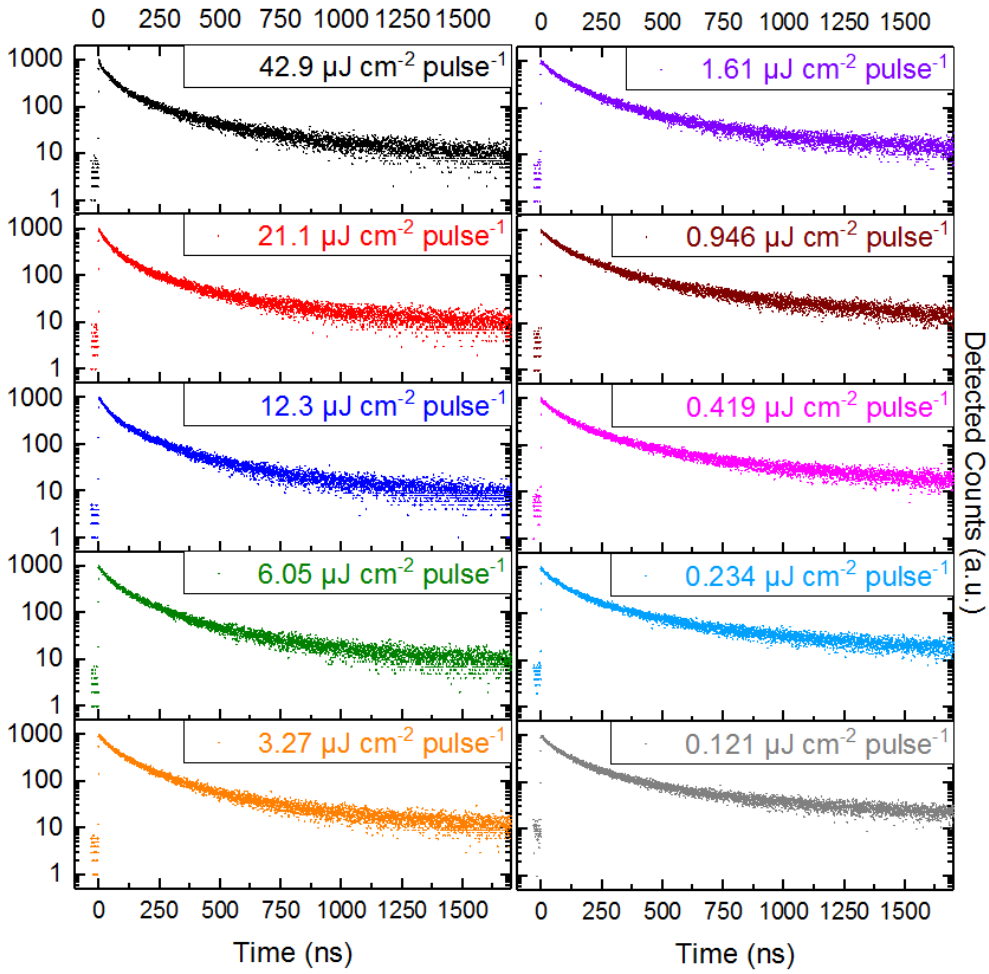

(a)

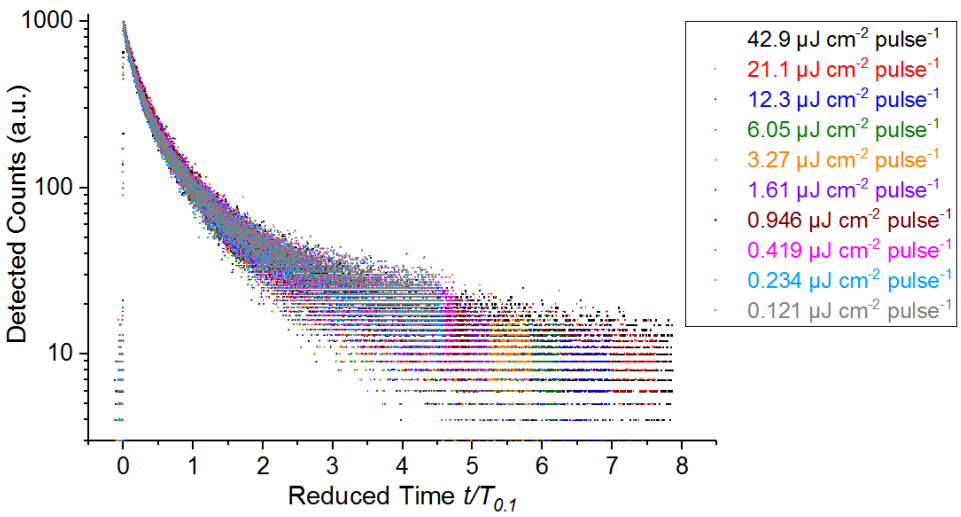

(b)

Figure 5.11: PL time decay measurements performed on C5859 at 10 K with varying excitation energy density at an emission energy of 2.301 eV (a) plotted separately (b) plotted together on a reduced time scale.

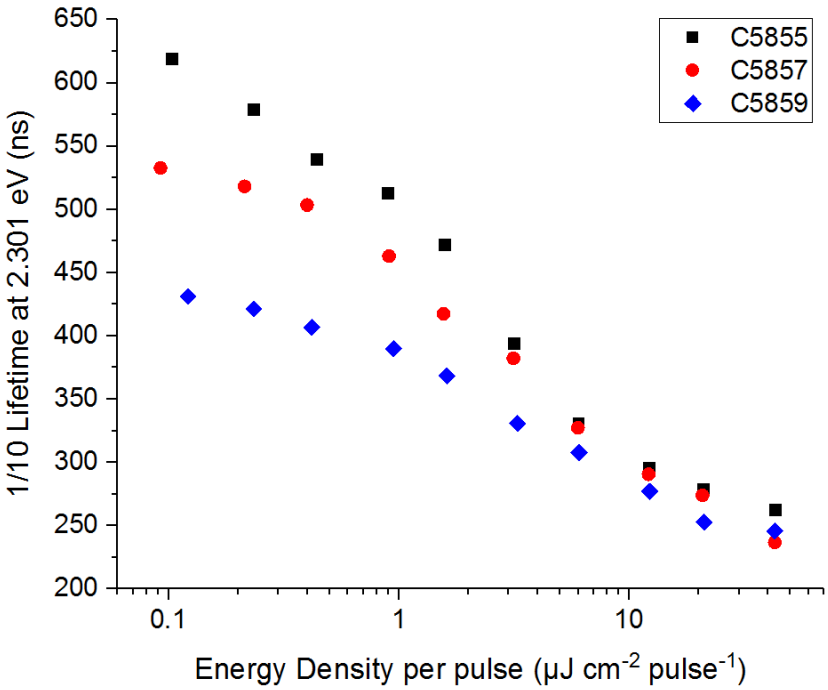

Figure 5.12: The $\frac{1}{10}$ lifetime of the samples at 2.301 eV with varying excitation energy density.

The value of the $T_{0.1}$ lifetime of the carriers decreases with increasing energy density per pulse over the range measured, see Figures 5.12. It appears that the lifetimes of the samples tend towards a plateau at low energy densities; this is consistent with the droop behaviour of InGaN QW samples at 10 K where at low excitation, the PL integrated intensity is linear with excitation power before becoming sub-linear with excitation power as the excitation power is increased. It is assumed that at the plateau region of the droop curve, the recombination mechanism of the carriers is purely radiative; this would correspond to a plateau in the lifetime with varying excitation power, which at this point becomes equal to the radiative lifetime of the sample. It is assumed that carriers cannot move to NRRC at 10 K as they are localized and that the NRRCs which occur in the same position as localization centers are saturated so do not greatly contribute to carrier recombination.

The reduction in lifetime and efficiency with increasing excitation power suggests that a non-radiative carrier recombination mechanism

becomes more dominant with increasing excitation. However, the reduction of lifetimes could also be partly due to carriers occupying weakly localized states where there is a larger electron-hole wavefunction overlap, as shown in the model by Christian *et al.*[9]; high energy broadening can be observed in the PL spectra at the highest excitation powers used, see Figures 5.3 and 5.4, but from the reduced time scale PL decay curves shown in Figures 5.9, 5.10 and 5.11, the PL at 2.301 eV is more characteristic of the typical PL emission rather than of the HEB emission which have been observed to be monoexponential in other works.

Comparing the lifetimes between the samples at 2.301 eV, samples grown at a higher temperature tends to have a longer lifetime compared to the samples grown at a lower temperature; this may be due to the samples with the higher growth temperature having a lower ratio of non-radiative recombination to radiative recombination because of a reduced number of defects. However, the lifetime of an InGaN QW samples also depends on additional factors such as strain-induced and spontaneous polarisation and indium content, which may have been affected by the different growth temperatures and TMI flow rate during the growth of the samples - these differences in the samples may not have been discerned in the XRD measurements. Additionally, the increased defect density in the samples with a lower growth temperature may have led to increased strain relaxation in those samples, thus resulting in a lower strain-induced QCSE and shorter lifetimes. In Figure 5.12, the difference between the lifetimes of the samples is reduced as the excitation power increases; this suggests that at high excitation powers, the samples have the same non-radiative recombination mechanism.

5.3.4 10 K Power Dependent PL Decay Measurements at 2.583 eV and 2.401 eV

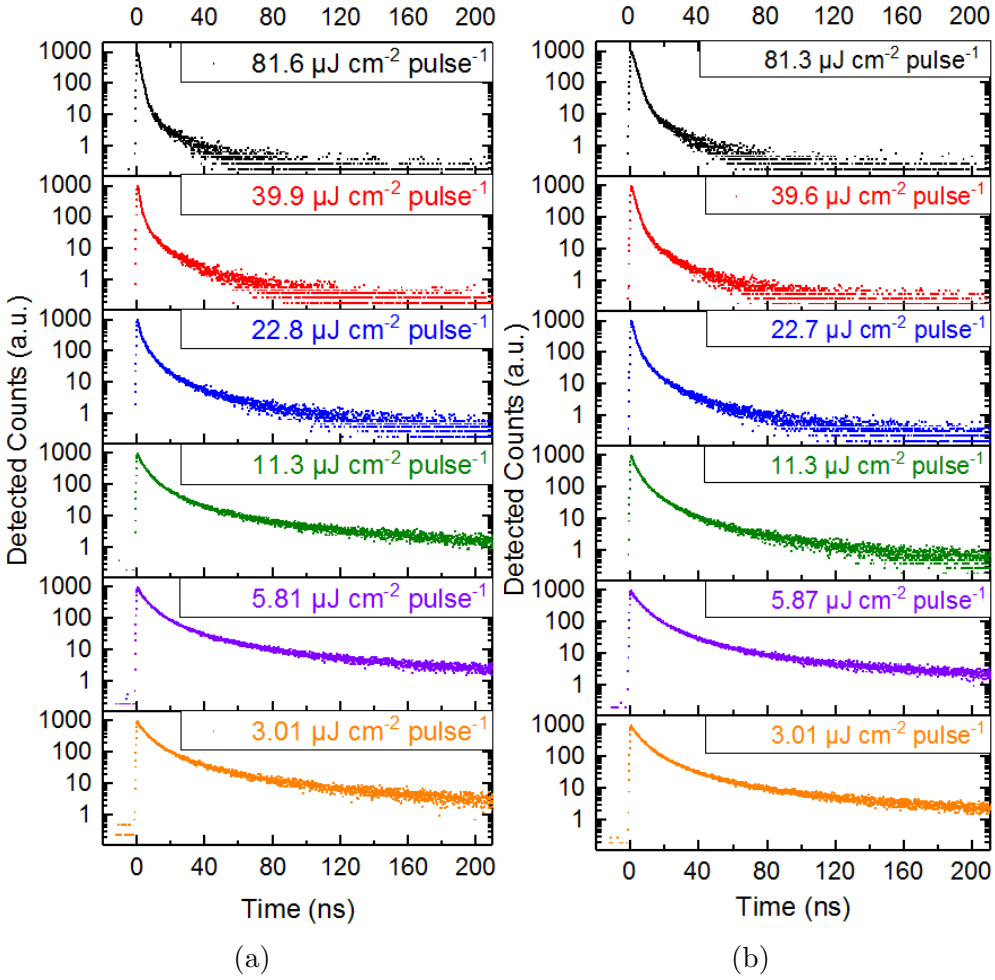

Figure 5.13: PL time decay measurements performed on (a) C5855 and (b) C5857 at 10 K with varying excitation energy density at an emission energy of 2.583 eV.

PL time decay measurements of the samples were also taken at an emission energy of 2.583 eV, where the high energy broadening occurred, at 10 K using setup C and are shown in Figures 5.13 and 5.14a. At the highest excitation energy densities for all three samples, there is an initial monoexponential component in the decay curve; the component becomes less prominent as the excitation energy density decreases. There are also slower, non-monoexponential components in the decay curves indicating

the presence of carriers decaying from the the typical range of more deeply localized states. In contrast to the decay shapes of the samples at 2.301 eV, when plotted against a reduced time scale in Figure 5.14b, the shape of the decay curves can be seen to vary with excitation density for all three samples. The initial monoexponential decays have been previously observed in conjunction with the HEB in InGaN QWs and could be due to carriers recombining from weakly localized states[8, 100, 9].

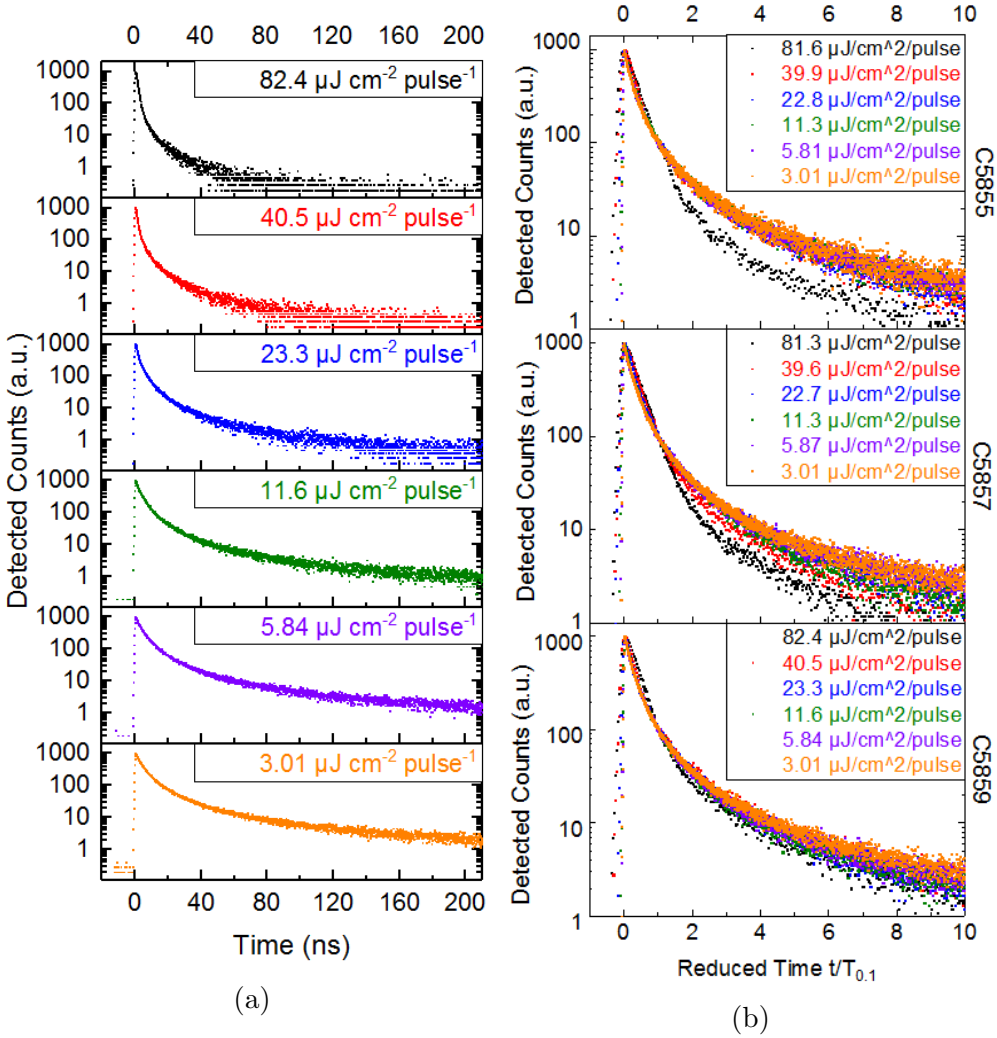

Figure 5.14: (a) PL time decay measurements performed on C5859 at 10 K with varying excitation energy density at an emission energy of 2.583 eV. (b) PL time decay measurements performed on C5855, C5857 and C5859 at 10 K with varying excitation energy density at an emission energy of 2.583 eV plotted on a reduced time scale.

The values of $T_{0.1}$ with varying power density in the samples at an PL emission energy of 2.583 eV are shown in Figure 5.15. In all three samples, the $\frac{1}{10}$ lifetime decreases with increasing energy density as the fast, initial monoexponential decay component and the HEB becomes more prominent. There appears to be no trend across the sample set; the HEB recombination dynamics are not dependent on the growth temperature and defect density variation between the samples.

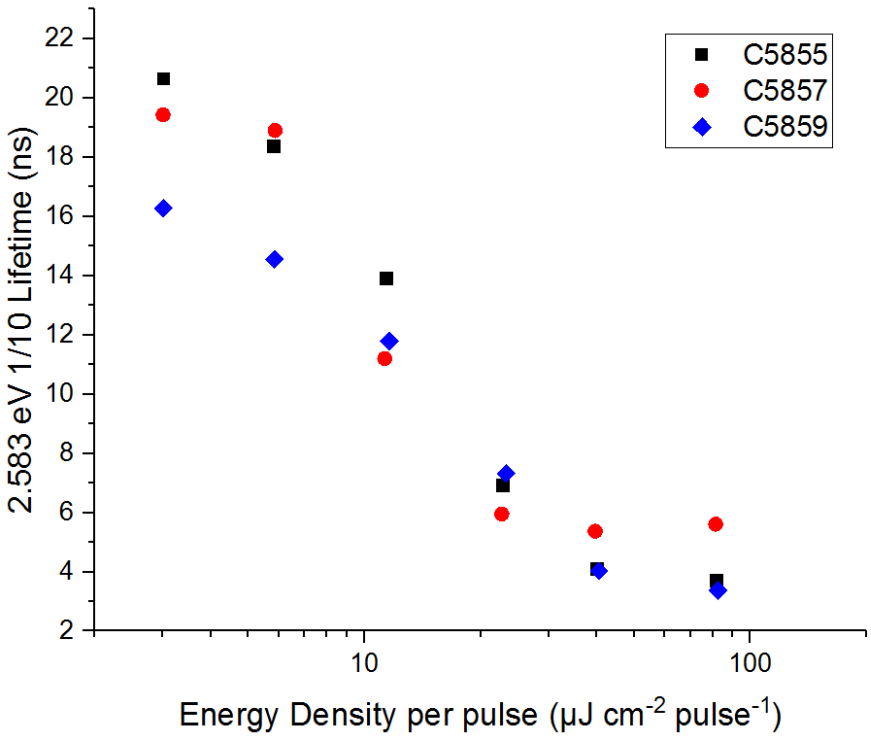

Figure 5.15: The $\frac{1}{10}$ lifetime of the samples at 2.583 eV with varying excitation energy density.

At the highest energy densities, the $\frac{1}{10}$ lifetimes of the samples appear to tend towards the same values, suggesting that the recombination pathways of the samples are the same at the highest energy densities. The sample C5857 appears to have slightly greater $\frac{1}{10}$ lifetime values compared to the other two samples at the two highest energy densities; the decay curves at these energy densities are shown in an expanded view in Figure 5.16.

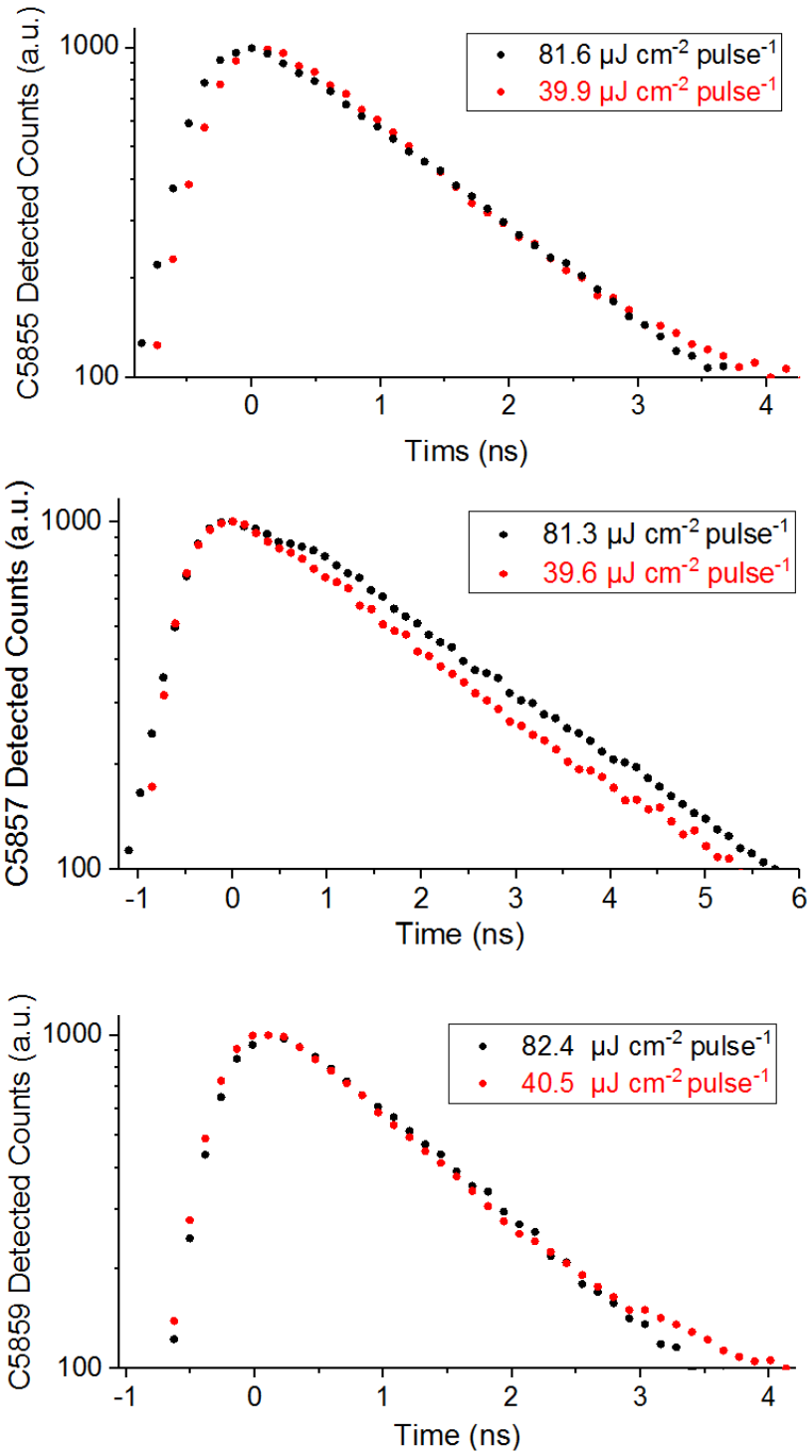

Figure 5.16: An expanded view of the PL time decays of C5855, C5857 and C5859 at an emission energy of 2.583 eV at the highest two excitation energy densities used. The small inflection in the highest excitation density decay curve of C5857 has been attributed to experimental error.

In addition to PL time decay measurements carried out at 2.301 eV, where the PL emission was mainly from the recombination of carriers in the typical localized states, and at 2.583 eV, where the HEB emission occurred, PL time decay measurements were also performed at intermediate emission energies.

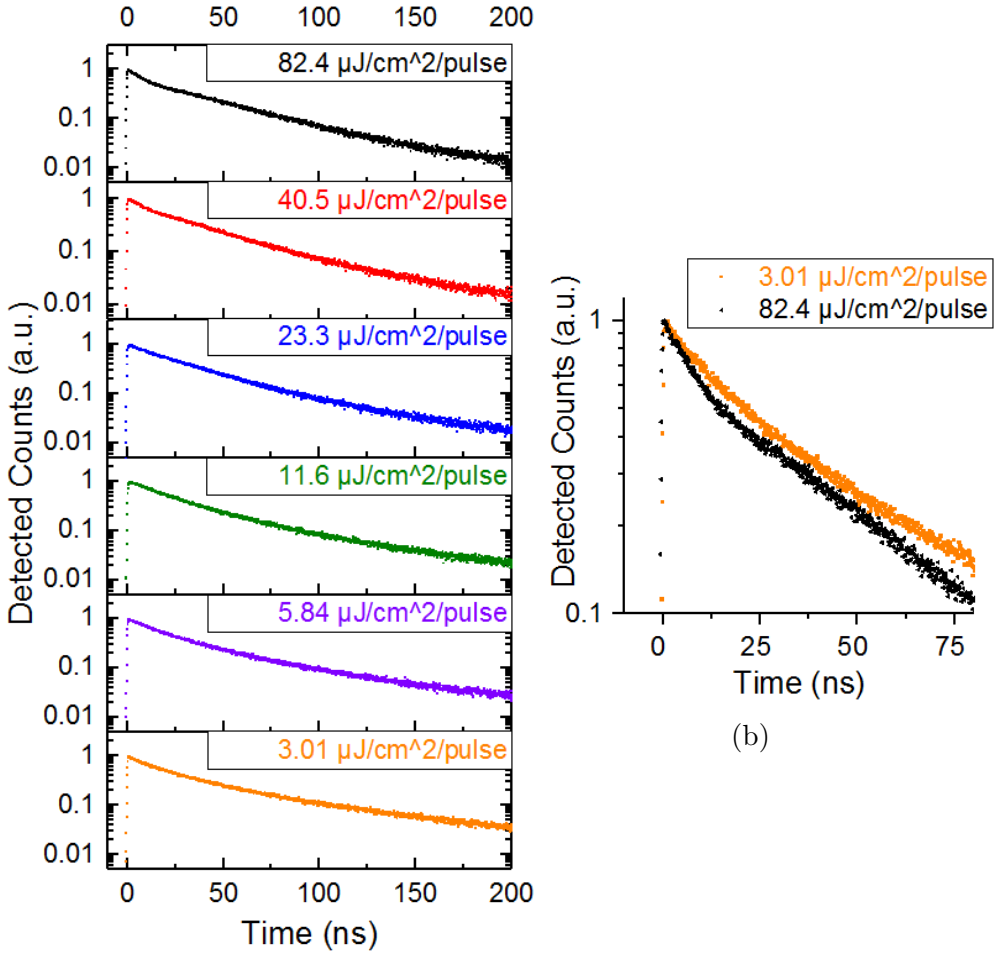

Figure 5.17: (a) PL time decay measurements of the sample C5855 at 2.407 eV with varying excitation energy density. (b) An expanded plot of the highest and lowest excitation energy density measurements from (a) showing an inflection for the highest excitation energy density.

At these intermediate energies, it was clearly observed that there is an inflection in the PL time decay measurements. The PL time decay measurements performed on C5855 at 2.401 eV at varying excitation energy density is shown in Figure 5.17; at the highest excitation energy densities

used, there is an initial monoexponential decay component followed by an inflection and then a slower non-monoexponential decay. This inflection becomes more prominent as the HEB becomes more prominent with increasing excitation power. The inflection could be due to the superposition of the fast monoexponential decays (from carriers recombining from weakly localized states which contribute to the HEB) with the slow non-monoexponential decays from carriers recombining from the typical, deeper localized states that have the same PL emission energy as the weakly localized states.

5.3.5 Additional 10 K Power Dependent PL Decay Measurements of C5855

To further investigate the change in lifetime with excitation power and emission energy, in particular with regards to the plateau in lifetime referred to briefly in Section 5.3.3, power dependent PL decay measurements were performed on the sample C5855 at various emission energies across its spectra, see Figures 5.18, 5.19, 5.20, 5.21, 5.22, 5.23 and 5.24. The time taken for the carriers to decay to a tenth of the peak carrier density for each emission energy and estimated peak carrier density is shown in Figure 5.25.

In Figure 5.25, there is a plateau in the lifetime at the lower carrier densities at each emission energy; this is consistent with the assumption that at low carrier densities at 10 K, carriers are localized and only undergo radiative recombination. There is a reduction in the lifetime as the peak carrier densities is increased; this reduction occurs at lower carrier densities for PL emission at lower energies compared to PL emission at higher energies. This drop in lifetime with increasing carrier density mirrors efficiency droop. The decrease in lifetime with increasing energy density appears monotonic for the lifetimes measured between 2.250 eV and 2.350 eV. At the the higher energy side of the PL spectrum, 2.400 eV and 2.450 eV, the overall reduction in lifetime with increasing excitation is not monotonic and appears to fluctuate before decreasing more rapidly; this reflects the change in decay shape shown in Figures 5.22, 5.23 and 5.24, where at the higher peak carrier densities, the decays have mono-exponential components and inflections, as discussed previously in Section 5.3.4.

In the theoretical model presented by Christian *et al.*, the reduction in lifetime with excitation energy density is due to the saturation of deeply localized states, leading to carriers being able to access semi-localized states where carriers have greater wavefunction overlaps and hence shorter lifetimes [9]. Based on this work, the initial reduction of lifetimes at lower PL emission energies with increasing carrier density compared to higher PL emission energies observed in Figure 5.25 may be due to the saturation of lower PL emission energy localized states

before the saturation of the higher PL emission energy localized states which are less strongly localized. Alternatively, the overall behaviour of the lifetime shown in Figure 5.25 may be due to the superposition of the lifetime behaviour in the five QWs of the C5855 sample which may not have precisely the same indium content, leading to a staggered reduction in lifetime with increasing excitation across the PL spectrum. Another possible explanation is that the carriers at the lower PL emission energy, deeply localized states have greater access to defect-related NRRC as non-radiative recombination, causing carriers in these states to have a reduced lifetime. This would be consistent with the DADR model of efficiency droop[7]. The carriers localized by indium fluctuations may be spatially closer to defects as the increased strain in the region could lead to more defect formation.

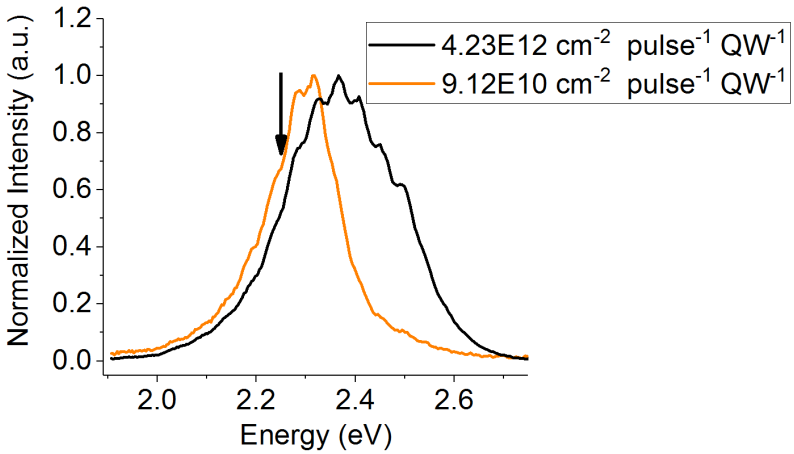

(a)

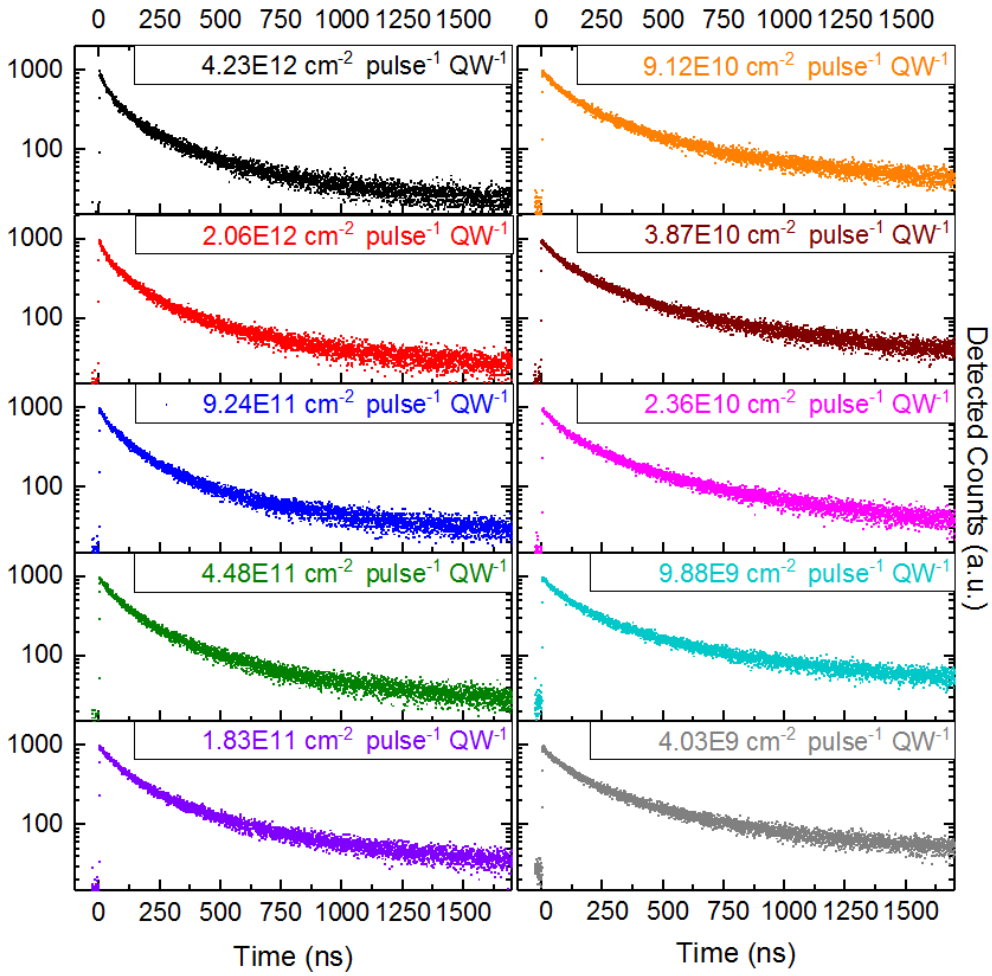

(b)

Figure 5.18: (a) Arrow showing 2.250 eV on the 10 K PL spectra of C5855. (b) 10 K PL time decay measurements of sample C5855 at 2.250 eV at varying estimated peak carrier densities.

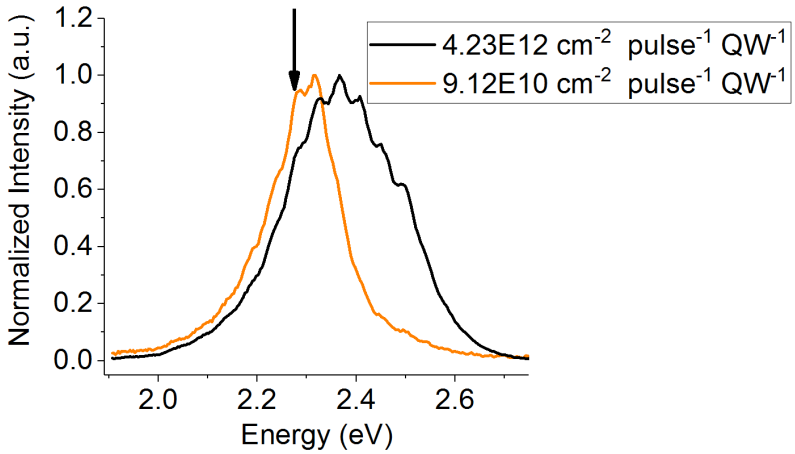

(a)

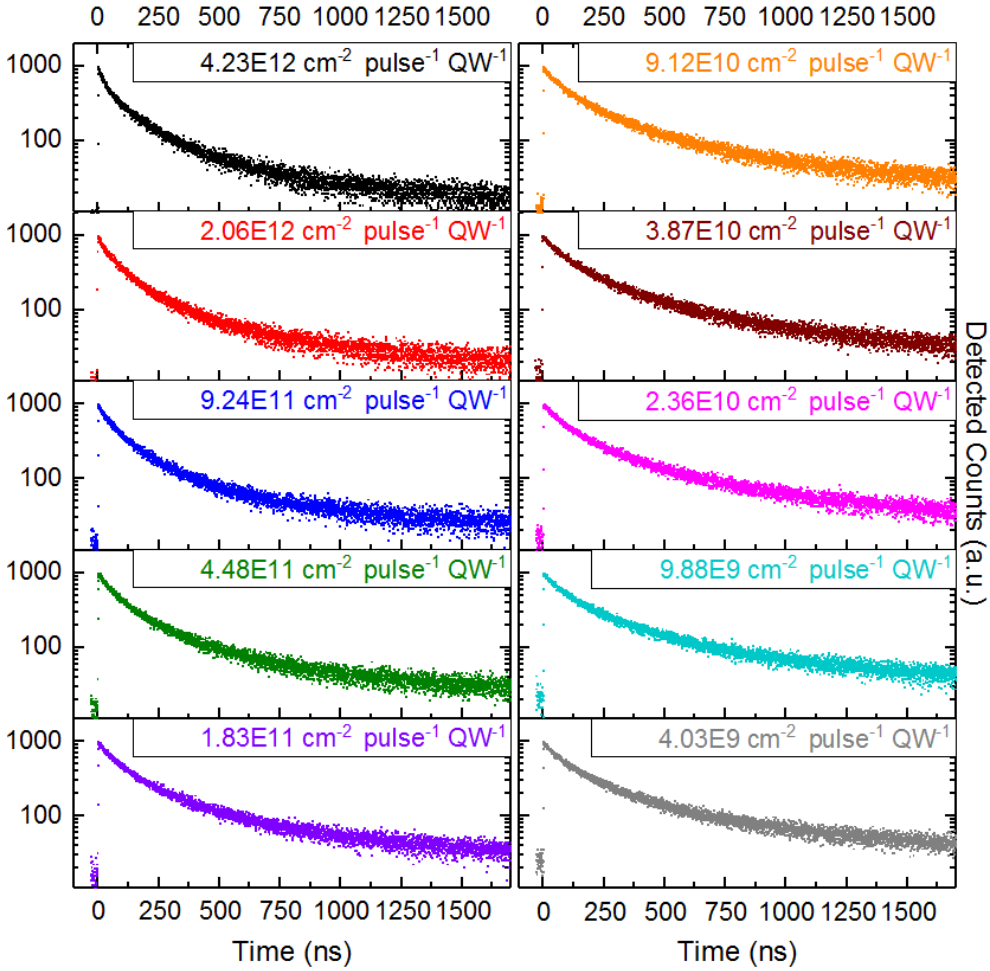

(b)

Figure 5.19: (a) Arrow showing 2.275 eV on the 10 K PL spectra of C5855. (b) 10 K PL time decay measurements of sample C5855 at 2.275 eV at varying estimated peak carrier densities.

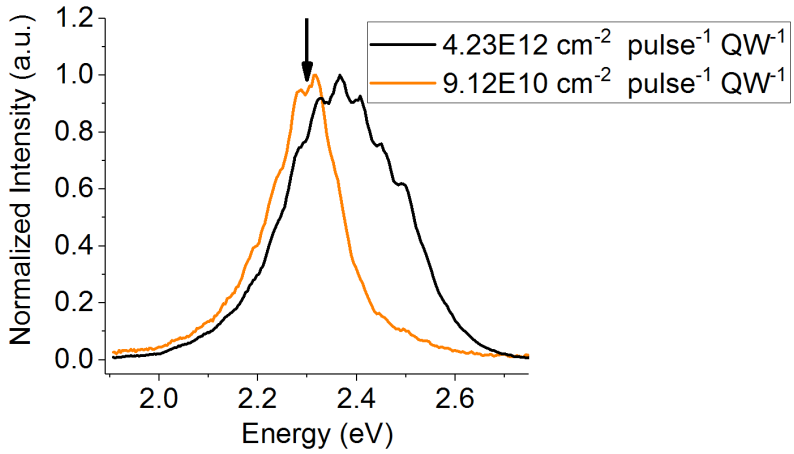

(a)

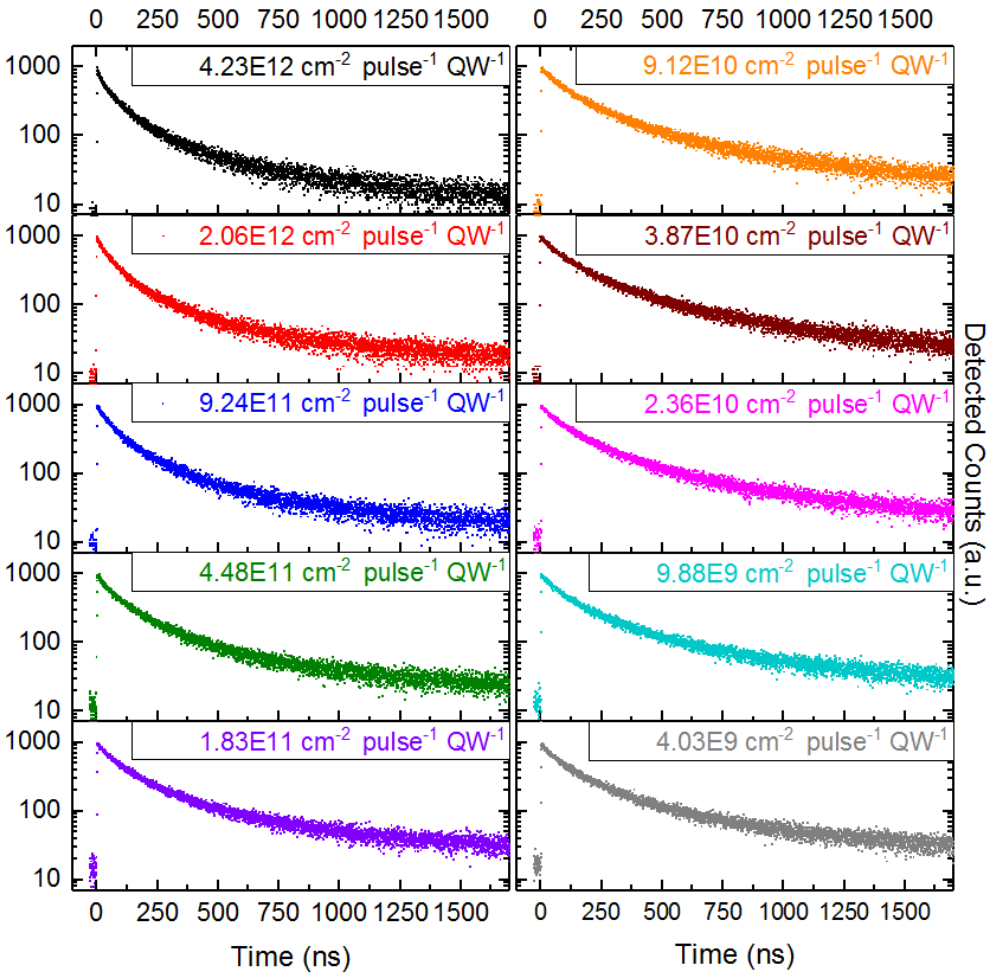

(b)

Figure 5.20: (a) Arrow showing 2.300 eV on the 10 K PL spectra of C5855. (b) 10 K PL time decay measurements of sample C5855 at 2.300 eV at varying estimated peak carrier densities.

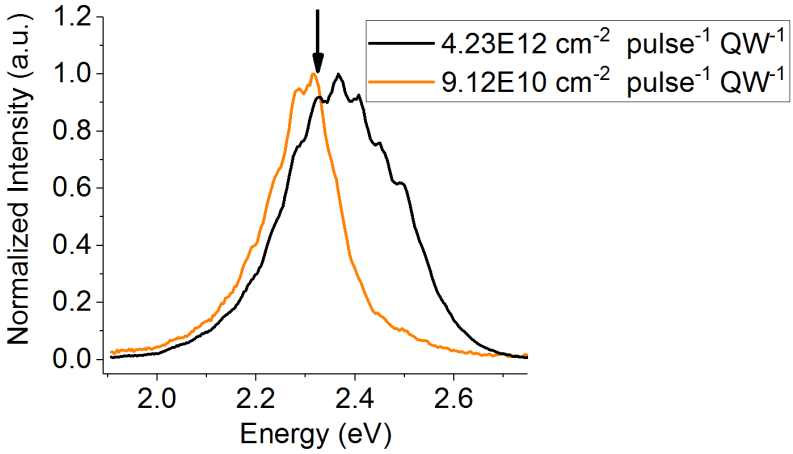

(a)

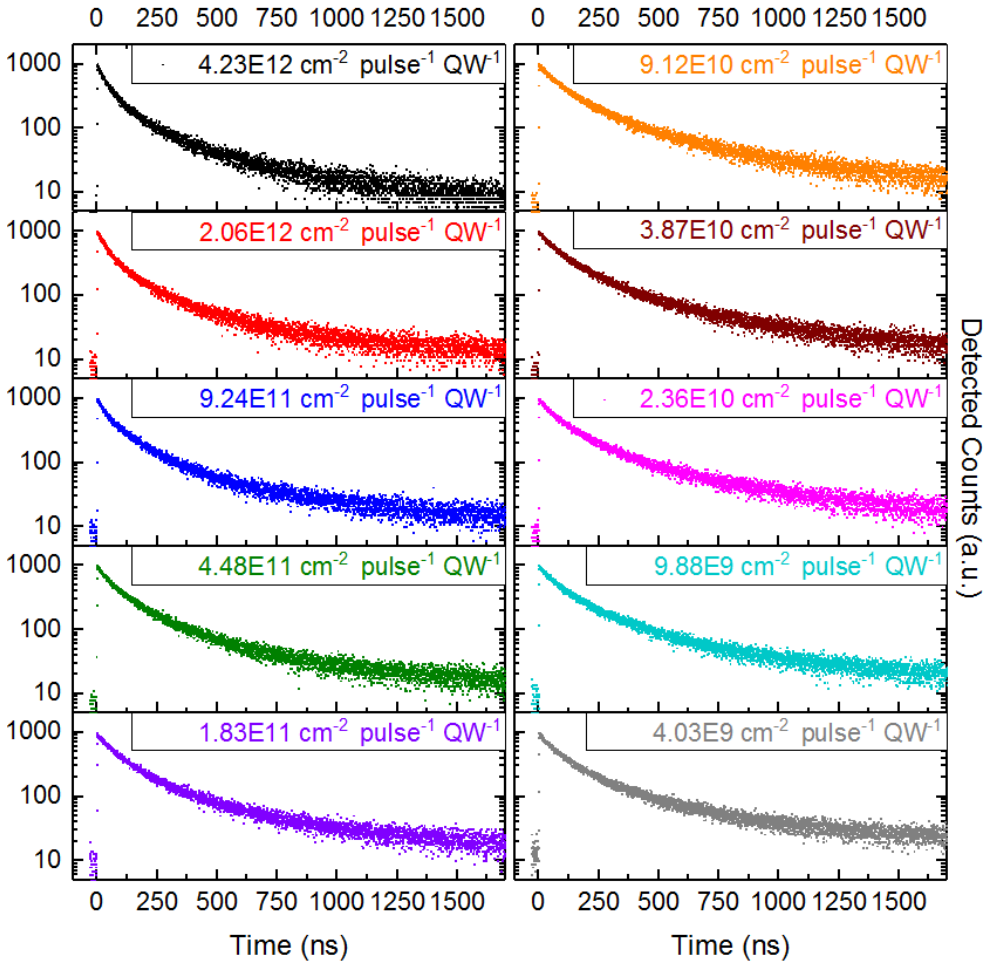

(b)

Figure 5.21: (a) Arrow showing 2.325 eV on the 10 K PL spectra of C5855. (b) 10 K PL time decay measurements of sample C5855 at 2.325 eV at varying estimated peak carrier densities.

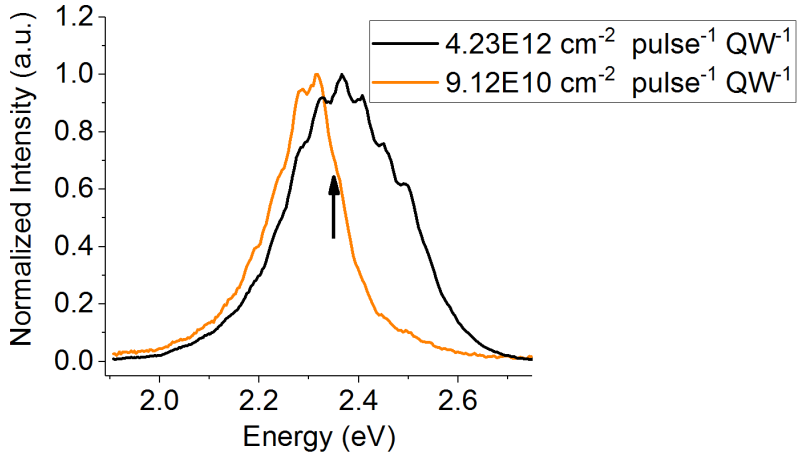

(a)

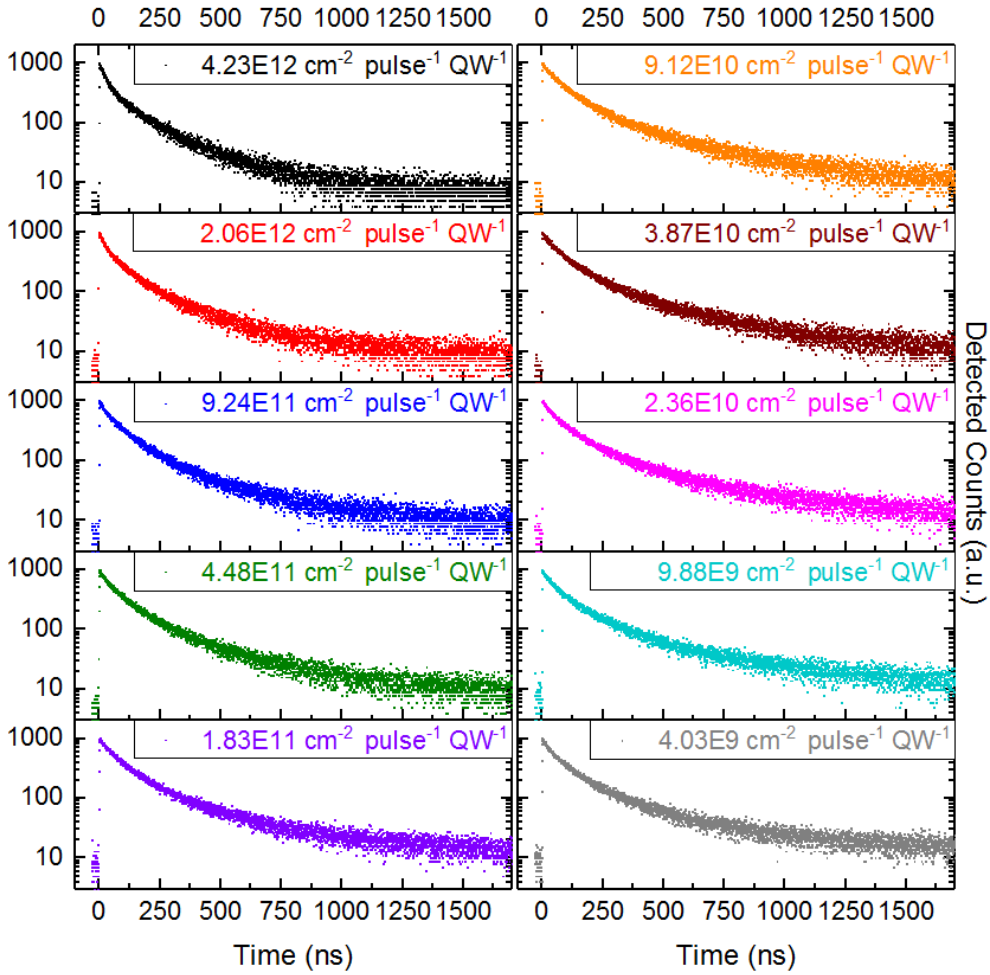

Figure 5.22: (a) Arrow showing 2.350 eV on the 10 K PL spectra of C5855. (b) 10 K PL time decay measurements of sample C5855 at 2.350 eV at varying estimated peak carrier densities.

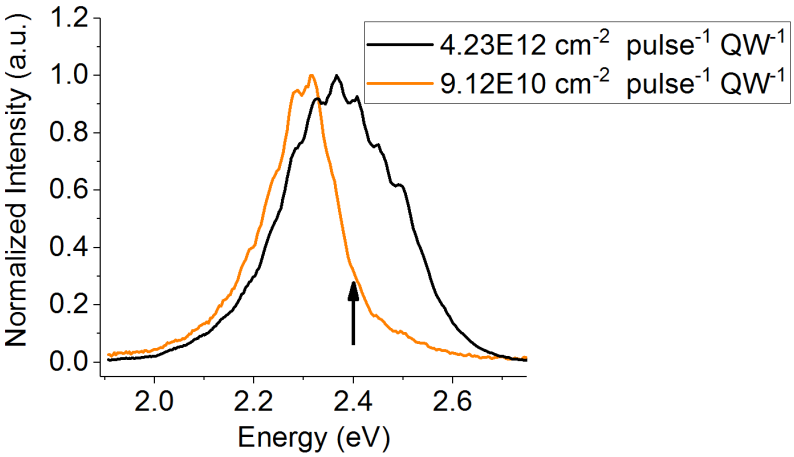

(a)

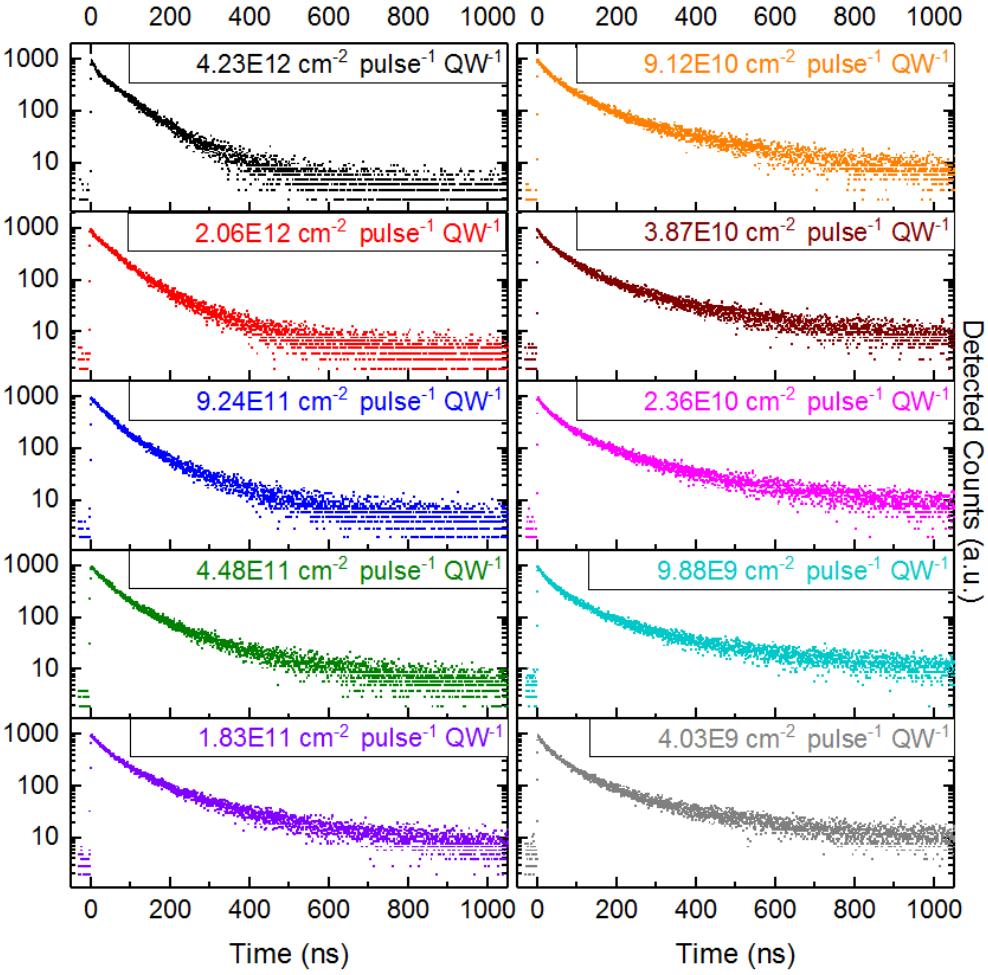

(b)

Figure 5.23: (a) Arrow showing 2.400 eV on the 10 K PL spectra of C5855. (b) 10 K PL time decay measurements of sample C5855 at 2.400 eV at varying estimated peak carrier densities.

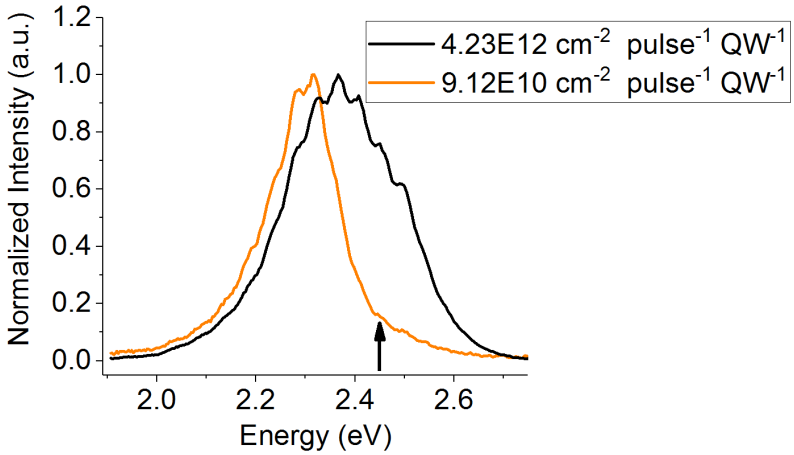

(a)

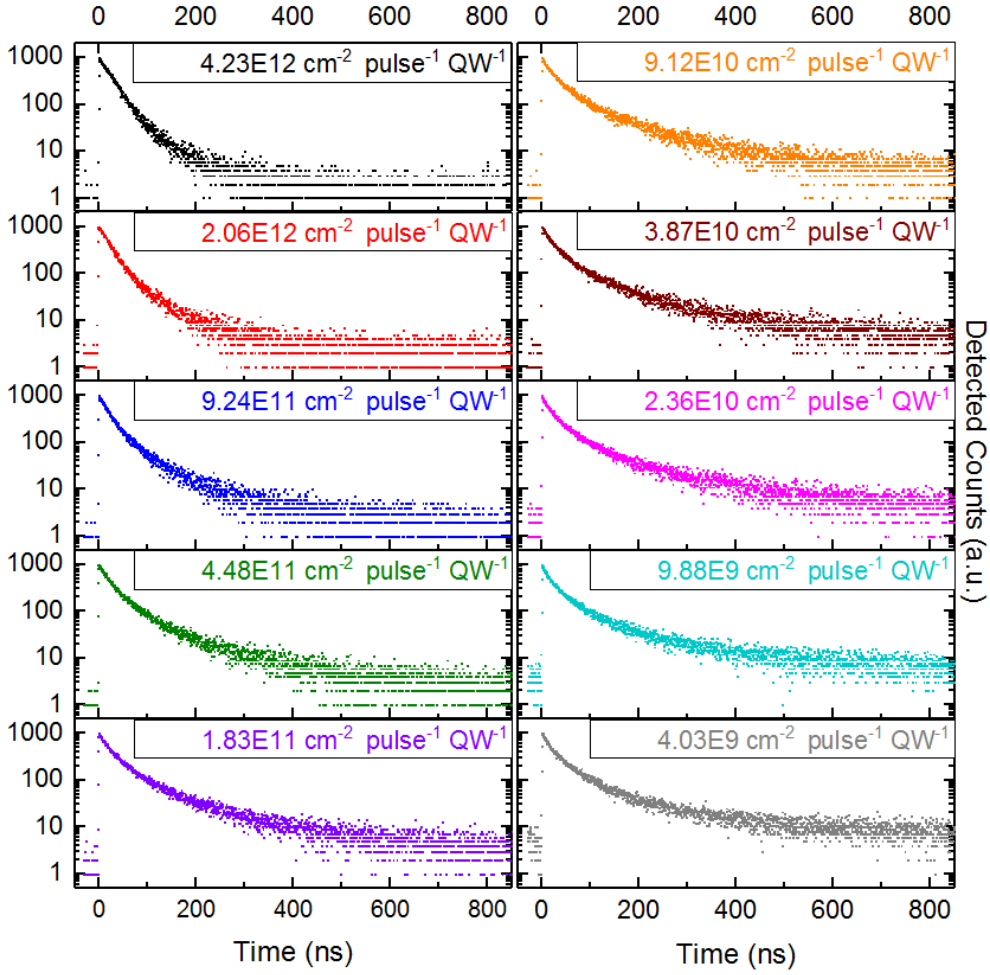

(b)

Figure 5.24: (a) Arrow showing 2.450 eV on the 10 K PL spectra of C5855. (b) 10 K PL time decay measurements of sample C5855 at 2.450 eV at varying estimated peak carrier densities.

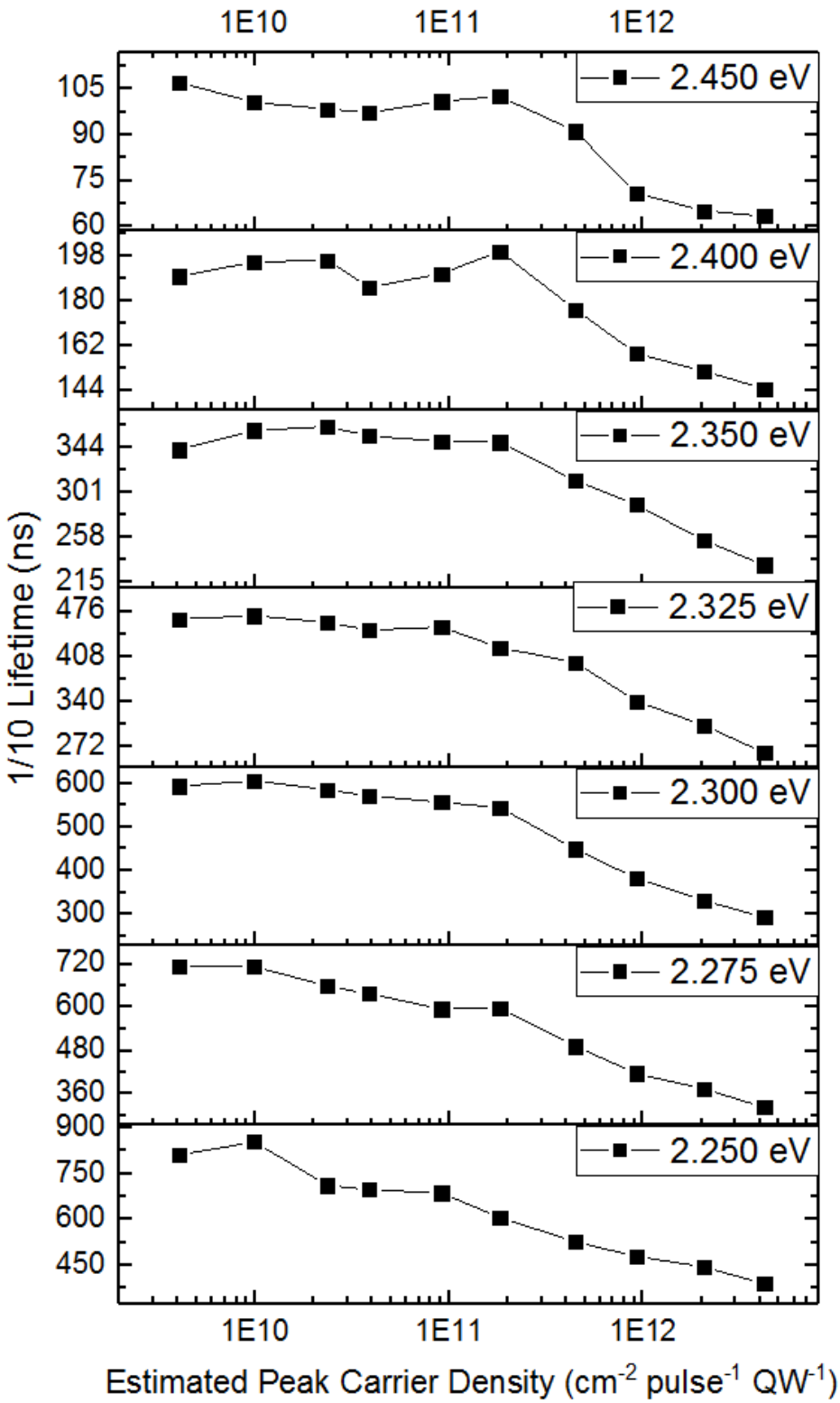

Figure 5.25: The $\frac{1}{10}$ lifetime of the samples at emission energies from 2.250 eV to 2.450 eV with varying estimated peak carrier density.

5.4 Summary

Three InGaN/GaN MQW samples grown at different temperatures to obtain a range of defect densities were investigated; during the 2-T growth of the samples, the flow rate of the indium precursor was varied between the samples to maintain a similar level of indium incorporation for each sample despite their different growth temperatures. The samples were previously studied by Hammersley *et al.* and Ding *et al.* who concluded that the samples with the higher growth temperatures have lower defect density[141, 148]; Hammersley *et al.* also observed that the samples with the higher growth temperature had higher IQEs at 300 K. 10 K TRPL and 10 K power dependent TIPL and PL time decay measurements were performed on the samples to investigate the effect of defect density on efficiency droop and the HEB; the HEB typically occurs at the high carrier densities for which droop is observed[9] and efficiency droop may be due to the delocalization of carriers granting carriers access to defect non-radiative recombination centers[7].

In the 10 K power dependent TIPL measurements, it was observed that the sample with the highest growth temperature and the smallest defect density exhibited efficiency droop at a higher excitation power density compared to the other two samples. In the 10 K power dependent PL decay measurements at the peak emission energy, the sample with the highest growth temperature was observed to have the longest lifetime; this may be because the samples with higher growth temperatures and smaller defect densities are less susceptible to non-radiative recombination triggered by high excitation densities. However, the variation in lifetime could be due to other variations between the samples resulting from their different growth temperatures, such as strain. In previous studies comparing the droop behaviour of InGaN QWs with varying defect densities, efficiency droop have been observed to be independent of threading dislocation defect density[149, 137].

In the 10 K power dependent PL decay measurements at the high energy side of the PL spectra, under the highest excitation energy densities, an initial mono-exponential component in the PL time decay which corresponded to the high energy broadening of the PL spectra was ob-

served, as previously reported by Sun *et al.* and Davies *et al.*[100, 8]. An inflection in the PL time decay, possibly caused by the superposition of PL time decays from carriers recombining from both weakly localized HEB states and strongly localized states with the same emission energy, was observed in the PL decay measurements performed at 10 K at an intermediate energy between the high energy broadening and the main emission peak energy. In the 10 K TRPL, 10 K power dependent TIPL and 10 K power dependent PL decay measurements at the high energy side of the PL spectra, no trend was observed in the HEB behaviour of the samples; it appears that the magnitude and width of the HEB is not dependent on sample growth temperature or defect density.

Additionally, more extensive excitation power varying PL time decay measurements were performed on sample C5855 at 10 K across its PL spectrum at seven emission energies. It was observed that the lifetime at a given emission energy was constant for low carrier densities and decreased at high carrier densities. For the lowest five emission energies, this decrease was monotonic and for the highest two emission energies, which corresponded roughly to the HEB, the decrease in lifetime appears to be more abrupt. The abrupt reduction in lifetime reflected the change in the decay shape observed at the the HEB, where fast monoexponential components and inflections are present in the decay. Comparing all the emission energies, the decrease in lifetime occurs at a lower estimated peak carrier density at lower emission energies. This may be due to the saturation of lower PL emission energy localized states before the higher PL emission energy localized states, which are more weakly localized. The trend may also be caused by the superposition of the lifetime behaviour of the five QWs in C5855, which may have slightly different indium compositions. Another possible explanation of the trend is that the carriers at the lower PL emission energy, more deeply localized states may have greater access to defect-related non-radiative recombination centers.

Chapter 6

Conclusion and Future Work

6.1 Varying the Number of QWs in Green InGaN/GaN QW samples

In Chapter 4, the samples with a varying number of QWs (1, 3, 5 & 10) all had a nominal 25 % indium concentration and were investigated with respect to the effect of QW number on the internal quantum efficiencies of the samples using PL spectroscopy and low temperature PL time decay measurements. At 10 K, the 1 QW sample was measured to have a slower decay than the 3 and 5 QW samples, which had very similar decays; the 10 QW sample was measured to have a faster decay than the 3 and 5 QW samples. The variation in lifetime between the samples may have been due to a combination of strain relaxation in the 10 QW sample, reduced average well thickness with increasing QW number and a different level of indium incorporation amongst the samples.

In the power dependent 300 K IQE measurements, the samples with more QWs tended to have a higher IQE; this was possibly because the samples with more QWs had a lower indium content, leading to a reduced SHR recombination. Additionally, the strain relaxation in the top QW layers of the 10 QW sample and the reduction in QW layer thickness with increasing QW number may have led to a reduction in the QCSE in the samples with more QWs, reducing the susceptibility of the samples with more QWs to thermally activated carrier loss. However, by comparing the 3 and 5 QW samples which have similar lifetimes and therefore

possibly similar levels of strain and indium content, it appears that increasing the QW number increases the IQE of the samples; increasing the QW number may have increased the recapture rate of carriers that have thermally escaped from the QW.

It was assumed during the investigation that the injected carriers from the HeCd laser emitting at 325 nm were equally captured between all the QWs despite the laser having a penetration depth of around 85 nm and the fact that the last QW of the 10 QW sample was approximately 110 nm from the sample surface. To ensure that the injected carriers are able to be captured by all the QWs in the 10 QW sample, a future iteration of the experiment could involve using a lower energy laser that is suitable for below-gap excitation with a sufficiently deep penetration depth or studying InGaN QW samples with a different number of QWs which have barriers which are thin enough for the wells to be coupled.

6.2 Varying the Growth Temperature of InGaN/GaN MQW samples

In Chapter 5, a set of three green light-emitting InGaN MQW samples with varying growth temperatures and defect densities were investigated with respect to the high energy band and their efficiency droop behaviour. In the 10 K PL measurements, the sample with the highest growth temperature and the smallest defect density exhibited efficiency droop at the highest excitation power density. In the 10 K PL time decay measurements at the peak emission energy, the sample with the highest growth temperature was also observed to have the longest lifetime; these results may indicate that the samples with higher growth temperatures and smaller defect densities are less susceptible to non-radiative recombination triggered by high excitation densities. However, the variation in lifetime could be due to other variations between the samples because of their different growth temperatures, such as strain.

In the 10 K PL time decay measurements at the high energy side of the PL spectra under high excitation, there was an initial mono-exponential component in the PL time decay which corresponded to the high energy

broadening of the PL spectra. An inflection was present in the 10 K PL time decay measurements performed at an intermediate energy between the high energy broadening and the main emission peak; it may have been due the superposition of PL time decays from carriers recombining from both weakly localized HEB states and strongly localized states. In the 10 K time-resolved PL, time-integrated PL and PL time decay measurements, the HEB behaviour of the samples did not vary systematically; the HEB did not appear to depend on sample growth temperature or defect density.

More extensive excitation power varying PL time decay measurements were also performed on one of the samples at 10 K across its PL spectrum; the lifetime at a given emission energy was measured to be constant for low carrier densities and decreasing at high carrier densities. At the emission energies distributed around the typical peak emission energy at low excitation, this decrease was monotonic and for the higher emission energies corresponding roughly to the HEB, the decrease in lifetime appeared to be more abrupt. This abrupt lifetime reduction corresponded to the occurrence of the fast monoexponential components and inflections in the decay shape at the the HEB. Overall, the lifetime reduction occurs at a lower peak carrier density for lower emission energies; this may be due to: the saturation of lower energy emitting localized states before the saturation of higher energy ones which are more weakly localized; the superposition of the lifetime behaviour of the five QWs in C5855, which may have varying indium compositions; or carriers at the more deeply localized states having greater access to defect-related non-radiative recombination centers (NRRCs).

There is scope for the variation in lifetime with increasing carrier density across the PL spectrum to be further investigated; performing excitation power varying PL time decay measurements at varying emission energies at 10 K on a single QW sample could remove the possibility that the behaviour is due to variations between QWs within a many QW sample.

References

[1] International Energy Agency, "Light's Labour's Lost", IEA Publications, France, 2006.

[2] World Energy Council, "World Energy Resources Report", World Energy Council, 2016.

[3] Signify, "The LED Lighting Revolution", Koninklijke Philips N.V, 2015.

[4] M. Auf der Maur, A. Pecchia, G. Penazzi, W. Rodrigues and A. Di Carlo, "Efficiency Drop in GreenInGaN/GaNLight Emitting Diodes: The Role of Random Alloy Fluctuations", *Physical Review Letters*, vol. 116, no. 2, 2016.

[5] M. Crawford, "LEDs for Solid-State Lighting: Performance Challenges and Recent Advances", *IEEE Journal of Selected Topics in Quantum Electronics*, vol. 15, no. 4, pp. 1028-1040, 2009.

[6] S. Hammersley, D. Watson-Parris, P. Dawson, M. Godfrey, T. Badcock, M. Kappers, C. McAleese, R. Oliver and C. Humphreys, "The consequences of high injected carrier densities on carrier localization and efficiency droop in InGaN/GaN quantum well structures", *Journal of Applied Physics*, vol. 111, no. 8, p. 083512, 2012.

[7] J. Hader, J. Moloney and S. Koch, "Density-activated defect recombination as a possible explanation for the efficiency droop in GaN-based diodes", *Applied Physics Letters*, vol. 96, no. 22, p. 221106, 2010.

[8] M. Davies, T. Badcock, P. Dawson, M. Kappers, R. Oliver and C. Humphreys, "High excitation carrier density recombination dynamics of InGaN/GaN quantum well structures: Possible relevance to efficiency droop", *Applied Physics Letters*, vol. 102, no. 2, p. 022106, 2013.

[9] G. Christian, S. Schulz, M. Kappers, C. Humphreys, R. Oliver and P. Dawson, "Recombination from polar InGaN/GaN quantum well structures at high excitation carrier densities", *Physical Review B*, vol. 98, no. 15, 2018.

[10] F. Massabuau, M. Davies, F. Oehler, S. Pamenter, E. Thrush, M. Kappers, A. Kovács, T. Williams, M. Hopkins, C. Humphreys, P. Dawson, R. Dunin-Borkowski, J. Etheridge, D. Allsopp and R. Oliver, "The impact of trench defects in InGaN/GaN light emitting diodes and implications for the "green gap" problem", *Applied Physics Letters*, vol. 105, no. 11, p. 112110, 2014.

[11] J. Smalc-Koziorowska, E. Grzanka, R. Czernecki, D. Schiavon and M. Leszczyński, "Elimination of trench defects and V-pits from InGaN/GaN structures", *Applied Physics Letters*, vol. 106, no. 10, p. 101905, 2015.

[12] W. Johnson, J. Parson and M. Crew, "Nitrogen Compounds of Gallium. III", *The Journal of Physical Chemistry*, vol. 36, no. 10, pp. 2651-2654, 1931.

[13] H. Maruska and J. Tietjen, "The Preparation and Properties of Vapour-Deposited Single-Crystalline GaN", *Applied Physics Letters*, vol. 15, no. 10, pp. 327-329, 1969.

[14] H. Maruska, D. Stevenson and J. Pankove, "Violet luminescence of Mg-doped GaN", *Applied Physics Letter*s, vol. 22, no. 6, pp. 303-305, 1973.

[15] M. Ilegems and R. Dingle, "Luminescence of Be- and Mg-doped GaN", *Journal of Applied Physics*, vol. 44, no. 9, pp. 4234-4235, 1973.

[16] S. Yoshida, S. Misawa and S. Gonda, "Improvements on the electrical and luminescent properties of reactive molecular beam epitaxially grown GaN films by using AlN-coated sapphire substrates", *Applied Physics Letters*, vol. 42, no. 5, pp. 427-429, 1983.

[17] H. Amano, N. Sawaki, I. Akasaki and Y. Toyoda, "Metalorganic vapor phase epitaxial growth of a high quality GaN film using an AlN buffer layer", *Applied Physics Letters*, vol. 48, no. 5, pp. 353-355, 1986.

[18] S. Nakamura, "GaN Growth Using GaN Buffer Layer", *Japanese Journal of Applied Physics*, vol. 30, no. 2, 10, pp. L1705-L1707, 1991.

[19] H. Amano, M. Kito, K. Hiramatsu and I. Akasaki, "P-Type Conduction in Mg-Doped GaN Treated with Low-Energy Electron Beam Irradiation (LEEBI)", *Japanese Journal of Applied Physics*, vol. 28, no. 2, 12, pp. L2112-L2114, 1989.

[20] S. Nakamura, T. Mukai, M. Senoh and N. Iwasa, "Thermal Annealing Effects on P-Type Mg-Doped GaN Films", *Japanese Journal of Applied Physics*, vol. 31, no. 2, 2, pp. L139-L142, 1992.

[21] S. Nakamura, N. Iwasa, M. Senoh and T. Mukai, "Hole Compensation Mechanism of P-Type GaN Films", *Japanese Journal of Applied Physics*, vol. 31, no. 1, 5, pp. 1258-1266, 1992.

[22] J. Vechten, J. Zook, R. Horning and B. Goldenberg, "Defeating Compensation in Wide Gap Semiconductors by Growing in H that is Removed by Low Temperature De-Ionizing Radiation", *Japanese Journal of Applied Physics*, vol. 31, no. 1, 11, pp. 3662-3663, 1992.

[23] J. Neugebauer and C. Van de Walle, "Hydrogen in GaN: Novel Aspects of a Common Impurity", *Physical Review Letters*, vol. 75, no. 24, pp. 4452-4455, 1995.

[24] J. Neugebauer and C. Van de Walle, "Role of hydrogen in doping of GaN", *Applied Physics Letters*, vol. 68, no. 13, pp. 1829-1831, 1996.

[25] Y. Okamoto, M. Saito and A. Oshiyama, "First-Principles Calculations on Mg Impurity and Mg-H Complex in GaN", *Japanese Journal of Applied Physics*, vol. 35, no. 2, 7, pp. L807-L809, 1996.

[26] K. Itoh, T. Kawamoto, H. Amano, K. Hiramatsu and I. Akasaki, "Metalorganic Vapor Phase Epitaxial Growth and Properties of GaN/Al0.1Ga0.9N Layered Structures", *Japanese Journal of Applied Physics*, vol. 30, no. 1, 9, pp. 1924-1927, 1991.

[27] N. Yoshimoto, T. Matsuoka, T. Sasaki and A. Katsui, "Photoluminescence of InGaN films grown at high temperature by metalorganic vapor phase epitaxy", *Applied Physics Letters*, vol. 59, no. 18, pp. 2251-2253, 1991.

[28] S. Nakamura, M. Senoh and T. Mukai, "P-GaN/N-InGaN/N-GaN Double-Heterostructure Blue-Light-Emitting Diodes", *Japanese Journal of Applied Physics*, vol. 32, no. 2, 1, pp. L8-L11, 1993.

[29] S. Nakamura, M. Senoh, N. Iwasa, S. Nagahama, T. Yamada and T. Mukai, "Superbright Green InGaN Single-Quantum-Well-Structure Light-Emitting Diodes", *Japanese Journal of Applied Physics*, vol. 34, no. 2, 10, pp. L1332-L1335, 1995.

[30] S. Nakamura, M. Senoh, N. Iwasa and S. Nagahama, "High-Brightness InGaN Blue, Green and Yellow Light-Emitting Diodes with Quantum Well Structures", *Japanese Journal of Applied Physics*, vol. 34, no. 2, 7, pp. L797-L799, 1995.

[31] S. Nakamura, M. Senoh, S. Nagahama, N. Iwasa, T. Yamada, T. Matsushita, H. Kiyoku and Y. Sugimoto, "InGaN-Based Multi-Quantum-Well-Structure Laser Diodes", *Japanese Journal of Applied Physics*, vol. 35, no. 2, 1, pp. L74-L76, 1996.

[32] M. Khan, S. Krishnankutty, R. Skogman, J. Kuznia, D. Olson and T. George, "Vertical–cavity stimulated emission from photopumped InGaN/GaN heterojunctions at room temperature", *Applied Physics Letters*, vol. 65, no. 5, pp. 520-521, 1994.

[33] H. Amano, T. Tanaka, Y. Kunii, K. Kato, S. Kim and I. Akasaki, "Room-temperature violet stimulated emission from optically pumped AlGaN/GaInN double heterostructure", *Applied Physics Letters*, vol. 64, no. 11, pp. 1377-1379, 1994.

[34] H. Young, R. Freedman and A. Ford, *Sears and Zemanksy's University Physics with Modern Physics University of Sheffield Edition*, 13th ed. Harlow, Essex: Pearson Education Limited, 2011, p. 1340.

[35] M. Asif Khan, J. Kuznia, A. Bhattarai and D. Olson, "Metal semiconductor field effect transistor based on single crystal GaN", *Applied Physics Letters*, vol. 62, no. 15, pp. 1786-1787, 1993.

[36] U. Mishra, Shen Likun, T. Kazior and Yi-Feng Wu, "GaN-Based RF Power Devices and Amplifiers", *Proceedings of the IEEE*, vol. 96, no. 2, pp. 287-305, 2008.

[37] L. Liu and J. Edgar, "Substrates for gallium nitride epitaxy", Materials Science and Engineering: R: Reports, vol. 37, no. 3, pp. 61-127, 2002.

[38] I. Vurgaftman and J. Meyer, "Band parameters for nitrogen-containing semiconductors", *Journal of Applied Physics*, vol. 94, no. 6, pp. 3675-3696, 2003.

[39] W. Yim, E. Stofko, P. Zanzucchi, J. Pankove, M. Ettenberg and S. Gilbert, "Epitaxially grown AlN and its optical band gap", *Journal of Applied Physics*, vol. 44, no. 1, pp. 292-296, 1973.

[40] P. Perry and R. Rutz, "The optical absorption edge of single-crystal AlN prepared by a close-spaced vapor process", *Applied Physics Letters*, vol. 33, no. 4, pp. 319-321, 1978.

[41] B. Monemar, "Fundamental energy gap of GaN from photoluminescence excitation spectra", *Physical Review B*, vol. 10, no. 2, pp. 676-681, 1974.

[42] Q. Guo and A. Yoshida, "Temperature Dependence of Band Gap Change in InN and AlN", *Japanese Journal of Applied Physics*, vol. 33, no. 1, 5, pp. 2453-2456, 1994.

[43] S. Tripathy, R. Soni, H. Asahi, K. Iwata, R. Kuroiwa, K. Asami and S. Gonda, "Optical properties of GaN layers grown on C-, A-, R-, and M-plane sapphire substrates by gas source molecular beam epitaxy", Journal of Applied Physics, vol. 85, no. 12, pp. 8386-8399, 1999.

[44] B. Gil, *Group III nitride semiconductor compounds*, 1st ed. Oxford University Press, 2002, p. 123.

[45] E. Etzkorn and D. Clarke, "Cracking of GaN films", *Journal of Applied Physics*, vol. 89, no. 2, pp. 1025-1034, 2001.

[46] H. Okumura, K. Balakrishnan, H. Hamaguchi, Takayoshi Koizumi, S. Chichibu, H. Nakanishi, T. Nagatomo and S. Yoshida, "Analysis of MBE growth mode for GaN epilayers by RHEED", *Journal of Crystal Growth*, vol. 189-190, pp. 364-369, 1998.

[47] K. Seshan, *Handbook of thin-film deposition processes and techniques*, 2nd ed. Norwich, N.Y.: Noyes Publications, 2001, p. 389.

[48] F. Bernardini and V. Fiorentini, "Nonlinear macroscopic polarization in III-V nitride alloys", Physical Review B, vol. 64, no. 8, 2001.

[49] V. Fiorentini, F. Bernardini and O. Ambacher, "Evidence for nonlinear macroscopic polarization in III–V nitride alloy heterostructures", *Applied Physics Letters*, vol. 80, no. 7, pp. 1204-1206, 2002.

[50] P. Prodhomme, A. Beya-Wakata and G. Bester, "Nonlinear piezoelectricity in wurtzite semiconductors", *Physical Review B*, vol. 88, no. 12, 2013.

[51] J. Lahnemann, O. Brandt, U. Jahn, C. Pfuller, C. Roder, P. Dogan, F. Grosse, A. Belabbes, F. Bechstedt, A. Trampert and L. Geelhaar, "Direct experimental determination of the spontaneous polarization of GaN", *Physical Review B*, vol. 86, no. 8, 2012.

[52] P. Harrison and A. Valavanis, *Quantum wells, wires and dots*, 3rd ed. West Sussex, United Kingdom: John Wiley & Sons, Inc, 2011, p. 209.

[53] F. Bernardini, V. Fiorentini and D. Vanderbilt, "Spontaneous polarization and piezoelectric constants of III-V nitrides", *Physical Review B*, vol. 56, no. 16, pp. R10024-R10027, 1997.

[54] F. Bernardini, V. Fiorentini and D. Vanderbilt, "Accurate calculation of polarization-related quantities in semiconductors", *Physical Review B*, vol. 63, no. 19, 2001.

[55] K. Tsubouchi and N. Mikoshiba, "Zero-Temperature-Coefficient SAW Devices on AlN Epitaxial Films", *IEEE Transactions on Sonics and Ultrasonics*, vol. 32, no. 5, pp. 634-644, 1985.

[56] T. Takeuchi, S. Sota, M. Katsuragawa, M. Komori, H. Takeuchi, H. Amano and I. Akasaki, "Quantum-Confined Stark Effect due to Piezoelectric Fields in GaInN Strained Quantum Wells", *Japanese Journal of Applied Physics*, vol. 36, no. 2, 4, pp.L382-L385, 1997.

[57] P. Lefebvre, A. Morel, M. Gallart, T. Taliercio, J. Allègre, B. Gil, H. Mathieu, B. Damilano, N. Grandjean and J. Massies, "High internal electric field in a graded-width InGaN/GaN quantum well: Accurate determination by time-resolved photoluminescence spectroscopy", *Applied Physics Letters*, vol. 78, no. 9, pp. 1252-1254, 2001.

[58] A. Bonfiglio, M. Lomascolo, G. Traetta, R. Cingolani, A. Di Carlo, F. Della Sala, P. Lugli, A. Botchkarev and H. Morkoc, "Well-width

dependence of the ground level emission of GaN/AlGaN quantum wells", *Journal of Applied Physics*, vol. 87, no. 5, pp. 2289-2292, 2000.

[59] T. Takeuchi, H. Takeuchi, S. Sota, H. Sakai, H. Amano and I. Akasaki, "Optical Properties of Strained AlGaN and GaInN on GaN", *Japanese Journal of Applied Physics*, vol. 36, no. 2, 2, pp. L177-L179, 1997.

[60] J. Seo Im, H. Kollmer, J. Off, A. Sohmer, F. Scholz and A. Hangleiter, "Reduction of oscillator strength due to piezoelectric fields in GaN/$Al_xGa_{1-x}N$ quantum wells", *Physical Review B*, vol. 57, no. 16, pp. R9435-R9438, 1998.

[61] N. Grandjean, B. Damilano and J. Massies, "Group-III nitride quantum heterostructures grown by molecular beam epitaxy", *Journal of Physics: Condensed Matter*, vol. 13, no. 32, pp. 6945-6960, 2001.

[62] P. Harrison and A. Valavanis, *Quantum wells, wires and dots*, 3rd ed. West Sussex, United Kingdom: John Wiley & Sons, Inc, 2011, p. 222.

[63] T. Wang, D. Nakagawa, J. Wang, T. Sugahara and S. Sakai, "Photoluminescence investigation of InGaN/GaN single quantum well and multiple quantum wells", *Applied Physics Letters*, vol. 73, no. 24, pp. 3571-3573, 1998.

[64] Ya-Ju Lee, Ching-Hua Chiu, Chih Chun Ke, Po Chun Lin, Tien-Chang Lu, Hao-Chung Kuo and Shing-Chung Wang, "Study of the Excitation Power Dependent Internal Quantum Efficiency in InGaN/GaN LEDs Grown on Patterned Sapphire Substrate", *IEEE Journal of Selected Topics in Quantum Electronics*, vol. 15, no. 4, pp. 1137-1143, 2009.

[65] R. Oliver, S. Bennett, T. Zhu, D. Beesley, M. Kappers, D. Saxey, A. Cerezo and C. Humphreys, "Microstructural origins of

localization in InGaN quantum wells", *Journal of Physics D: Applied Physics*, vol. 43, no. 35, p. 354003, 2010.

[66] Y. Cho, G. Gainer, A. Fischer, J. Song, S. Keller, U. Mishra and S. DenBaars, "S-shaped" temperature-dependent emission shift and carrier dynamics in InGaN/GaN multiple quantum wells", *Applied Physics Letters*, vol. 73, no. 10, pp. 1370-1372, 1998.

[67] T. Badcock, S. Hammersley, D. Watson-Parris, P. Dawson, M. Godfrey, M. Kappers, C. McAleese, R. Oliver and C. Humphreys, "Carrier Density Dependent Localization and Consequences for Efficiency Droop in InGaN/GaN Quantum Well Structures", *Japanese Journal of Applied Physics*, vol. 52, no. 8, pp. 08JK10, 2013.

[68] J. Davidson, P. Dawson, T. Wang, T. Sugahara, J. Orton and S. Sakai, "Photoluminescence studies of InGaN/GaN multi-quantum wells", *Semiconductor Science and Technology*, vol. 15, no. 6, pp. 497-505, 2000.

[69] A. Morel, P. Lefebvre, T. Taliercio, T. Bretagnon, B. Gil, N. Grandjean, B. Damilano and J. Massies, "Two-dimensional "pseudo-donor–acceptor-pairs" model of recombination dynamics in InGaN/GaN quantum wells", *Physica E: Low-dimensional Systems and Nanostructures*, vol. 17, pp. 64-67, 2003.

[70] R. Martin, P. Middleton, K. O'Donnell and W. Van der Stricht, "Exciton localization and the Stokes' shift in InGaN epilayers", *Applied Physics Letters*, vol. 74, no. 2, pp. 263-265, 1999.

[71] S. Chichibu, T. Sota, K. Wada and S. Nakamura, "Exciton localization in InGaN quantum well devices", Journal of Vacuum Science & Technology B: Microelectronics and Nanometer Structures, vol. 16, no. 4, p. 2204, 1998.

[72] A. Hangleiter, J. Im, H. Kollmer, S. Heppel, J. Off and F. Scholz, "The role of piezoelectric fields in GaN-based quantum wells",

MRS Internet Journal of Nitride Semiconductor Research, vol. 3, 1998.

[73] Y. Narukawa, Y. Kawakami, M. Funato, S. Fujita, S. Fujita and S. Nakamura, "Role of self-formed InGaN quantum dots for exciton localization in the purple laser diode emitting at 420 nm", *Applied Physics Letters*, vol. 70, no. 8, pp. 981-983, 1997.

[74] D. Gerthsen, E. Hahn, B. Neubauer, A. Rosenauer, O. Schon, M. Heuken and A. Rizzi, "Composition Fluctuations in InGaN Analyzed by Transmission Electron Microscopy", *physica status solidi* (a), vol. 177, no. 1, pp. 145-155, 2000.

[75] S. Chichibu, T. Azuhata, T. Sota and S. Nakamura, "Spontaneous emission of localized excitons in InGaN single and multiquantum well structures", *Applied Physics Letters*, vol. 69, no. 27, pp. 4188-4190, 1996.

[76] I. Ho and G. Stringfellow, "Solid phase immiscibility in GaInN", Applied Physics Letters, vol. 69, no. 18, pp. 2701-2703, 1996.

[77] S. Kaprov, "Suppression of phase separation in InGaN due to elastic strain", *MRS Internet Journal of Nitride Semiconductor Research*, vol. 3, 1998.

[78] T. Smeeton, M. Kappers, J. Barnard and C. Humphreys, "Analysis of InGaN-GaN quantum well chemistry and interfaces by transmission electron microscopy and X-ray scattering", *MRS Proceedings*, vol. 798, 2003.

[79] T. Smeeton, M. Kappers, J. Barnard, M. Vickers and C. Humphreys, "Electron-beam-induced strain within InGaN quantum wells: False indium "cluster" detection in the transmission electron microscope", *Applied Physics Letters*, vol. 83, no. 26, pp. 5419-5421, 2003.

[80] J. O'Neill, I. Ross, A. Cullis, T. Wang and P. Parbrook, "Electron-beam-induced segregation in InGaN/GaN

multiple-quantum wells", *Applied Physics Letters*, vol. 83, no. 10, pp. 1965-1967, 2003.

[81] T. Smeeton, C. Humphreys, J. Barnard and M. Kappers, "The impact of electron beam damage on the detection of indium-rich localisation centres in InGaN quantum wells using transmission electron microscopy", *Journal of Materials Science*, vol. 41, no. 9, pp. 2729-2737, 2006.

[82] M. Galtrey, R. Oliver, M. Kappers, C. Humphreys, D. Stokes, P. Clifton and A. Cerezo, "Three-dimensional atom probe studies of an $In_xGa_{1-x}N$/GaN multiple quantum well structure: Assessment of possible indium clustering", *Applied Physics Letters*, vol. 90, no. 6, p. 061903, 2007.

[83] M. Galtrey, R. Oliver, M. Kappers, C. Humphreys, P. Clifton, D. Larson, D. Saxey and A. Cerezo, "Three-dimensional atom probe analysis of green- and blue-emitting $In_xGa_{1-x}N$/GaN multiple quantum well structures", *Journal of Applied Physics*, vol. 104, no. 1, p. 013524, 2008.

[84] L. Bellaiche, T. Mattila, L. Wang, S. Wei and A. Zunger, "Resonant hole localization and anomalous optical bowing in InGaN alloys", *Applied Physics Letters*, vol. 74, no. 13, pp. 1842-1844, 1999.

[85] L. Wang, "Calculations of carrier localization in $In_xGa_{1-x}N$", *Physical Review B*, vol. 63, no. 24, 2001.

[86] S. Chichibu, A. Uedono, T. Onuma, B. Haskell, A. Chakraborty, T. Koyama, P. Fini, S. Keller, S. DenBaars, J. Speck, U. Mishra, S. Nakamura, S. Yamaguchi, S. Kamiyama, H. Amano, I. Akasaki, J. Han and T. Sota, "Origin of defect-insensitive emission probability in In-containing (Al,In,Ga)N alloy semiconductors", Nature Materials, vol. 5, no. 10, pp. 810-816, 2006.

[87] D. Graham, P. Dawson, M. Godfrey, M. Kappers and C. Humphreys, "Resonant excitation photoluminescence studies of

InGaN/GaN single quantum well structures", *Applied Physics Letters*, vol. 89, no. 21, p. 211901, 2006.

[88] D. Graham, A. Soltani-Vala, P. Dawson, M. Godfrey, T. Smeeton, J. Barnard, M. Kappers, C. Humphreys and E. Thrush, "Optical and microstructural studies of InGaN/GaN single-quantum-well structures", *Journal of Applied Physics*, vol. 97, no. 10, p. 103508, 2005.

[89] S. Kalliakos, P. Lefebvre, X. Zhang, T. Taliercio, B. Gil, N. Grandjean, B. Damilano and J. Massies, "The Effects of Localization and of Electric Fields on LO-Phonon-Exciton Coupling in InGaN/GaN Quantum Wells and Quantum Boxes", *physica status solidi (a)*, vol. 190, no. 1, pp. 149-154, 2002.

[90] R. Phillips, A. Steffan, S. Newton, T. Reinecke and R. Kotlyar, "Exciton fine structure in interfacial quantum dots", *physica status solidi (b)*, vol. 238, no. 3, pp. 601-606, 2003.

[91] D. Watson-Parris, M. Godfrey, P. Dawson, R. Oliver, M. Galtrey, M. Kappers and C. Humphreys, "Carrier localization mechanisms in $In_xGa_{1-x}N$/GaN quantum wells", *Physical Review B*, vol. 83, no. 11, 2011.

[92] S. Schulz, M. Caro, C. Coughlan and E. O'Reilly, "Atomistic analysis of the impact of alloy and well-width fluctuations on the electronic and optical properties of InGaN/GaN quantum wells", *Physical Review B*, vol. 91, no. 3, 2015.

[93] A. Hangleiter, F. Hitzel, C. Netzel, D. Fuhrmann, U. Rossow, G. Ade and P. Hinze, "Suppression of Nonradiative Recombination by V-Shaped Pits in GaInN/GaN Quantum Wells Produces a Large Increase in the Light Emission Efficiency", *Physical Review Letters*, vol. 95, no. 12, 2005.

[94] N. Grandjean, E. Feltin, R. Butté, J. Carlin, S. Sonderegger, B. Deveaud and J. Ganière, "Growth mode induced carrier

localization in InGaN/GaN quantum wells", *Philosophical Magazine*, vol. 87, no. 13, pp. 2067-2075, 2007.

[95] N. van der Laak, R. Oliver, M. Kappers and C. Humphreys, "Role of gross well-width fluctuations in bright, green-emitting single InGaN/GaN quantum well structures", *Applied Physics Letters*, vol. 90, no. 12, p. 121911, 2007.

[96] J. Narayan, H. Wang, J. Ye, S. Hon, K. Fox, J. Chen, H. Choi and J. Fan, "Effect of Thickness Variation in High-Efficiency Ingan/Gan Light Emitting Diodes", *MRS Proceedings*, vol. 743, 2002.

[97] M. Smith, J. Lin, H. Jiang, A. Khan, Q. Chen, A. Salvador, A. Botchkarev, W. Kim and H. Morkoc, "Exciton-phonon interaction in InGaN/GaN and GaN/AlGaN multiple quantum wells", *Applied Physics Letters*, vol. 70, no. 21, pp. 2882-2884, 1997.

[98] S. Schulz, D. Tanner, E. O'Reilly, M. Caro, F. Tang, J. Griffiths, F. Oehler, M. Kappers, R. Oliver, C. Humphreys, D. Sutherland, M. Davies and P. Dawson, "Theoretical and experimental analysis of the photoluminescence and photoluminescence excitation spectroscopy spectra of m-plane InGaN/GaN quantum wells", *Applied Physics Letters*, vol. 109, no. 22, p. 223102, 2016.

[99] N. Bochkareva, Y. Rebane and Y. Shreter, "Efficiency droop and incomplete carrier localization in InGaN/GaN quantum well light-emitting diodes", *Applied Physics Letters*, vol. 103, no. 19, p. 191101, 2013.

[100] G. Sun, G. Xu, Y. Ding, H. Zhao, G. Liu, J. Zhang and N. Tansu, "Investigation of fast and slow decays in InGaN/GaN quantum wells", *Applied Physics Letters*, vol. 99, no. 8, p. 081104, 2011.

[101] T. Schulz, A. Nirschl, P. Drechsel, F. Nippert, T. Markurt, M. Albrecht and A. Hoffmann, "Recombination dynamics in $In_xGa_{1-x}N$ quantum wells — Contribution of excited subband

recombination to carrier leakage", *Applied Physics Letters*, vol. 105, no. 18, p. 181109, 2014.

[102] F. Nippert, A. Nirschl, T. Schulz, G. Callsen, I. Pietzonka, S. Westerkamp, T. Kure, C. Nenstiel, M. Strassburg, M. Albrecht and A. Hoffmann, "Polarization-induced confinement of continuous hole-states in highly pumped, industrial-grade, green InGaN quantum wells", *Journal of Applied Physics*, vol. 119, no. 21, p. 215707, 2016.

[103] M. Kappers, F. Massabuau and S. Sahonta, Private Communication, Feb. 2015.

[104] M. Shahmohammadi, W. Liu, G. Rossbach, L. Lahourcade, A. Dussaigne, C. Bougerol, R. Butté, N. Grandjean, B. Deveaud and G. Jacopin, "Enhancement of Auger recombination induced by carrier localization in InGaN/GaN quantum wells", *Physical Review B*, vol. 95, no. 12, 2017.

[105] U. Kaufmann, M. Kunzer, H. Obloh, M. Maier, C. Manz, A. Ramakrishnan and B. Santic, "Origin of defect-related photoluminescence bands in doped and nominally undoped GaN", *Physical Review B*, vol. 59, no. 8, pp. 5561-5567, 1999.

[106] M. Reshchikov, J. McNamara, H. Helava, A. Usikov and Y. Makarov, "Two yellow luminescence bands in undoped GaN", *Scientific Reports*, vol. 8, no. 1, 2018.

[107] M. Reshchikov and H. Morkoç, "Luminescence properties of defects in GaN", *Journal of Applied Physics*, vol. 97, no. 6, p. 061301, 2005.

[108] H. Wang, Z. Ji, S. Qu, G. Wang, Y. Jiang, B. Liu, X. Xu and H. Mino, "Influence of excitation power and temperature on photoluminescence in InGaN/GaN multiple quantum wells", *Optics Express*, vol. 20, no. 4, p. 3932, 2012.

[109] X. Cao, E. Stokes, P. Sandvik, S. LeBoeuf, J. Kretchmer and D. Walker, "Diffusion and tunneling currents in GaN/InGaN multiple

quantum well light-emitting diodes", *IEEE Electron Device Letters*, vol. 23, no. 9, pp. 535-537, 2002.

[110] A. Kaneta, M. Funato, Y. Narukawa, T. Mukai and Y. Kawakami, "Direct correlation between nonradiative recombination centers and threading dislocations in InGaN quantum wells by near-field photoluminescence spectroscopy", *physica status solidi (c)*, vol. 3, no. 6, pp. 1897-1901, 2006.

[111] G. Pozina, R. Ciechonski, Z. Bi, L. Samuelson and B. Monemar, "Dislocation related droop in InGaN/GaN light emitting diodes investigated via cathodoluminescence", *Applied Physics Letters*, vol. 107, no. 25, p. 251106, 2015.

[112] A. Laubsch, M. Sabathil, W. Bergbauer, M. Strassburg, H. Lugauer, M. Peter, S. Lutgen, N. Linder, K. Streubel, J. Hader, J. Moloney, B. Pasenow and S. Koch, "On the origin of IQE-'droop' in InGaN LEDs", *physica status solidi (c)*, vol. 6, no. 2, pp. S913-S916, 2009.

[113] Y. Shen, G. Mueller, S. Watanabe, N. Gardner, A. Munkholm and M. Krames, "Auger recombination in InGaN measured by photoluminescence", *Applied Physics Letters*, vol. 91, no. 14, p. 141101, 2007.

[114] K. Delaney, P. Rinke and C. Van de Walle, "Auger recombination rates in nitrides from first principles", *Applied Physics Letters*, vol. 94, no. 19, p. 191109, 2009.

[115] J. Iveland, L. Martinelli, J. Peretti, J. Speck and C. Weisbuch, "Direct Measurement of Auger Electrons Emitted from a Semiconductor Light-Emitting Diode under Electrical Injection: Identification of the Dominant Mechanism for Efficiency Droop", *Physical Review Letters*, vol. 110, no. 17, 2013.

[116] L. Wang, J. Jin, C. Mi, Z. Hao, Y. Luo, C. Sun, Y. Han, B. Xiong, J. Wang and H. Li, "A Review on Experimental

Measurements for Understanding Efficiency Droop in InGaN-Based Light-Emitting Diodes", *Materials*, vol. 10, no. 11, p. 1233, 2017.

[117] J. Cho, E. Schubert and J. Kim, "Efficiency droop in light-emitting diodes: Challenges and countermeasures", *Laser & Photonics Reviews*, vol. 7, no. 3, pp. 408-421, 2013.

[118] M. Schubert, J. Xu, Q. Dai, F. Mont, J. Kim and E. Schubert, "On resonant optical excitation and carrier escape in GaInN/GaN quantum wells", *Applied Physics Letters*, vol. 94, no. 8, p. 081114, 2009.

[119] Y. Shen, G. Mueller, S. Watanabe, N. Gardner, A. Munkholm and M. Krames, "Auger recombination in InGaN measured by photoluminescence", *Applied Physics Letters*, vol. 91, no. 14, p. 141101, 2007.

[120] K. Bulashevich and S. Karpov, "Is Auger recombination responsible for the efficiency rollover in III-nitride light-emitting diodes?", *physica status solidi (c)*, vol. 5, no. 6, pp. 2066-2069, 2008.

[121] Q. Dai, Q. Shan, J. Wang, S. Chhajed, J. Cho, E. Schubert, M. Crawford, D. Koleske, M. Kim and Y. Park, "Carrier recombination mechanisms and efficiency droop in GaInN/GaN light-emitting diodes", *Applied Physics Letters*, vol. 97, no. 13, p. 133507, 2010.

[122] A. Laubsch, M. Sabathil, J. Baur, M. Peter and B. Hahn, "High-Power and High-Efficiency InGaN-Based Light Emitters", *IEEE Transactions on Electron Devices*, vol. 57, no. 1, pp. 79-87, 2010.

[123] A. David and M. Grundmann, "Droop in InGaN light-emitting diodes: A differential carrier lifetime analysis", *Applied Physics Letters*, vol. 96, no. 10, p. 103504, 2010.

[124] J. Piprek, "Efficiency droop in nitride-based light-emitting diodes", *physica status solidi (a)*, vol. 207, no. 10, pp. 2217-2225, 2010.

[125] J. Hader, J. Moloney, B. Pasenow, S. Koch, M. Sabathil, N. Linder and S. Lutgen, "On the importance of radiative and Auger losses in GaN-based quantum wells", *Applied Physics Letters*, vol. 92, no. 26, p. 261103, 2008.

[126] E. Kioupakis, P. Rinke, K. Delaney and C. Van de Walle, "Indirect Auger recombination as a cause of efficiency droop in nitride light-emitting diodes", *Applied Physics Letters*, vol. 98, no. 16, p. 161107, 2011.

[127] M. Binder, A. Nirschl, R. Zeisel, T. Hager, H. Lugauer, M. Sabathil, D. Bougeard, J. Wagner and B. Galler, "Identification of nnp and npp Auger recombination as significant contributor to the efficiency droop in (GaIn)N quantum wells by visualization of hot carriers in photoluminescence", *Applied Physics Letters*, vol. 103, no. 7, p. 071108, 2013.

[128] J. Xie, X. Ni, Q. Fan, R. Shimada, Ü. Özgür and H. Morkoç, "On the efficiency droop in InGaN multiple quantum well blue light emitting diodes and its reduction with p-doped quantum well barriers", *Applied Physics Letters*, vol. 93, no. 12, p. 121107, 2008.

[129] J. Danhof, C. Vierheilig, U. Schwarz, T. Meyer, M. Peter and B. Hahn, "Temperature-dependent photoluminescence measurements on a sub-micrometer length scale on green light emitting InGaN/GaN quantum wells", *physica status solidi (b)*, vol. 248, no. 5, pp. 1270-1274, 2010.

[130] P. Eliseev, P. Perlin, J. Lee and M. Osiński, ""Blue" temperature-induced shift and band-tail emission in InGaN-based light sources", *Applied Physics Letters*, vol. 71, no. 5, pp. 569-571, 1997.

[131] O. Rubel, S. Baranovskii, K. Hantke, B. Kunert, W. Rühle, P. Thomas, K. Volz and W. Stolz, "Model of temperature quenching of photoluminescence in disordered semiconductors and comparison to experiment", *Physical Review B*, vol. 73, no. 23, 2006.

[132] C. Othick, "Optical Characterisation of Group III – Nitride Semiconductors", Ph.D Thesis, University of Manchester, 2011.

[133] A. Hospodková, T. Hubáček, J. Oswald, J. Pangrác, K. Kuldová, M. Hývl, F. Dominec, G. Ledoux and C. Dujardin, "InGaN/GaN Structures: Effect of the Quantum Well Number on the Cathodoluminescent Properties", *physica status solidi (b)*, vol. 255, no. 5, p. 1700464, 2017.

[134] M. Kappers, S. Zhang and M. Frentrup, private communication, Sept. 2018.

[135] N. Nanhui, W. Huaibing, L. Jianping, L. Naixin, X. Yanhui, H. Jun, D. Jun and S. Guangdi, "Enhanced luminescence of InGaN/GaN multiple quantum wells by strain reduction", *Solid-State Electronics*, vol. 51, no. 6, pp. 860-864, 2007.

[136] Y. Harada, T. Hikosaka, S. Kimura, M. Sugai, H. Nago, K. Tachibana, N. Sugiyama and S. Nunoue, "Effect of dislocation density on efficiency curves in InGaN/GaN multiple quantum well light-emitting diodes", *Light-Emitting Diodes: Materials, Devices, and Applications for Solid State Lighting XVI*, 2012.

[137] M. Schubert, S. Chhajed, J. Kim, E. Schubert, D. Koleske, M. Crawford, S. Lee, A. Fischer, G. Thaler and M. Banas, "Effect of dislocation density on efficiency droop in GaInN/GaN light-emitting diodes", *Applied Physics Letters*, vol. 91, no. 23, p. 231114, 2007.

[138] Q. Dai, M. Schubert, M. Kim, J. Kim, E. Schubert, D. Koleske, M. Crawford, S. Lee, A. Fischer, G. Thaler and M. Banas, "Internal quantum efficiency and nonradiative recombination coefficient of GaInN/GaN multiple quantum wells with different

dislocation densities", *Applied Physics Letters*, vol. 94, no. 11, p. 111109, 2009.

[139] A. Barker and M. Ilegems, "Infrared Lattice Vibrations and Free-Electron Dispersion in GaN", *Physical Review B*, vol. 7, no. 2, pp. 743-750, 1973.

[140] P. Hurst, P. Dawson, S. Levetas, M. Godfrey, I. Watson and G. Duggan, "Temperature Dependent Optical Properties of InGaN/GaN Quantum Well Structures", *physica status solidi* (b), vol. 228, no. 1, pp. 137-140, 2001.

[141] S. Hammersley, M. Kappers, F. Massabuau, S. Sahonta, P. Dawson, R. Oliver and C. Humphreys, "Effects of quantum well growth temperature on the recombination efficiency of InGaN/GaN multiple quantum wells that emit in the green and blue spectral regions", *Applied Physics Letters*, vol. 107, no. 13, p. 132106, 2015.

[142] K. Kazlauskas, G. Tamulaitis, P. Pobedinskas, A. Žukauskas, M. Springis, C. Huang, Y. Cheng and C. Yang, "Exciton hopping in $In_xGa_{1-x}N$ multiple quantum wells", *Physical Review B*, vol. 71, no. 8, 2005.

[143] B. Crutchley, I. Marko and S. Sweeney, "The influence of temperature on the recombination processes in blue and green InGaN LEDs", *physica status solidi (c)*, vol. 10, no. 11, pp. 1533-1536, 2013.

[144] O. Rubel, M. Galluppi, S. Baranovskii, K. Volz, L. Geelhaar, H. Riechert, P. Thomas and W. Stolz, "Quantitative description of disorder parameters in (GaIn)(NAs) quantum wells from the temperature-dependent photoluminescence spectroscopy", *Journal of Applied Physics*, vol. 98, no. 6, p. 063518, 2005.

[145] A. Uedono, S. Ishibashi, N. Oshima, R. Suzuki and M. Sumiya, "Point Defect Characterization of Group-III Nitrides by Using Monoenergetic Positron Beams", *ECS Transactions*, vol. 61, no. 5, pp. 19-30, 2014.

[146] T. Langer, H. Pietscher, H. Bremers, U. Rossow, D. Menzel and A. Hangleiter, "Nonradiative recombination due to point defects in GaInN/GaN quantum wells induced by Ar implantation", *Gallium Nitride Materials and Devices VIII*, 2013.

[147] S. Chichibu, A. Uedono, T. Onuma, T. Sota, B. Haskell, S. DenBaars, J. Speck and S. Nakamura, "Limiting factors of room-temperature nonradiative photoluminescence lifetime in polar and nonpolar GaN studied by time-resolved photoluminescence and slow positron annihilation techniques", *Applied Physics Letters*, vol. 86, no. 2, p. 021914, 2005.

[148] B. Ding, F. Massabuau, S. Sahonta, M. Kappers, C. Humphreys and R. Oliver, "Effects of dislocations on the optical properties of blue and green InGaN/GaN Quantum Wells grown at different temperatures", Poster presented at: *UK Nitrides Consortium Winter Conference*, 2017 Jan 5-6, Oxford, UK

[149] M. Davies, P. Dawson, F. Massabuau, F. Oehler, R. Oliver, M. Kappers, T. Badcock and C. Humphreys, "The effects of varying threading dislocation density on the optical properties of InGaN/GaN quantum wells", *physica status solidi (c)*, vol. 11, no. 3-4, pp. 750-753, 2014.